THE UNIVERSITY OF QUEENSLAND

AUSTRALIA

Realistic models for detection of neuronal currents with magnetic resonance imaging

Jiaxin Du

Bachelor of Science (BS), and Master of Science (MS)

A thesis submitted for the degree of Doctor of Philosophy at

The University of Queensland in 2015

Queensland Brain Institute

Abstract

A great challenge facing brain research is to “see” neurons in action at high spatial and temporal resolution in the living human brain. While existing non-invasive techniques, such as electroencephalography (EEG), magnetoencephalography (MEG), and functional magnetic resonance imaging (fMRI), have either poor spatial or temporal resolution, neuronal current MRI (nc-MRI) may hold the potential to revolutionize cognitive neuroscience by imaging neuronal activity at high temporal and spatial resolutions. However, the implementation of nc-MRI using existing instrumentation is yet to be convincingly demonstrated.

In this project, I investigated the feasibility of nc-MRI via computer simulations. To allow realistic neuronal current simulations, the laminar cortex model (LCM) was first developed. The LCM incorporates the laminar architecture of the cerebral cortex into a continuum cortex model (previously developed by Wright et al.) to simulate the collective activity of cortical neurons. As validations, the LCM has been used to simulate the local field potentials (LFP) of the primary visual cortex. The LCM produced spontaneous LFPs exhibited frequency-inverse (1/f) power spectrum behaviour. The LCM also captured the fundamental as well as the high order harmonics under intermittent light stimulation.

To model neuronal currents, I decomposed the neuronal activity simulated by the LCM into action potentials and postsynaptic potentials. The geometries of dendrites and axons were generated dynamically to account for neuronal morphology diversity. Magnetic fields produced by action potentials and postsynaptic potentials were calculated for the cases of spontaneous and stimulated cortical activity, from which the nc-MRI signal was determined. The MRI signal magnitude change was found to be below currently detectable levels (< 0.1 part-per-million), but signal phase change was potentially detectable (in the order of 0.1 milli-radian). Furthermore, nc-MRI signals were sensitive to temporal and spatial variations in neuronal activity and independent of the intensity of neuronal activation. Synchronous neuronal activity produces large phase changes, up to 1 milli-radian, and the signal phase oscillated with neuronal activity.

Based on the computer simulation results, I proposed to image oscillatory neuronal currents using a multi-echo spin echo (MESE) and a synchronised multi-echo gradient recalled echo (MEGRE) sequences. A MESE sequence can accumulate phase changes for multiple neuronal activity oscillation periods through applying radio-frequency (RF)

excitation pulses at the times when neuronal magnetic fields change sign. MEGRE sequence could be used to extract neuronal current signal from noisy MRI signals, because neuronal current signal but not blood-oxygen-level dependent (BOLD) effect or noise, varies with neuronal oscillation. Because a MEGRE sequence is capable of acquiring MRI signals at a series of closely-spaced time points, the inherent oscillation of neuronal current signals may potentially be deduced from the temporal profile of the MRI signals. I performed MRI experiments to image neuronal currents in the visual cortex induced by intermittent light stimulation using the proposed sequences. Significant neuronal current signal was absent due to the limited signal-to-noise ratio achieved by the system. I concluded that new MRI hardware and software (sequences and image analysis methods) is required for capturing neuronal currents signal in the brain.

Declaration by author

This thesis is composed of my original work, and contains no material previously published or written by another person except where due reference has been made in the text. I have clearly stated the contribution by others to jointly-authored works that I have included in my thesis.

I have clearly stated the contribution of others to my thesis as a whole, including statistical assistance, survey design, data analysis, significant technical procedures, professional editorial advice, and any other original research work used or reported in my thesis. The content of my thesis is the result of work I have carried out since the commencement of my research higher degree candidature and does not include a substantial part of work that has been submitted to qualify for the award of any other degree or diploma in any university or other tertiary institution. I have clearly stated which parts of my thesis, if any, have been submitted to qualify for another award.

I acknowledge that an electronic copy of my thesis must be lodged with the University Library and, subject to the policy and procedures of The University of Queensland, the thesis be made available for research and study in accordance with the Copyright Act 1968 unless a period of embargo has been approved by the Dean of the Graduate School.

I acknowledge that copyright of all material contained in my thesis resides with the copyright holder(s) of that material. Where appropriate I have obtained copyright permission from the copyright holder to reproduce material in this thesis.

Publications during candidature

Du J., Vegh V., and Reutens D.C. (2012) The laminar cortex model: a new continuum cortex model incorporating laminar architecture. PLoS Comput Biol 8: e1002733.

Du J., Vegh V., and Reutens D.C. (2014) MRI signal phase oscillates with neuronal activity in cerebral cortex: implications for neuronal current imaging. Neuroimage 94: 1-11.

Publications included in this thesis

Du J., Vegh V., Reutens D.C. (2012) The laminar cortex model: a new continuum cortex model incorporating laminar architecture. PLoS Comput Biol 8: e1002733 – incorporated as Chapter 4.

Contributor	Statement of contribution
Jiaxin Du (Candidate)	Conceived and designed the experiments (60%); Performed the experiments (100%); Analysed the data (60%); Wrote the paper (60%).
Viktor Vegh	Conceived and designed the experiments (20%); Analysed the data (20%); Wrote the paper (20%).
David Reutens	Conceived and designed the experiments (20%); Analysed the data (20%); Wrote the paper (20%).

Du J., Vegh V., Reutens D.C. (2014) MRI signal phase oscillates with neuronal activity in cerebral cortex: implications for neuronal current imaging. Neuroimage 94: 1-11 – incorporated as Chapter 5.

Contributor	Statement of contribution
Jiaxin Du (Candidate)	Conceived and designed the experiments (60%); Performed the experiments (100%); Analysed the data (60%); Wrote the paper (60%).
Viktor Vegh	Conceived and designed the experiments (20%); Analysed the data (20%); Wrote the paper (20%).
David Reutens	Conceived and designed the experiments (20%); Analysed the data (20%); Wrote the paper (20%).

Contributions by others to the thesis

No contributions by others.

Statement of parts of the thesis submitted to qualify for the award of another degree

None.

Acknowledgements

I would like to express my sincere gratitude to many people for their support, guidance, and encouragement during my study in the University of Queensland. First of all, I am deeply grateful to my supervisors Prof David Reutens and Dr Viktor Vegh, who introduced me to the field of magnetic resonance imaging. Without their continuous support and guidance, this thesis would not have been possible.

I would like to thank my PhD milestone committee members, A/Prof Ross Cunnington, Prof Graham Galloway and Dr Peter Stratton, for their help and valuable suggestions during the study.

I would like to give a special thanks to my wife, Meng Yang. Sometimes the PhD study seemed to be a journey that would never come to an end. Her patience, understanding and love make the journal less stressful and more enjoyable. Thank you for sharing with me the wonderful moments and hard times in the last four and half years. I also want to thank my father, my mother who passed away many years ago, and my sisters for their encouragement and infinite support.

Thanks to you all.

Keywords

magnetic resonance imaging, neuronal current imaging, neuronal magnetic field

Australian and New Zealand Standard Research Classifications (ANZSRC)

ANZSRC code: 029903 Medical Physics, 60%

ANZSRC code: 100499 Medical Biotechnology not elsewhere classified, 20%

ANZSRC code: 170205 Neurocognitive Patterns and Neural Networks, 20%

Fields of Research (FoR) Classification

FoR code: 1109, Neuroscience, 60%

FoR code: 1702, Cognitive Science, 40%

Table of Contents

List of Figures

List of Abbreviations

AP: action potential;

BOLD: blood-oxygen-level-dependent;

CCM: continuum cortex model;

cm: centimetre(s);

CSD: current source density;

EEG: electroencephalography;

EFP: extracellular field potential;

EPSP: excitatory postsynaptic potential;

FID: free induction decay;

fMRI: function magnetic resonance imaging, functional MRI;

GRE (GE): gradient (recalled) echo;

GE-EPI: gradient echo echo-planar imaging;

IPSP: inhibitory postsynaptic potential;

LCM: laminar cortex model;

LFP: local field potential;

MEG: magnetoencephalography;

MEGRE: multi-echo gradient (recalled) echo;

MESE: multi-echo spin echo sequence;

mm: millimetre(s);

MRI: magnetic resonance imaging;

msec: millisecond(s);

MUA: multi-unit activity;

nc-MRI: neuronal current magnetic resonance imaging;

NMF: neuronal magnetic field;

PAT: phase accumulating time;

ppm: part-per-million;

PSP: postsynaptic potential;

pT: pico-Tesla (10^{-12} Tesla);

rad: radian (1 radian = 57.296 degree);

RF: radio frequency;

SE: spin echo;

SE-EPI: spin echo echo-planar imaging;

sec: second(s);

SSVEP: steady-state visually evoked potential;

TE: time to echo;

TR: repetition time;

ULF: ultra-low field;

μm: micrometre(s) (10^{-6} metre).

Chapter 1

Introduction

A great challenge facing brain research is to “see” neurons in action at high spatial and temporal resolution in the living human brain. Non-invasive neuroimaging techniques, notably electroencephalography (EEG), magnetoencephalography (MEG), and functional magnetic resonance imaging (fMRI), have provided invaluable knowledge about brain function in health and disease. However, EEG and MEG are low spatial resolution techniques that infer neuronal activity from limited scalp measurements (Hamalainen et al., 1993; Niedermeyer and Lopes da Silva, 2005), and fMRI is a low temporal resolution method (Logothetis et al., 2001; Logothetis, 2008) that deduces brain activation indirectly from blood-oxygen-level-dependent (BOLD) changes that are driven by complex, non-linear hemodynamic processes (Logothetis et al., 2001; Handwerker et al., 2012).

Neuronal activity produces small transient currents (Hille, 2001; Nunez and Srinivasan, 2006). These currents may be detectable via magnetic resonance imaging (MRI) because they produce relatively small neuronal magnetic fields (NMFs) that perturb the imaging magnetic field. As a result, changes in the precession frequencies of surrounding protons may modulate the MRI signal and provide information about neuronal activity (Singh, 1994; Kamei et al., 1999; Bandettini et al., 2005; Hagberg et al., 2006). Theoretically, this effect, termed neuronal current MRI (nc-MRI), has the potential to map neuronal activity at higher spatial and temporal resolutions than existing neuroimaging methods (Bandettini et al., 2005). Successful implementation of nc-MRI would benefit the study of brain function and may also have important clinical applications, such as the non-invasive mapping of epileptic foci (Liston et al., 2004). Previous MRI experiments that attempted to capture neuronal current signals have been performed on several experimental models, including turtle (Luo et al., 2009) and snail ganglia (Park et al., 2004), and on humans (Xiong et al., 2003; Konn et al., 2004; Luo et al., 2011a) using various MRI sequences and a range of acquisition parameters. The findings have been inconsistent, even when similar MRI sequences and parameters were used (for example, see Xiong et al., 2003; Chu et al.,

2004; Parkes et al., 2007). Therefore, the feasibility of nc-MRI has been debated (Bandettini et al., 2005; Hagberg et al., 2006).

Computer simulations are an important paradigm for predicting the nc-MRI techniques that are most likely to succeed. However, a major challenge to simulate the nc-MRI signal is the accurate modeling of the spatial distribution and temporal variation of neuronal currents. Previous models have simulated neuronal currents using an ensemble of identical neurons, such as an anatomically realistic pyramidal neuron from the rat cortex (Blagoev et al., 2007), the monkey hippocampus (Cassara et al., 2008), or the human cortex (Luo et al., 2011b). This approach reduces the computational complexity inherent in simulating the dynamics of a large number of individual neurons. However, the MRI signal predicted by such models may be inaccurate for two reasons. First, the morphological differences between neurons, which may exert a significant impact on the size of the calculated NMFs (Cassara et al., 2008), are ignored. Second, the models in which all of the neurons exhibit identical firing patterns are likely to produce neuronal currents with unrealistic temporal pattern.

In the present thesis, I investigate the feasibility of nc-MRI using computer simulations. A laminar cortex model (LCM) was developed based on laminar architecture and the synaptic connections of the cortex and incorporated into the continuum cortex model (Wright, 2009). The LCM was used to simulate the neuronal activity at different oscillation states in the primary visual cortex of the cat. The NMFs of the neuronal activity were calculated and used to predict neuronal current-induced MRI signals. The project was intended to answer the following questions,

1. Is neuronal current detectable using currently available MRI techniques?
2. How is the nc-MRI signal related to neuronal activity?
3. What MRI protocol should be used to detect neuronal current signals?

This thesis is organized as follows. Chapter 2 and Chapter 3 are literature reviews. In Chapter 2, the basics of neuronal activity, neuronal field potentials and magnetic fields are reviewed. Chapter 3 provides a summary of the existing nc-MRI simulations and experiments. In Chapter 4, I introduce the LCM and use it to simulate the neuronal activity of the primary cortex. Chapter 5 is dedicated to neuronal current simulation and nc-MRI signal prediction. A preliminary MRI experimental validation of the simulation results is

provided in Chapter 6. Chapter 7 is a general discussion and specific conclusions are drawn at the end.

Chapter 2

Literature review I: electric currents of neuronal activity

Successful implementation of nc-MRI experiments requires an imaging protocol that specifically targets neuronal currents. To achieve this goal, an understanding of neuronal currents is essential, as the nc-MRI signals are functions of the temporal and spatial magnetic fields produced by neuronal currents (Blagoev et al., 2007; Heller et al., 2009). While existing nc-MRI simulations have attempted to model the electric currents of a cluster of dendrites (Xue et al., 2006; Park and Lee, 2007; Huang et al., 2010; Jay et al., 2012) or an assemblage group of identical neurons (Blagoev et al., 2007; Cassara et al., 2008; Luo et al., 2011b), this project aims to model the currents produced by realistic neuronal activity. Such a model has only become possible because vast knowledge about neuronal activity has been made available from studies using various techniques, such as the membrane potential and neuronal field potential recording techniques, EEG, and MEG. In this chapter, I provide a review of basic neuronal function based on previous literature (mainly Johnston and Wu, 1995; Kandel et al., 2000) as well as the neuronal basis of neuronal field potentials and magnetic fields.

2.1 Neuronal membrane potentials

Neurons are the computing units of the nervous system. A neuron consists of three major compartments (see Figure 2-1): the cell body (also known as the soma), where most metabolic processes occur; an axon, which delivers action potentials (AP) to other neurons; and a tree of dendrites that receive synaptic inputs from other neurons. Like all other cells in the human body, neurons are enclosed by a phospholipid bilayer, termed the *plasma membrane* or simply the *membrane*, which separates the intracellular fluid from the surrounding extracellular environment.

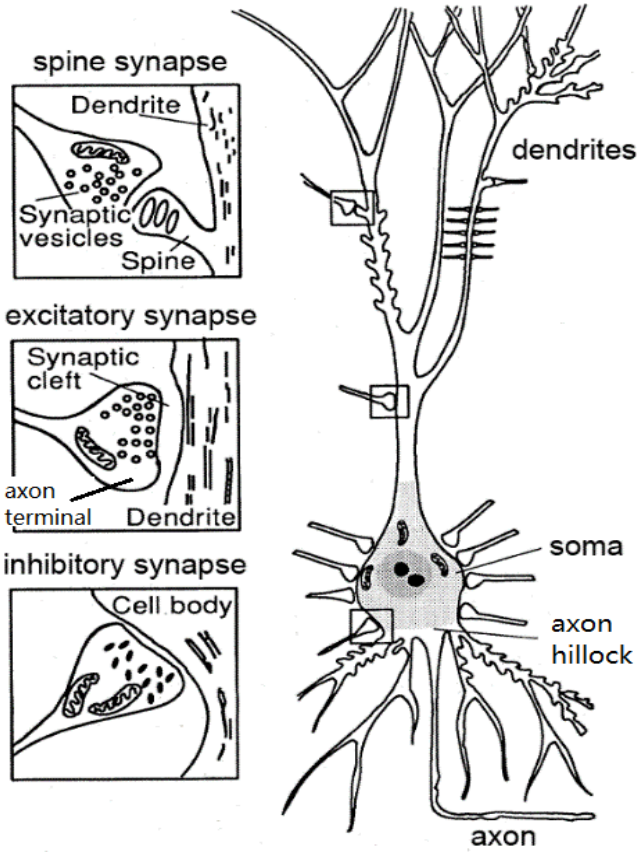

Figure 2-1 Neuron structure.

Illustrated are a cortical neuron and three magnified synapses (figure reproduced from Hamalainen et al., 1993).

The plasma membrane constitutes an effective barrier that prevents most hydrophilic molecules from permeating the cell, and it is highly impermeable to ions. However, some ions may pass through the membrane with the help of carriers formed by transmembrane proteins. Some transmembrane proteins only allow ions moving down their ion concentration gradients, i.e., from the high concentration side to the low concentration side of the membrane. These proteins, called *ion channels*, provide a pathway by which ions can freely pass through the membrane. Ion channels possess two distinctive features. First, an ion channel typically only allows one species of ions to pass, a feature which is usually called *selective permeability*. For example, the three most common ion channels, sodium channels, potassium channels, and chlorine channels, are only permeable to Na^+, K^+ and Cl^-, respectively. Second, some ion channels can change their conformation from a closed (inactive) state to an open (active) state, or *vice versa*, in the presence of a certain stimulus, which is a mechanism commonly referred to as *gating*. For example, a voltage-gated ion channel can be opened/closed by a local membrane potential change, and

ligand-gated ion channels are typically activated upon binding to specific ligands, such as neurotransmitters. The functions of ion channels are of special interest to neuroscientists, but their extent is so vast that over 300 ion channels have been identified in the brain and their functional roles are not completely understood. For detailed descriptions of various ion channels, the reader may wish to review textbooks such as (Hille, 2001) and (Johnston and Wu, 1995).

	Concentration (millimole)	
Ion	Intracellular	Extracellular
Potassium (K^+)	140	5
Sodium (Na^+)	5-15	145
Chlorine (Cl^-)	4-30	110
Calcium (Ca^{2+})	0.0001	1-2

Table 2-1: Extracellular and intracellular ion concentrations.

Listed are the typical intracellular and extracellular ion concentrations in mammals (Data acquired from Purves, 2004).

Another class of transmembrane protein carriers is *ion transporters*, which can transport ions against the concentration gradient, i.e., from the low concentration side to the high concentration side of the membrane, often at the expense of energy. The most important ion transporter is the Na^+-K^+ pump, which transports Na^+ out of, and K^+ into, the neuron at a ratio of 3:2. While the Na^+-K^+ pump utilizes energy via the hydrolysis of adenosine triphosphate (ATP), some ion transporters, known as *ion exchangers*, utilize the energy associated with the electrochemical gradient of one ionic species to transport another ionic species. For example, Na^+-Ca^{2+} exchangers can transport the Na^+ down its electrochemical gradient and utilize the associated energy to transfer Ca^{2+} from the low concentration side to the high concentration side of the membrane.

Ion channels and ion transporters are crucial for the function of neurons. One of their functions is to maintain *the membrane potential*, which is the electric potential difference across the membrane. The membrane potential is closely related to the ion concentration difference across the membrane. Because of unidirectional ion transport via ion transporters, the intracellular and extracellular concentrations of some ions, notably Na^+, K^+, Cl^-, and Ca^{2+}, are significantly different (see Table 2-1). The ion concentration gradients impose a chemical potential force on the corresponding ions, as ions tend to move from a high-concentration region to a low-concentration region. In a resting neuron, the chemical potential force is counteracted by an electrical force that originates from the

electric potential difference across the membrane. Because ion transporters move unequal electric charges (which are carried by ions) into and out of neurons, a net positive charge accumulates outside of the membrane, and a net negative charge accumulates inside of the membrane. These unbalanced charges form an electrical field, which imposes an electrical force on all of the ions. In a resting neuron, the chemical and electrical forces are completely cancelled out, and the electrical potential difference across the membrane is

$$V_{\mathrm{m}} = V_{\mathrm{i}} - V_{\mathrm{o}} = \frac{RT}{F}\ln\frac{P_{\mathrm{K}}[\mathrm{K}^+]_{\mathrm{o}} + P_{\mathrm{Na}}[\mathrm{Na}^+]_{\mathrm{o}} + P_{\mathrm{Cl}}[\mathrm{Cl}^-]_{\mathrm{i}}}{P_{\mathrm{K}}[\mathrm{K}^+]_{\mathrm{i}} + P_{\mathrm{Na}}[\mathrm{Na}^+]_{\mathrm{i}} + P_{\mathrm{Cl}}[\mathrm{Cl}^-]_{\mathrm{o}}}, \tag{2.1}$$

where V_{i} and V_{o} represent the electric potential (also called voltage) of the inside and outside of the membrane, respectively; R represents the ideal gas constant of 8.31 J/(K·mol); F represents the Faraday's constant of 9.65×10^4 C/mol; T represents the absolute temperature in Kelvin; P_{A} represents the permeability of ion A through the membrane, which is determined by the density of the corresponding open ion channels; and $[\mathrm{A}]_{\mathrm{i}}$ and $[\mathrm{A}]_{\mathrm{o}}$ represent the concentration of ion A in the intracellular and extracellular fluid, respectively. This equation is known as *Goldman's equation*, and the electrical potential difference across membrane is known as the membrane potential. Although equation (2.1) only includes three types of ions, K^+, Na^+ and Cl^-, other ions, such as Ca^{2+}, can be included in the equation accordingly (Johnston and Wu, 1995).

It should be noted that different ions play different roles in maintaining the membrane potential. For example, if the membrane was only permeable to Na^+, the membrane potential would be approximately +55 mV (this membrane potential is called the *equilibrium potential* of Na^+ (E_{Na})), but the equilibrium potential for K^+ (E_{K}) would be -90 mV and that of Cl^- (E_{Cl}) would be -65 mV. In a resting neuron, the resting membrane potential is between the equilibrium potentials of K^+ and Na^+ ($E_{\mathrm{K}} \le V_{\mathrm{m}} \le E_{\mathrm{Na}}$), and it is typically closer to E_{K}, in the range of -90 to -50 mV, because the membrane is much more permeable to K^+ than to Na^+ and Cl^-, i.e., $P_{\mathrm{K}} \gg P_{\mathrm{Na}}$ and $P_{\mathrm{K}} \gg P_{\mathrm{Cl}}$. Furthermore, ions continuously move across the membrane at the resting membrane potential. The current across the membrane can be calculated using the following equation:

$$I_{\mathrm{A}} = g_{\mathrm{A}}(V_{\mathrm{m}} - \mathrm{E}_{\mathrm{A}}), \tag{2.2}$$

where I_{A} represents the current of ion A across the membrane and g_{A} corresponds to the membrane conductance for ion A, which is determined by the permeability of the membrane to ion A. At the resting membrane potential, the conductance of K^+ is larger than the conductance of Na^+, but the V_{m} is closer to E_{k} than E_{Na}. Therefore, both the sodium and potassium currents are small at the resting membrane potential, and they are counteracted by the currents generated by ion transporters resulting in no net transmembrane current.

Neurons are capable of rapidly changing their membrane potential. They can open or close thousands of ion channels in a millisecond, and thereby alter the membrane permeability followed by the intracellular concentration of certain ions, which changes the membrane potential. When the membrane permeability to a particular ion increases, then the membrane potential moves toward the equilibrium potential of that ion. For example, at the beginning of an action potential, a large number of voltage-gated sodium channels open, thereby significantly increasing the membrane permeability to Na^+ and shifting the membrane potential to a less negative voltage or even a positive voltage ($E_{\mathrm{Na}} > 0$); this process is commonly referred to as *depolarization*. However, during synaptic transmission, inhibitory neurotransmitters may open ligand-gated chlorine channels, increasing the membrane permeability to Cl^- and shifting the membrane potential to a more negative voltage; this process is referred to as *repolarization*.

Neuronal membrane potentials are the essence of neuronal activity. Neurons encode neuronal information into membrane potential changes (action potentials and sub-threshold potentials) and conduct them to neighboring neurons or even to other regions of the brain where this information is further processed or used to innervate or coordinate body movements. Determining how membrane potential changes initiate and evolve in the brain is the central task of functional neuroimaging, which can be used to help neuroscientists understand how the brain functions.

2.2 Action potentials and postsynaptic potentials

The two predominant membrane potential changes in the brain are *postsynaptic potentials* (PSPs) and *action potentials* (APs). PSPs are caused by synaptic inputs, while APs are initialized in a neuron and transmit outputs to other neurons.

2.2.1 Action potentials

APs, also known as *spikes*, are generated in the *axon hillock* (also known as *axon initial segment, AIS*), which is a unique region of the soma that connects to the axon (see Figure 2-1). The axon hillock is capable of initializing APs because it contains a very high density of voltage-gated sodium and potassium channels, and the voltage-gated ion channels are sensitive to relatively small membrane potential changes. The voltage-gated sodium and potassium channels both open when the membrane potential reaches a threshold value, which is approximately 15-30 mV above the resting membrane potential. However, the two types of channels behave slightly differently. The sodium channels open within a short time after the membrane potential increase. They only remain open for approximately one msec before closing, and they do not respond to membrane potential changes until the membrane potential returns to a value close to the resting membrane potential. The potassium channels open approximately one msec after the sodium channels open, and their open duration is longer than the sodium channels.

When the afferent membrane potential reaches the threshold, the sodium channel opens first, which allows for a strong influx of Na^+, causing the membrane to depolarize. This depolarization occurs rapidly because the increased membrane potential leads to the opening of more sodium channels, allowing more Na^+ to flow in, which is known as *positive feedback*. Because the membrane becomes more permeable to Na^+ than to K^+, the membrane potential quickly moves toward the equilibrium potential of Na^+ ($E_{\mathrm{Na}} \approx +55$ mV). The membrane potential usually reaches a positive value, which is called *overshoot*. After approximately one msec, the sodium channels close and remain closed for the rest of the AP, and the potassium channels begin to open, allowing K^+ to flow out of the neuron. At this point, the membrane is more permeable to K^+ than to Na^+; therefore, the membrane potential moves towards the equilibrium potential of K^+ ($E_{\mathrm{K}} \approx -90$ mV) and then gradually returns to the resting membrane potential. The potassium channels may remain open for an additional short period, which leads to further depolarization of the membrane potential, and the membrane potential may reach a value more negative than the resting potential, an effect called *undershoot*. After both the sodium and potassium channels are closed, the Na^+-K^+ pump moves the Na^+ out of and K^+ into the neuron to restore the membrane potential to prepare for the next AP.

It has been shown recently that sodium channel density at the axon hillock of cortical pyramidal neurons is about 50 times higher than that in soma and proximal dendrites (Kole et al., 2008). Such a high sodium channel density plays a critical role in AP initialization, because they can produce large inward ionic currents in a short time. The strong currents can compensate the current loss due to AP backpropagation to the soma and dendrites, and ensure a strong potential change can be triggered in the axon.

APs can be conducted along the axon. During the initiation phase of an AP, the strong influx of sodium can depolarize the next axon segment and cause it to produce its own AP. In this way, the AP can propagate from the axon hillock to the distal end of the axon, typically to an axon (presynaptic) terminal, where synaptic transmission may occur. In the brain, most axons are myelinated. Myelinated axons are wrapped with a thick layer of insulation called *myelin*. Myelin is not continuous; it breaks periodically at gaps called *nodes of Ranvier*. Myelination can increase the conduction rate of an AP by a factor of more than 10 (Kandel et al., 2000).

2.2.2 Postsynaptic potentials

PSPs are initialized at synapses (see Figure 2-1). A synapse is a specialized region where one neuron make contact and communicate with another neuron. A synapse is generally formed between the axon terminal of the presynaptic neuron and the dendrite or soma of the postsynaptic neuron. In the brain, a typical neuron receives thousands of synaptic connections from other neurons.

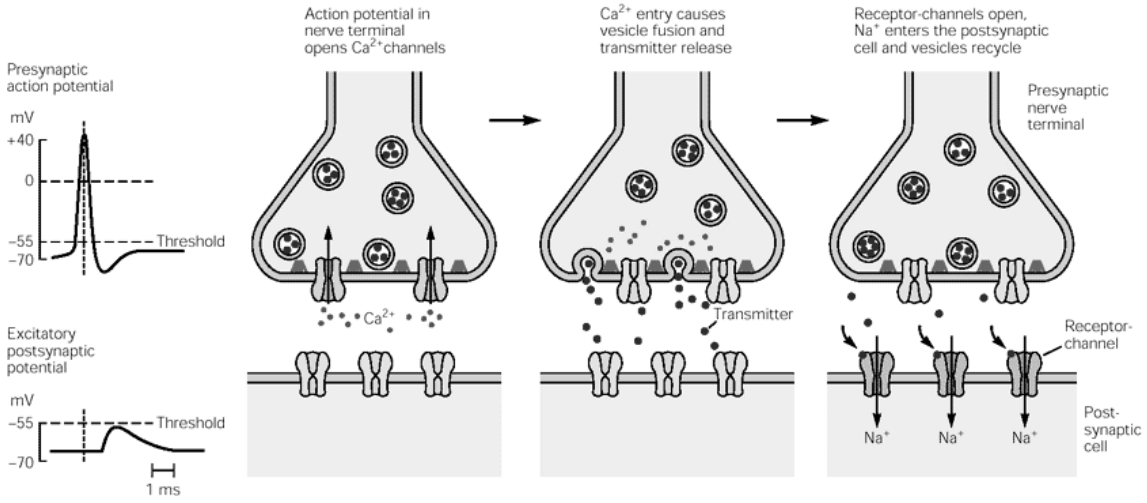

Figure 2-2 Synaptic transmission.

The synaptic transmission process is illustrated (figure reproduced from Kandel et al., 2000).

Most synapses in the brain are chemical in nature, which means that they use a large amount of molecules, known as *neurotransmitters*, as messengers to transmit information from one neuron to another neuron. As shown in Figure 2-2, at a chemical synapse, two neurons are not directly connected. Instead, they are separated by a small gap, which is referred to as the *synaptic cleft*. Chemical synapses are unidirectional, which means that neuronal signals can only travel from the axon terminal of one neuron to the soma and/or dendrite of the other neuron. The neuron that transmits this signal is called the *presynaptic neuron*, and the neuron that receives the signal is called the *postsynaptic* neuron.

Prior to synaptic transmission, neurotransmitters are stored in *synaptic vesicles* inside the presynaptic terminal (see Figure 2-2). Synaptic transmission is triggered when an AP arrives at the presynaptic terminal. Upon the arrival of the AP, a large number of voltage-gated Ca^{2+} channels open, which allows for a strong influx of Ca^{2+}. The increased intracellular Ca^{2+} concentration causes the synaptic vesicles to fuse with the presynaptic membrane (a process termed *exocytosis*), thereby releasing their neurotransmitter molecules into the synaptic cleft. Neurotransmitters act as chemical messengers between the presynaptic and postsynaptic neurons. When neurotransmitters diffuse to the membrane of the postsynaptic neuron, they bind to a unique group of ion channels known as *neurotransmitter receptors*, causing them open or close. This change in the permeability of the membrane leads to an additional inward or outward flow of ions, which changes the membrane potential of the postsynaptic neuron. The membrane potential change is termed the *postsynaptic membrane potential* (PSP).

Although all chemical synapses share a similar synaptic transmission process, synapses are diverse with respect to their neurotransmitter and postsynaptic mechanism. Broadly, synapses can be classified into two groups, excitatory and inhibitory synapses, and their postsynaptic potentials are called excitatory PSPs (EPSPs) and inhibitory PSPs (IPSPs), respectively. An EPSP depolarizes the membrane potential ($\Delta V > 0$), while an IPSP repolarizes the membrane potential ($\Delta V < 0$). The most common excitatory neurotransmitter is glutamate. Glutamate can bind to multiple postsynaptic receptors, including the NMDA (N-methyl-D-aspartate) receptor and the AMPA (α-amino-3-hydroxy-5-methyl-4-isoxazolepropionic acid) receptor. These receptors are all permeable to Na^+ and K^+ and sometimes Ca^{2+} (some AMPA receptors and all NMDA receptors are permeable to Ca^{2+}). Although the membrane permeability to both Na^+ and K^+ are

increased, the inward Na^+ flow and the possible inward Ca^{2+} flow dominate the early phase of the EPSP because the resting membrane potential is closer to the equilibrium potential of K^+ compared to the equilibrium potentials of Na^+ and Ca^{2+}. The inward Na^+ and/or Ca^{2+} flow depolarizes the membrane potential.

The most common inhibitory neurotransmitter is GABA (γ-aminobutyric acid). GABA can also bind to multiple receptors, including the $GABA_A$ and $GABA_B$ receptor. $GABA_A$ receptors are ion channels that are selectively permeable to Cl^- upon activation, which allows for the influx of Cl^-. This can cause the membrane potential to become more negative, repolarizing the neuron. When activated, the $GABA_B$ receptor can open K+ channels via G-proteins, which leads to repolarization of the neuron.

In the brain, a neuron typically receive thousands of PSPs in a short time window, and the PSPs can travel from the synapses to the soma of the neuron. During the conduction from synapses to the soma, PSPs typically decay exponentially in amplitude (Johnston and Wu, 1995). In the soma, PSPs from the dendrites and the soma are aggregated, which may initialize an AP. In this manner, neurons perform atomic computational tasks by converting its various synaptic inputs from other neurons into spikes and delivering them to other neurons. The spiking of a neuron depends on not only the synaptic inputs but also the morphology of the neuron, the ion channel type and density on the neuron, and other factors. The manner in which various synaptic inputs affect the spiking of neurons remains a hot research topic.

2.3 Neuronal field potentials

Neuronal activity redistributes the electric charges around neurons, thereby changing the surrounding electric field potentials. The field potentials of the brain, called *neuronal field potentials*, have been measured using various electrode techniques to infer information about various aspects of neuronal activity. Neuronal field potential recording techniques were once a dominant method of neuronal activity measurement, and they remain an important tool for neurophysiological studies today. In this section, I provide a brief review of the characteristics of various neuronal field potential recordings; more detailed descriptions of neuronal field potentials can be found elsewhere (Johnston and Wu, 1995; Logothetis, 2002; Nunez and Srinivasan, 2006).

Neuronal field potentials have been measured from different anatomical locations. For example, electrodes can be placed on the scalp to measure electroencephalogram (EEG) signals non-invasively, on the surface of the cortex to measure electrocorticogram (ECoG) signals, or in the extracellular space inside the brain to measure extracellular field potentials (EFPs). Because these techniques measure voltage fluctuations originating from the same transmembrane currents of neuronal activity, their signals share many similarities with respect to frequency. Therefore, EEG sometimes is used to broadly refer to all neuronal field potential recordings. However, neuronal field potentials recorded from distinct locations also exhibit two major differences. First, their spatial specificities are different. The EEG signals measured at an electrode are likely to reflect the neuronal activity of a region of approximately 10 cm^2 (Nunez and Srinivasan, 2006), which is at least 100 times larger than the region measured using the ECoG and EFPs. Moreover, the ECoG is only measured on the surface of the cortex, while EFPs can be measured in the cortex. Furthermore, EEG signals but not ECoG signals or EFPs may suffer from distortion and attenuation caused by the soft tissues and the skull that are between the electrode tip and the current source (Nunez and Srinivasan, 2006). Thus, EEG signals are, though non-invasive, less accurate than ECoG and EFP signals. In conclusion, as a brain electric activity measurement, EFP recordings are the most informative method. In fact, EFPs are used as the gold standard technique for measuring neuronal activity in the brain.

2.3.1 Extracellular field potentials

EFPs has been quantified using the volume conductor theory, in which the extracellular space is considered as a three-dimensional volume conductor with homogeneous conductivity and the transmembrane currents are treated as the current sources. Based on these simplifications, EFPs are determined based on the trans-membrane currents according to (Nunez and Srinivasan, 2006):

$$\phi(\mathbf{r},t) = \sum_n \frac{1}{4\pi\sigma} \frac{i_n(\mathbf{r}',t)}{|\,\mathbf{r}-\mathbf{r}'\,|}\,, \tag{2.3}$$

where $\phi(r,t)$ represents the EFPs; σ represents the extracellular conductivity; $i_n(\mathbf{r}',t)$ represents the transmembrane current; $\mathbf{r}$ and $\mathbf{r}'$ correspond to the locations of the transmembrane currents and the electrode tip, respectively; and the summation is calculated over all of the transmembrane currents. In equation (2.3), $i_n > 0$ indicates that

the current flows into the volume conductor (i.e., the extracellular space), and the site where current enters the volume conductor is defined as the current *source*; alternatively, $i_n < 0$ indicates that current flows out of the volume conductor, and the site where the current exits is defined as the current *sink*.

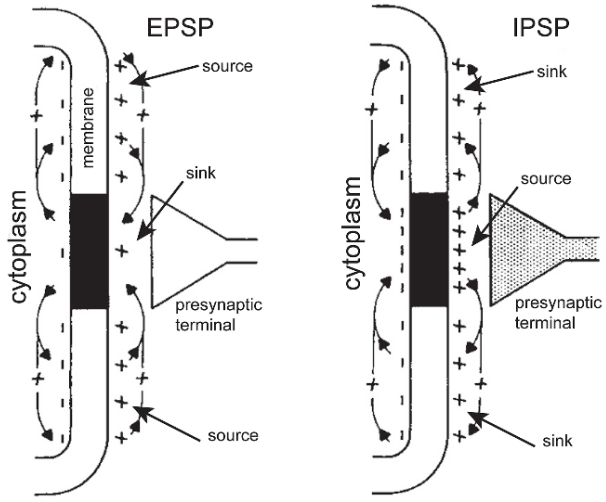

Figure 2-3 The return currents of excitatory and inhibitory PSPs.

Illustrated are the return currents and the corresponding current source and sink of an EPSP and an IPSP (figure reproduced from Niedermeyer and Lopes da Silva, 2005).

Theoretically, all transmembrane currents can contribute to the EFPs, including those produced by synaptic transmission, PSPs, APs, and other neuronal activity components (Buzsaki et al., 2012). Postsynaptic activities, i.e., PSPs on dendrites and somas, are thought to be the primary contributor to the EFP (Buzsaki et al., 2012), but the effects of excitatory and inhibitory synaptic activity are different. For excitatory synaptic activity, countless AMPA and NMDA receptors are activated by neurotransmitters, which generate an inward Na^+ and Ca^{2+} flow, thereby producing a local current sink. According to Kirchhoff's circuit laws, in an electric circuit, an inbound current to a node must be balanced by an outbound current to achieve so-called electroneutrality in the node. In a neuronal system, the postsynaptic current is typically balanced by another transmembrane current with the opposite sign, which is generally defined as the *return current*. Because the generation of the return current does not involve a change in membrane conductivity, it is commonly referred to as a *passive current*, while the postsynaptic current is commonly referred to as an *active current*. In a neuron, if only one excitatory synapse is active, the return current is typically distributed along the neuron and close to the synapse. However,

in the brain, an active neuron may receive thousands of excitatory synaptic inputs in a short time window. If the active synapses are on basal or apical dendrites, the synchronised synaptic activities generate a large active current sink on the basal or apical dendrites, and the return current is typically located in the soma. In such a situation, the entire neuron can be considered as an electric dipole that contains a positive charge in the soma and negative charges in the dendrites. If a neuron receives simultaneous inputs from multiple directions with respect to the soma, this condition may also generate higher-order n-poles (see Nunez and Srinivasan, 2006 for more information).

Neurons also receive inhibitory synaptic inputs. Inhibitory postsynaptic activity produces an inward flow of Cl^- that acts as an *active current source* (an inward negative current is equivalent to an outward positive current because of electroneutrality), but inhibitory postsynaptic activity only produces very small EFPs because neurons typically form far fewer inhibitory synapses than excitatory synapses, and the inhibitory postsynaptic current is typically small unless the neuron is highly depolarized, as the equilibrium potential of Cl^- is close to the resting membrane potential. For that reason, the contribution of inhibitory postsynaptic activity to EFPs is less explored in the literature.

Although an AP produces transmembrane currents that are at least 10 times larger than a PSP, APs generate smaller EFPs than PSPs (Buzsaki et al., 2012). The shape of EFPs are determined by not only the magnitudes and signs of individual transmembrane currents and their spatial density but also the temporal synchrony of the current sources (Buzsaki et al., 2012). The contribution of a single transmembrane current to the EFP is quite small, and large EFPs can only emerge when a large number of current sources overlap in time (i.e., synchronous currents). Compared with APs, which persist for approximately 1 msec, PSPs are slow events that last for approximately 10 msec, and PSPs typically outnumber APs by at least two orders of magnitude. Therefore, PSPs can easily overlap in time and space, producing a strong EFP wave, while APs do not often overlap and therefore generate separate small EFP waves. For the same reason, APs and PSPs generate EFPs that differ with respect to their temporal pattern: PSPs primarily contribute to the low frequency component of the EFPs (<300 Hz), also known as local field potentials (LFPs), and APs are more likely to produce high frequency EFPs (>500 Hz), also known as multi-unit activity. Other types of neuronal activity may also contribute to EFPs, including sub-threshold membrane oscillations (Kamondi et al., 1998) and spike

after-potentials (Buzsaki, 2002). Their contributions are relatively small and less explored in the literature.

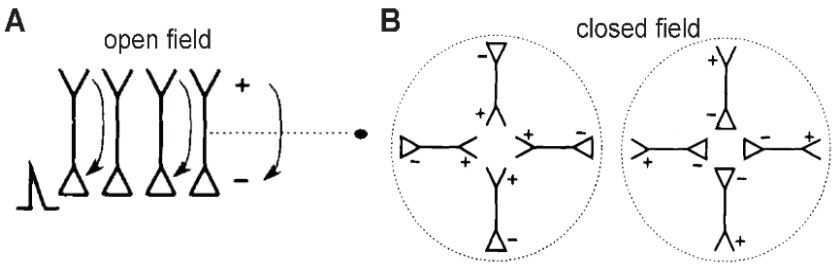

Figure 2-4 Open and close field for EFPs.

Illustrated are (A) neurons arranged in an open field and (B) neurons arranged in two different closed fields (figure reproduced from Johnston and Wu, 1995).

In a neuron population level, EFPs represent field potential changes that are produced by neurons in the vicinity of the electrode tips. The contribution of individual neurons are not only weighted by the inverse of the distance of the neuron to the tip, but also depends on the size and shape of the neurons (see equation (2.3)). Large pyramidal neurons typically produce larger EFPs than small neurons. If the electrode tip is located near the soma of a pyramidal neuron, the recorded field potential will be dominated by EFPs generated from the spiking activity. This effect is used to detect the spiking activity of individual neurons (Henze et al., 2000). Therefore, to measure the EFPs produced by a group of neurons, the electrode tip should avoid the somas of large neurons. Furthermore, the geometrical arrangement of the neurons also affects the shape of the EFPs. Two neuron arrangements that produce distinctive field potentials have been proposed: *open field* and *closed field* (Johnston and Wu, 1995). Open field refers to an arrangement in which the neurons are organized in a polarized manner, where the dendrites are on one side and the somas are on the other side. Open field is common in the neocortex, the cerebellum and the hippocampus, where neurons are organized in a laminar architecture. When synchronously activated, neurons arranged in an open field configuration produce a macroscopic electric dipole, as shown in Figure 2-4. The field potentials around the open field are also laminated; i.e., the field potential near the current source layer is the opposite of that of the current sink layer. The closed field is typically formed by neurons organized in a spherical manner, where the somas are located in the center and the dendrites are on the periphery, or vice versa. The synchronous activity of neurons in a closed field creates a spherical dipole, in which the field potentials of the center exhibit an opposite sign from

those of the periphery. Brain regions containing open fields are likely to produce strong EFPs when stimulated by a synchronised input, while activated closed fields generate EFPs less efficiently.

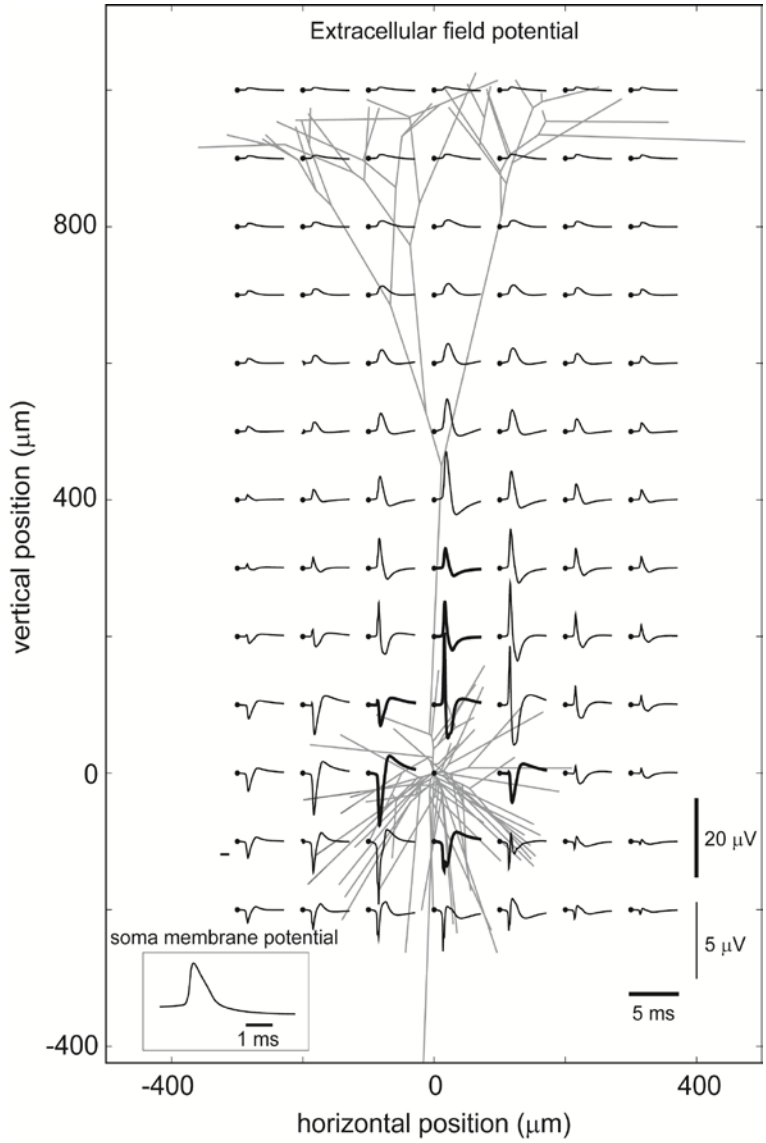

Figure 2-5 Extracellular field potential of a single neuron.

Presented is the simulated EFP signature of a layer-5 pyramidal neuron generating an AP. The neuron is stimulated by apical excitation inputs and basal inhibition inputs. The traces display the EFP of a 5 msec window during firing. The thick lines correspond to a 20 μV scale and the thin lines to a 5 μV scale. The subfigure in the bottom left window shows the membrane potential in the soma of the neuron (figure reproduced from Pettersen et al., 2010).

Spatial EFPs are typically analyzed using the *current source density* (CSD) method to obtain information regarding current sources and sinks (Nunez and Srinivasan, 2006). For CSD analysis, EFPs are simultaneously recorded at equally spaced points along a line. If

the coordinates of the points on the line are denoted as x_1, x_2, …, x_n and the voltages recorded at these points as V_1, V_2, …, V_n, then the CSD function is the second spatial derivative of the voltage, calculated as

$$I_i = \left.\frac{\partial^2 V}{\partial x}\right|_{x=x_i} \approx \frac{V_{i+1} + V_{i-1} - 2V_i}{\left(\Delta x\right)^2}, \tag{2.4}$$

where Δx represents the distance between the points. The CSD function remains a useful tool for locating the site of synaptic activity.

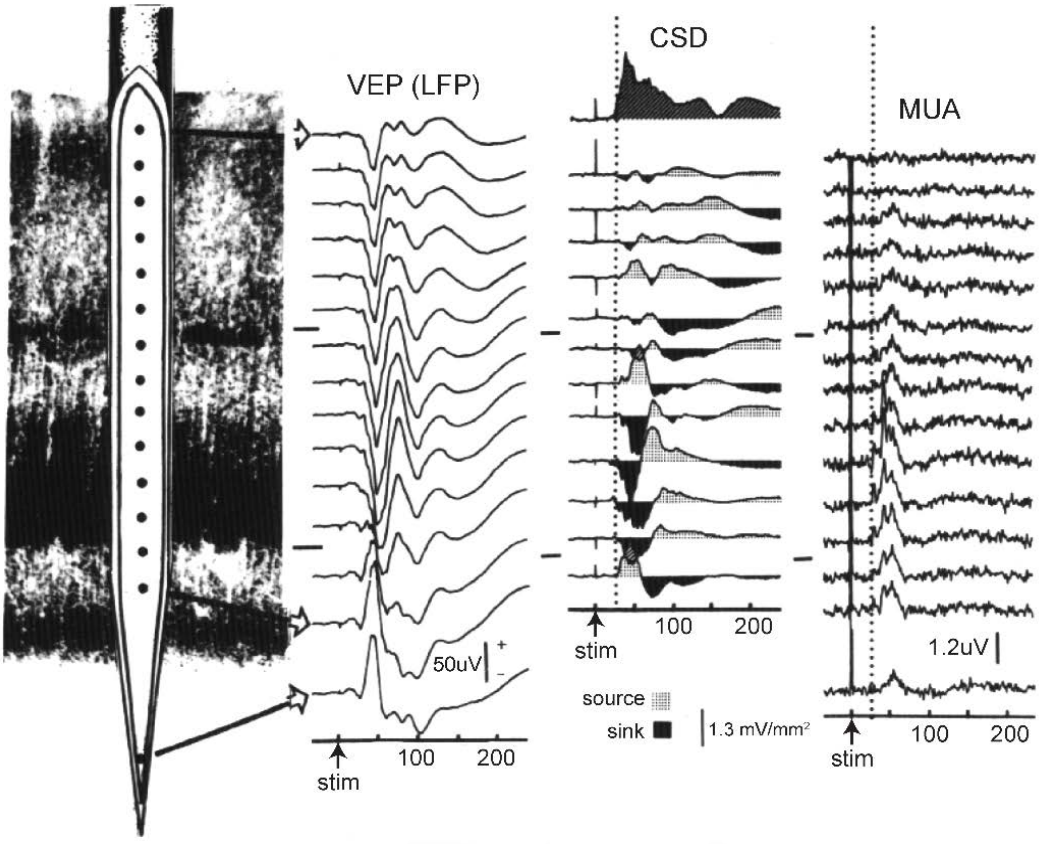

Figure 2-6 CSD in the primary visual cortex.

Presented is an example of current source density (CSD) analysis in the primary cortex. The EFPs are recorded using a multi-contact electrode from which the LFP, CSD, and MUA recordings are calculated. (figure reproduced from Schroeder et al., 1998)

2.3.2 Local Field Potentials (LFP)

LFPs, the low frequency (<300 Hz) component of EFPs, are thought to originate from the dendritic and somatic processing of synaptic inputs within approximately 250 µm from the electrode tip (Mitzdorf, 1985a, 1987; Katzner et al., 2009; Kajikawa and Schroeder,

2011). LFPs are widely used to examine not only the activity of individual neurons but also the synchronised activities of neuronal networks (Buzsaki and Draguhn, 2004; Berens et al., 2010; Einevoll et al., 2013). Recently, LFP recording has become even more popular because studies have shown that LFPs can be used to predict the BOLD functional MRI signals (Logothetis et al., 2001; Logothetis, 2003).

LFPs are typically analyzed in the frequency domain. In the absence of stimulation, the LFPs in the mammalian cortex are dominated by slow fluctuations, and the power spectrum density of the LFPs is known to be proportional to the inverse of the frequency ($1 / f$ where f is frequency) or sometimes to the inverse power of the frequency ($1 / f^n$, where $n \geq 1$), which is commonly referred to as 1/f frequency scaling or power-law behavior (Freeman et al., 2000). The origin of 1/f frequency scaling is unclear, although several explanations have been proposed. For instance, 1/f frequency scaling may be due to self-organized criticality (Bak et al., 1987), which refers to the natural characteristics of a dynamic system containing extended spatial degrees of freedom, in which complexity can emerge independent of the details of the system. In self-organized criticality it is argued that the 1/f noise is in fact not noise but reflects the intrinsic dynamics of self-organized critical systems (Bak et al., 1987, 1988). Another effect that may account for 1/f noise is the intrinsic dendritic low-pass filtering effect of large pyramidal neurons (Linden et al., 2010; Linden et al., 2011). It was found that the morphology of neuronal dendritic trees may impose a low-pass filtering effect on neuronal oscillations, largely damping the high-frequency EFPs (Linden et al., 2010). Alternatively, it has been also suggested that 1/f frequency scaling may be caused by ionic diffusion due to the electric field, which can lead to a frequency-dependent attenuation of the EFPs (Bedard and Destexhe, 2009). Further theoretical and experimental studies must be performed to elucidate the rationality of these theories.

LFPs in the living brain display oscillations at several frequency bands from approximately 0.05 Hz to 500 Hz (Buzsaki, 2002; Buzsaki and Draguhn, 2004). These different frequency oscillations of LFPs are likely related to the recurrent activity of individual neurons and neuronal networks of varying spatial scale. For example, in the mammalian brain, low frequency oscillations are thought to be produced by the thalamo-cortical network and modulated by global neuromodulatory inputs (Buzsaki and Draguhn, 2004; Steriade, 2006), while high frequency oscillations (30-90 Hz, gamma frequency)

likely arise from small local microcircuits. These correlations may be due to the limited speed of neuronal communication because of delays in axonal conduction and synapse delay. Therefore, fast oscillations can only occur in local neuronal networks that only involve neurons within a small region, while low frequency oscillations can be generated by large neuronal networks that contain neurons from different regions.

2.4 Magnetoencephalography (MEG)

Neuronal currents also generate magnetic fields, termed *neuronal magnetic fields*, which are measured on the scalp and are used to infer the neuronal activity in the brain (see Figure 2-7). This technique is known as MEG. The neuronal magnetic field and the MEG technique are reviewed in this section.

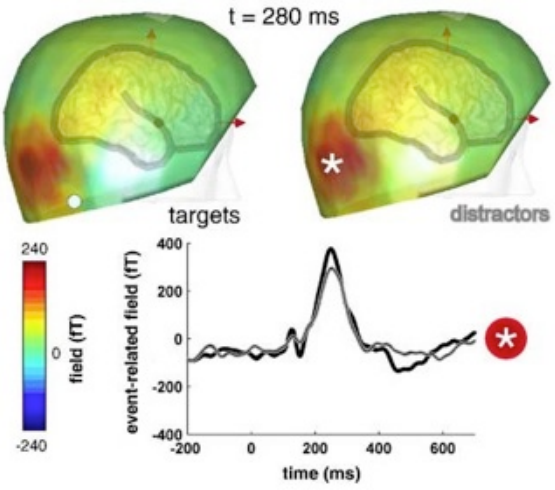

Figure 2-7 MEG signals of an epileptic patient.

Shown is the topography of the magnetic fields measured by MEG on an epileptic patient as well as the time series of the evoked fields measured at the peak sensor. “Target” and “distractor” are two mechanisms of stimulation. For further details, please refer to (Dalal et al., 2009), (figure reproduced from Dalal et al., 2009).

Because neuronal magnetic fields are small (less than 1 part-per-billion of the Earth’s magnetic fields), MEG experiments must be conducted in a magnetically shielded room to avoid the interference of the Earth’s magnetic fields and background electromagnetic waves. Moreover, highly sensitive magnetometers, such as super-conducting quantum interference devices (SQUIDs), must be used. These highly sensitive magnetometers are typically attached to a flux transformer, a device used to increase the magnetic flux across the magnetometer, thus enhancing the signal level (see Figure 2-8). A simple coil may be

used as a flux transformer. In this case, the magnetometer measures the magnetic field components orthogonal to the plane of the coil. This type of magnetometer is sensitive to not only the magnetic fields from the brain but also the magnetic fields generated by muscles and the heart, which may disturb the neuronal magnetic field signal. Another type of flux transformer utilizes an additional compensation coil, which converts the magnetometer into a gradiometer. Because the homogeneous components of magnetic fields are cancelled by the compensation coils, magnetic gradiometers are only sensitive to magnetic field gradients (see Hamalainen et al., 1993 for details). Because magnetic fields generated by distant sources are nearly homogeneous, gradiometers are more resistant to noise from the heart and muscles.

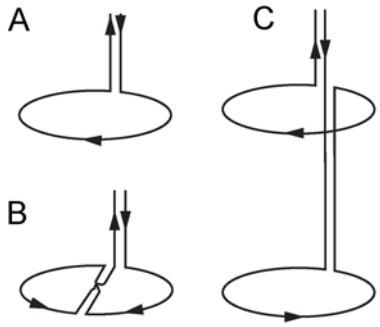

Figure 2-8 Flux transformer for MEG sensors.

Shown are three types of flux transformer geometries: (A) magnetometer, (B) planar gradiometer, and (C) axial gradiometer. (figure reproduced from Hansen et al., 2010)

MEG and (scalp) EEG are the only non-invasive neuroimaging techniques that can measure neuronal activity with a millisecond resolution. They are two complementary techniques that measure different signals generated by the same sources, neuronal currents. The MEG and EEG signals measured from the same individual are generally consistent. However, MEG and EEG are also different in many aspects. First, because of the vector nature of the magnetic field, MEG is only sensitive to tangential currents (currents that are parallel to the skull), while EEG is sensitive to currents of all orientations. Moreover, the EEG signal, but not the MEG signal, can be distorted by the brain tissue, the cerebrospinal fluid, the skull, and the scalp between the sources and the recording sites. Furthermore, current sources in the deep brain produce very weak MEG signals but considerable EEG signals.

Because MEG measures magnetic fields far away from the sources, equivalent current dipoles are typically used to represent the current sources. A current dipole is a point current source that can be expressed as $\mathbf{J}(\mathbf{r}') = \mathbf{q}\delta(\mathbf{r}_q - \mathbf{r}')$, where $\delta(\mathbf{r})$ represents the delta function, $\mathbf{q}$ corresponds to the moment of the dipole, and $\mathbf{r}_q$ corresponds to the location of the dipole. Its magnetic fields can be expressed as

$$\mathbf{B}(\mathbf{r}) = \frac{\mu_0}{4\pi} \frac{\mathbf{r} \times \mathbf{r}_q}{\mathbf{r}\left|\mathbf{r} - \mathbf{r}_q\right|^3} \cdot \mathbf{q}\,, \tag{2.5}$$

where μ_0 represents the magnetic permeability. Theoretically, a current distribution with an arbitrary spatial extension can always be broken down into smaller regions, each of which can be represented by equivalent current dipoles. The equivalent current dipole concept largely simplifies the relationship between neuronal magnetic fields and current sources; therefore, it is widely used for MEG source modeling.

Similar to EEG, MEG faces the challenge of estimating the source of the observed magnetic fields, the so-called inverse problem. Theoretically, the current sources of the magnetic field distribution can be solved using Maxwell equations. However, MEG measures the neuronal magnetic fields at limited (~100) isolated locations, and the brain is a complex structure consisting of compartments exhibiting heterogeneous electrical properties. Therefore, the source of the MEG signal cannot be uniquely resolved unless assumptions are made. Generally, there are two types of methods used to estimate the source of the MEG signal: parametric and imaging methods. The parametric method assumes that the current source can be represented by several equivalent current dipoles, and the locations, orientations, and amplitudes of the dipoles are estimated using a numeric method. The imaging method first assigns a current dipole to a small cortical region that may generate a MEG signal; i.e., the locations and the orientations of the current dipoles are pre-set, and the MEG signals are used to determine the amplitude of each current dipole. These two methods are both limited by the fact that the number of current dipoles in the brain may exceed the number of spatial measurements. Therefore, the sources estimated using each algorithm may be significantly different, and the more plausible solution is commonly chosen based on prior knowledge.

The MEG signal has been used to estimate the effect of neuronal currents on the MRI signal. However, this estimation may inaccurately predict the neuronal current signal. The

magnetic fields detected via MEG are produced by neurons in a centimeter-scale brain region, but nc-MRI is expected to detect signals produced by a much smaller region (approximately 1 mm). Furthermore, NMFs in the near-field may be different from those in the far-field. Near-field NMFs are heavily influenced by the shape of the neuronal currents, which are determined by the local neuronal architecture.

2.5 Cortical architecture

In this project, I have considered the effects of the neuronal arrangements on the nc-MRI signals. Neuronal current signals are most frequently measured in the visual cortex. The cortical architecture, especially cortical lamination and cortical columns, may have a significant impact on the neuronal current-induced MRI signal. In this section, I introduce the two features of cortical organization.

Most of the cortex consists of the neocortex, containing six cellular layers or laminae (Kandel et al., 2000). The cortical layers, numbered in Roman numerals from superficial to deep, differ with respect to neuron type, neuron density, and synaptic connection pattern. Layer I (also known as the molecular layer) contains only few scattered neurons, but it contains a large number of synapses formed between the apical dendrites of pyramidal cells from other layers and the horizontally oriented axons from various origins; layers II and III are commonly combined because they do not display a cytoarchitectonic border, and both layers contain primarily medium-sized pyramidal neurons that form intracortical connections. Layer IV contains a high neuron density, primarily consisting of spiny stellate and star pyramidal neurons, which can receive inputs from the thalamus and distribute them to the other layers. Layer V contains the largest pyramidal cells, and it is the major target of the thalamic projections. Layer VI contains neurons with various morphologies, which send initial projections to thalamus as well as other cortical regions.

The cortex is horizontally organized into columns (Mountcastle, 1997). The *cortical column*, also known as the *cortical module*, is a fundamental unit of cortical organization consisting of a vertical group of cells spanning all of the cortical layers. Columns typically display a diameter of 300-600 μm, and their size is consistent across species. The neurons in a column often contain the same receptive field, preferably responding to the same stimulation features in a similar manner. In the primary visual cortex, for example,

cells containing the same orientation preferences are grouped into ocular dominance columns. Therefore, it has been argued that cortical columns may be the fundamental processing unit of the cortex (Mountcastle, 1997).

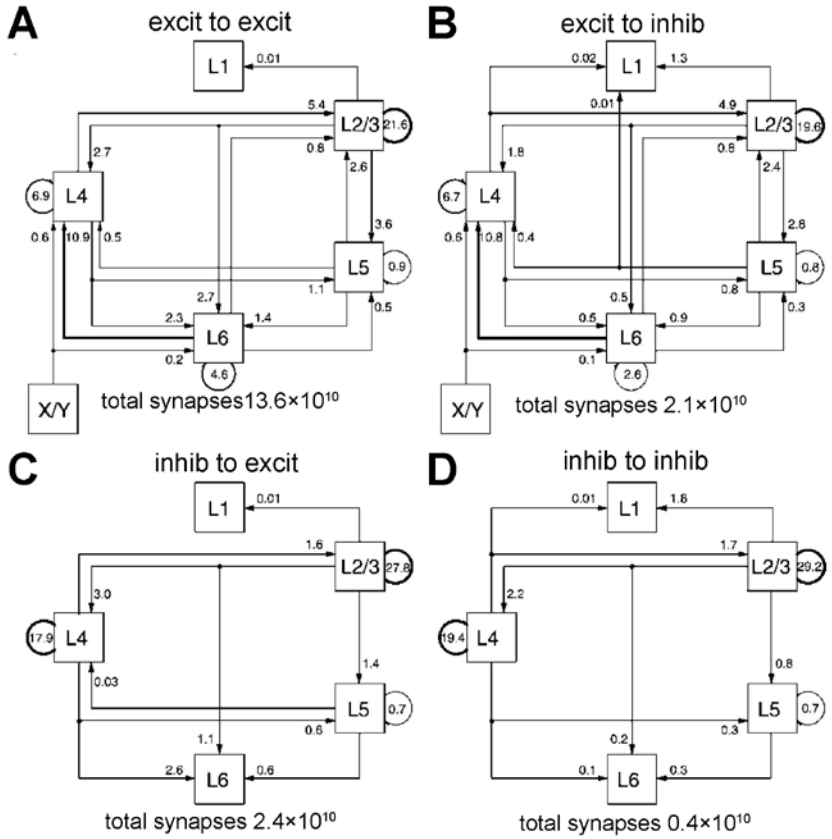

Figure 2-9 A neuronal network in the primary visual cortex.

Presented are the schematics of several synapses formed between excitatory and inhibitory neurons of the cortical layers and the X-type and Y-type afferents from the dorsal LGN to the primary visual cortex. The numbers above the arrows indicate the proportion of the synapses that are formed between excitatory neurons (A), from excitatory neurons onto inhibitory neurons (B), from inhibitory neurons onto excitatory neurons (C), and between inhibitory neurons (D). The total number of synapses are indicated below each figure. The data are estimates using cats (figure reproduced from Binzegger et al., 2004).

Cortical lamination and cortical column organization may affect the neuronal current signal. Neurons in cortical layers may exhibit dendrite trees of different shapes, and they may also fire in different patterns. This firing patterns is likely to affect the temporal and spatial patterns of the neuronal currents. Moreover, the synaptic connections between neurons within cortical layers determine the propagation direction of spikes, which can shape the directions of the neuronal currents. These factors should be considered when estimating the neuronal current signal. Furthermore, neurons in a cortical column display

similar responses to specific stimuli, which is likely to affect the spatial pattern of the neuronal activity under certain stimuli, thereby affecting the neuronal current signal. In this project these two cortical features have been taken into consideration when modeling the nc-MRI signal.

Chapter 3

Literature review II: imaging neuronal current using magnetic resonance imaging

In this chapter, I provide a brief review of the current knowledge about the MRI-based neuronal activity imaging. The first section is a brief introduction to the basic principles of the MRI technique. Blood-oxygen-level-dependent (BOLD) functional MRI is the predominant method used for neuronal activity imaging, but BOLD fMRI technique has limited spatial and temporal resolutions. In the second section, the neuronal basis of BOLD fMRI and its temporal and spatial resolutions are reviewed. Following that, in the last two sections of the chapter, the existing nc-MRI experimental evidence and theoretical models are introduced.

3.1 Magnetic Resonance Imaging (MRI)

MRI, or *nuclear magnetic resonance imaging*, is a medical imaging technique that utilizes the nuclear magnetic resonance (NMR) phenomenon to produce internal images of the human body. MRI technique is widely used to study the brain. It has been proven to be a powerful tool for imaging brain structures, connections, tissue diffusion states, and other brain conditions. MRI technique is also routinely used to detect regional activation in the brain during cognitive tasks and the resting state (Ogawa et al., 1990b; Ogawa et al., 1990a; Biswal et al., 1995). MRI measures the signals produced by excited proton spins, the behavior of which may be influenced by the property, micro-structure and magnetic micro-environments of tissues. Using the appropriate sequence and parameter settings, MRI technique is capable of acquiring images weighted by one or more contrasts, such as proton intensity, magnetization relaxation times, water diffusion and so on (see Haacke et al., 1999; Bernstein et al., 2004). These images can provide a multi-dimensional representation of the state of the brain. In this section, I provide a brief overview of MRI signal generation based on the literature (Haacke et al., 1999; Liang and Lauterbur, 2000;

Bernstein et al., 2004). However, for details regarding MRI techniques, the readers may wish to review the literature.

3.1.1 Spin magnetization

MRI measures the signals generated by nuclear spins inside the human body. *Spin*, denoted by $\vec{S}$, is the intrinsic angular momentum carried by elementary particles. Most MRI experiments utilize hydrogen nuclei (^{1}H), i.e., protons, because of their ubiquity and abundance in biological tissues. The spin of a charged particle, such as a proton, also produces a small magnetic moment. The spin magnetic moment, denoted by $\vec{\mu}$, is proportional to the spin angular momentum, i.e.,

$$\vec{\mu} = \gamma \vec{S}, \tag{3.1}$$

where γ corresponds to the *gyromagnetic ratio*, which for protons is $\gamma_{\mathrm{p}} = 42.58$ MHz/T, and the overhead arrows indicate the vector nature of the quantities. In the absence of an externally applied magnetic field, spin magnetic moments are randomly oriented, and thus do not produce macroscopic spin magnetic moment. Therefore, the human body normally does not display spin magnetic moment.

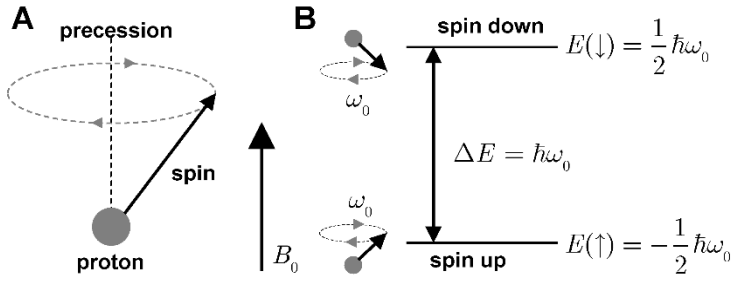

Figure 3-1 Illustration of proton spin in a magnetic field.

Illustrated are (A) the movement of proton in a magnetic field, and (B) the energy associated with the spin up and spin down states. Note the rotation direction of the spin in (A).

MRI data acquisition is conducted in a strong and homogeneous magnetic field (usually on the order of Tesla), generally referred to as the *imaging field* or B_0, and it is historically defined along the z-axis. When a subject enters the imaging field, the state of the proton spins inside the subject's body changes. First, the magnetic field constantly changes the direction but not the magnitude of the spin magnetic moment. The motion equation is

$$\frac{d\vec{\mu}}{dt} = \gamma\vec{\mu} \times \vec{B}_0 \,. \tag{3.2}$$

The motion described by Equation (3.2) is defined as *precession* (see Figure 3-1). During precession, the z-component of the spin magnetic moment does not change at all, and the transverse component constantly rotates. The rotation frequency is

$$\omega_0 = \gamma B_0 \,, \tag{3.3}$$

which is known as the *Larmor frequency*. Precession only changes the precession phase of the spin magnetic moments, which is typically defined as the angle from the transverse component to the x-axis. The motion of a spin is also constrained by another rule explained by quantum mechanics that the spin component in the direction of the magnetic field can only be $S_i = s_i\hbar$, where $\hbar$ is the Dirac constant, $s_i = -s, -s+1, \cdots, s-1, s$, and s corresponds to the spin quantum number of the particle. For example, a proton displays a spin quantum number of 1/2, so in the direction of magnetic field, it contains only two possible components:

$$S_z(\uparrow) = \hbar \,/\, 2 \quad \text{and} \quad S_z(\downarrow) = -\hbar \,/\, 2 \tag{3.4}$$

which are referred to as the *spin up* (↑) and *spin down* (↓) states, respectively. The probability of finding a proton in spin up or spin down states is determined the energy associated with the state. In a thermal equilibrium state, the probabilities for spin up or spin down states are

$$\begin{aligned} P(\uparrow) &= \frac{e^{\hbar\omega_0/(2kT)}}{e^{\hbar\omega_0/(2kT)} + e^{-\hbar\omega_0/(2kT)}} \\ P(\downarrow) &= \frac{e^{-\hbar\omega_0/(2kT)}}{e^{\hbar\omega_0/(2kT)} + e^{-\hbar\omega_0/(2kT)}} \end{aligned} \,, \tag{3.5}$$

respectively, where $k = 1.38 \times 10^{-23}$ J/K is Boltzmann's constant, and T represents the absolute temperature of the sample. At room temperature, there are more protons in spin up state than in the spin down state, and the excess up spins generate a net magnetic moment. The net magnetic moment density, also referred to as the *spin magnetization* or simply *magnetization*, is written as

$$\vec{M}_0(z) = \sum_{\text{all spins}} \mu_z = \rho_0 \left[P(\uparrow)\mu_z(\uparrow) + P(\downarrow)\mu_z(\downarrow) \right] \simeq \frac{\rho_0 \gamma^2 \hbar^2}{4kT} \vec{B}_0 \,, \tag{3.6}$$

where ρ_0 represents the proton density of the tissue. Therefore, the overall effect of the imaging field is a static longitudinal spin magnetization. Although individual spin magnetic moments contain transverse components, they exhibit random phases and thus do not produce a macroscopic transverse magnetization component in total.

3.1.2 Free induction decay and relaxation time

MRI technique measures signals produced by a transverse spin magnetization rather than the static longitudinal spin magnetization. In most MRI experiments, a short transverse oscillatory magnetic field, known as a radiofrequency (RF) pulse, is used to drive the spin magnetization away from the imaging field to producing a rotating transverse magnetization component (see Figure 3-2). This process is commonly referred to as *magnetization excitation*, and the magnetic field of the RF pulse is commonly referred to as B_1. An effective RF pulse must be perpendicular to the imaging field B_0, and its frequency must correspond to the Larmor frequency:

$$\omega = \omega_0 = \gamma B_0 \,. \tag{3.7}$$

Equation (3.7) is known as the *resonance condition*. The spin magnetization can only be driven by magnetic fields at Larmor frequency, and this effect is known as *nuclear magnetic resonance*. The magnitude of the transverse spin magnetization is determined by the amplitude and duration of the RF. The angle between the magnetization vector and the imaging field, which is known as the *flip angle*, is

$$\theta = \gamma B_1 \tau \,, \tag{3.8}$$

where B_1 is the amplitude of RF, and τ represents the RF pulse duration. The spin magnetization after RF is

$$\begin{aligned} M_{xy} &= M_0 \sin\theta = \frac{\rho_0 \gamma^2 \hbar^2}{4kT} B_0 \sin\theta \\ M_z &= M_0 \cos\theta = \frac{\rho_0 \gamma^2 \hbar^2}{4kT} B_0 \cos\theta \end{aligned} \,. \tag{3.9}$$

For individual protons, a RF pulse induces two important effects. First, some protons absorb energy from the RF pulse and jump from the low energy state (spin up) to the high energy state (spin down). As a result, the number of excess up spins is reduced, and the longitudinal component of the spin magnetization is decreased. Second, the RF pulse

induces coherency between the spin precession phases, which produces a rotating transverse component of the spin magnetization. However, the two effects do not last long; they disappear over a short time because of spin-spin and spin-lattice interactions (see below). This recovery process is commonly referred to as *relaxation*.

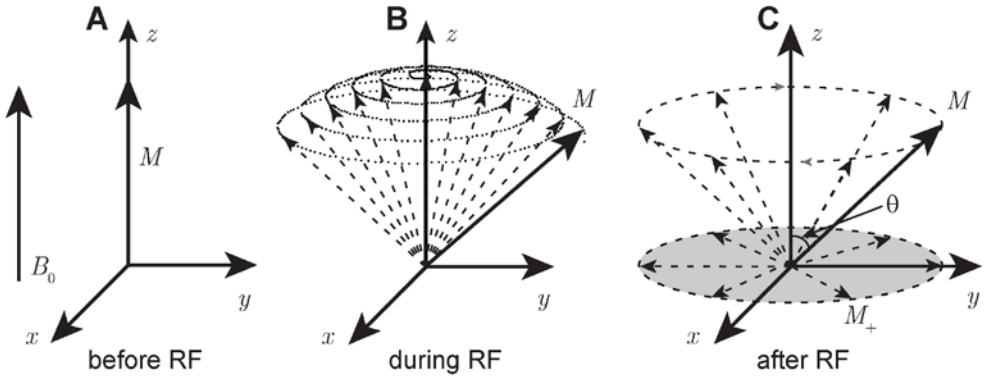

Figure 3-2 Magnetization excitation using a RF pulse.

Shown are the magnetization behaviour before (A), during (B) and after (C) a RF pulse.

The spin magnetization corresponds to the vector sum of the individual spin magnetic moments (see Equation (3.6)). If all of the spins are assumed to be independent, then the spin magnetization is governed by the same motion equations as individual spins, i.e.:

$$\begin{aligned} \frac{d\vec{M}_{xy}}{dt} &= \gamma \vec{M}_{xy} \times B_0 \hat{z} \\ \frac{dM_z}{dt} &= 0 \end{aligned} . \qquad (3.10)$$

However, the spins are far from independent, and the dynamics of spin magnetization are influenced by many other forces. First, because protons are in thermal contact with other particles, their spins can exchange energy with the surrounding background thermodynamic lattice. These spin-lattice interactions lead to the redistribution of the up and down spin states, which recovers the longitudinal component of the magnetization vector. It can be proven that the recovery speed is a function of $(M_0 - M_z)$, i.e.:

$$\frac{dM_z}{dt} = \frac{(M_0 - M_z)}{T_1}, \qquad (3.11)$$

where T_1 represents an empirical constant characterizing the longitudinal, or spin-lattice, relaxation time. Furthermore, spins can also interact with each other in a manner similar to thermal motion. The spin-spin interactions reduce the coherency between the proton

precession phases and lead to the decay of the transverse component of magnetization. The magnetization transverse decay rate is proportional to the magnitude of the transverse component. Incorporating the decay factor, the equation of motion of the transverse magnetization becomes:

$$\frac{d\vec{M}_{xy}}{dz} = \gamma \vec{M}_{xy} \times B_0 \hat{z} - \frac{\vec{M}_{xy}}{T_2}, \tag{3.12}$$

where T_2 represents an empirical constant characterizing the transverse or spin-spin relaxation time. Equations (3.11) and (3.12) can be combined into a vector equation:

$$\frac{d\vec{M}}{dt} = \gamma \vec{M} \times \vec{B}_0 + \frac{1}{T_1}(M_0 - M_z)\hat{z} - \frac{1}{T_2}\vec{M}_{xy}. \tag{3.13}$$

Equations (3.11), (3.12) and (3.13) are referred to as the *Bloch equation*, which has the solution

$$\begin{aligned} M_x(t) &= M_{xy}(t)\cos(w_0 t + \psi_0) \\ M_y(t) &= M_{xy}(t)\sin(w_0 t + \psi_0) \\ M_z(t) &= M_0 - (M_0 - M_{z0}) \cdot \exp(-t \,/\, T_1) \end{aligned}, \tag{3.14}$$

where

$$M_{xy}(t) = M_{xy0} \exp(-t \,/\, T_2), \tag{3.15}$$

where M_{xy0} and M_{z0} correspond to the transverse and longitudinal components of the magnetization after the RF pulse, respectively, and ψ_0 corresponds to the phase of the transverse magnetization after the RF pulse.

Beside the spin-spin interaction, transverse relaxation is also influenced by microscopic magnetic field heterogeneity arising from imaging field imperfections, tissue magnetic susceptibility variations, amongst other effects. For individual protons, magnetic field heterogeneity introduces frequency shifts to the precessions of the spins (see Equation (3.3)); therefore, the spin precessions are no longer have the same frequency; instead, their frequencies are distributed within a band of frequencies. The overall effect of the frequency shifts on a MRI signal depends on the magnetic field distribution within a voxel. If the frequency shifts are uniform within the voxel, then they produce an additional phase shift to the corresponding signal. If the frequency shifts vary, the spin precessions accumulate as phase dispersions (differences between the phases of the spin precessions)

over time. The phase dispersions can increase the speed of transverse magnetization relaxation as well as the signal decay (see Figure 3-3). Therefore, magnetic field heterogeneity may produce a phase change in and/or an enhanced decay of MRI signals. Traditionally, the signal decay is described as an additional relaxation time (T_2') similar to the spin-spin relaxation time. By incorporating this terminology, the transverse component of magnetization decays behaves according to

$$M_{xy} = M_{xy0} \exp(-t / T_2^*), \tag{3.16}$$

where

$$1 / T_2^* = 1 / T_2 + 1 / T_2', \tag{3.17}$$

where T_2^* is commonly referred to as the apparent T_2, and T_2' represents a parameter characterizing the transverse magnetization decay due to magnetic field heterogeneity.

A major difference between the relaxation caused by spin-spin interaction (characterized by T_2) and magnetic field heterogeneity (characterized by T_2') is their temporal characteristics. Spin-spin interactions, similar to Brownian motion, are intrinsically stochastic; therefore, spin-spin interaction-induced relaxation cannot be deduced. However, magnetic field heterogeneity-induced relaxation can be determined because the magnetic field heterogeneity typically remains unchanged throughout the relaxation process, and its effect on magnetization may be reversed and cancelled out through the use of a refocusing RF pulse (see Figure 3-5).

The signal generated by a relaxing magnetization is referred to as the *free-induction decay* (FID) signal. A general illustration of the FID process is described as follows: after the application of a RF pulse, the excited magnetization vector precesses around the imaging field at the Larmor frequency. Simultaneously, because of the spin-lattice interaction, spin-spin interaction, and magnetic field inhomogeneity, the magnetization gradually releases the additional energy absorbed from RF and returns to the initial state, i.e., the state preceding the application of the RF pulse. During this process, the transverse component of magnetization decays exponentially, and the longitudinal components grow exponentially (see equation (3.14)). The relaxation process is crucial for MRI signal generation because it is the period of time in which MRI signals are modulated

based on information from tissues and their micro-environments, which are then deconstructed from the measured MRI signals and presented as MRI images.

MRI detects signals produced by transverse magnetization using RF coils placed in the transverse plane (x-y) (see Figure 3-3). Because the transverse magnetization rotates at the Larmor frequency, the MRI signals also oscillate at the same frequency. A general expression of the signal is

$$S(r,t) = s(r,t) \cdot \sin\left[\omega_0 t + \psi(r)\right] \tag{3.18}$$

where $s(r,t)$ corresponds to the signal magnitude and ψ represents the signal phase offset. Because the oscillation frequency of a MRI signal (i.e., the Larmor frequency) (on the order of 10 MHz) is orders of magnitude faster than the change rate of the signal magnitude (on the order of 1 kHz), the signal magnitude and the phase are co-invariant. Thus, they can be treated as independent variables.

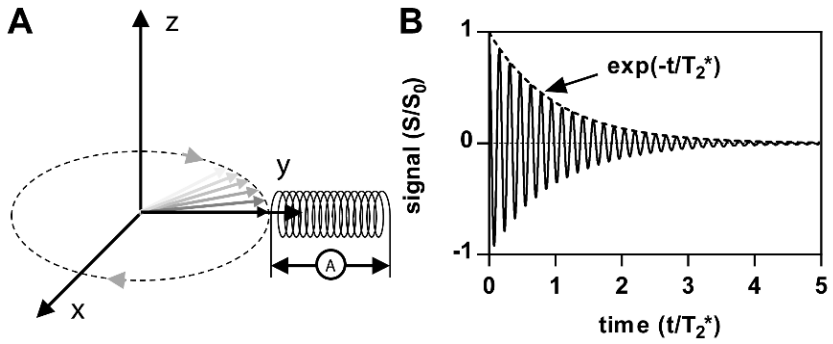

Figure 3-3 MRI signal during FID.

Shown are (A) the simplest MRI signal detection mechanism and (B) the MRI signal during FID.

MRI uses magnetic field gradients to encode spatial information about magnetization into MRI signals. Typically, three magnetic field gradients, the slice selection gradient, the phase-encoding gradient, and the frequency-encoding gradient, are used to resolve the voxel locations within the magnetic resonance images. The slice selection gradient is used with a RF pulse to selectively excite a thin slice of the object. Then, the phase-encoding gradient and the frequency-encoding gradient are applied multiple times to modulate the spatial magnetization of the slice to produce a series of MRI signals, which are used to generate a MRI image via Fourier transformation. The application of magnetic field gradients is the topic of pulse sequence design, and such an in-depth discussion is

beyond the scope of the present thesis. For a detailed description of the action of magnetic field gradients, the reader may wish to review a classic MRI textbook (Haacke et al., 1999; Bernstein et al., 2004).

3.1.3 Gradient echo and spin echo sequences

RF pulse and magnetic field gradient are two major components of MRI pulse sequences. MRI *pulse sequence* is a program of RFs and field gradients that is used to produce a MRI image. Pulse sequences allow MRI to generate images weighted by different types of contrasts. Pulse sequences remain an active research field today, and their extent is so vast that specific sequences and parameter settings have been established to detect contrasts between different types of tissue. Here, the two fundamental pulse sequences, gradient echo (GRE) and spin echo (SE) sequences, are briefly described.

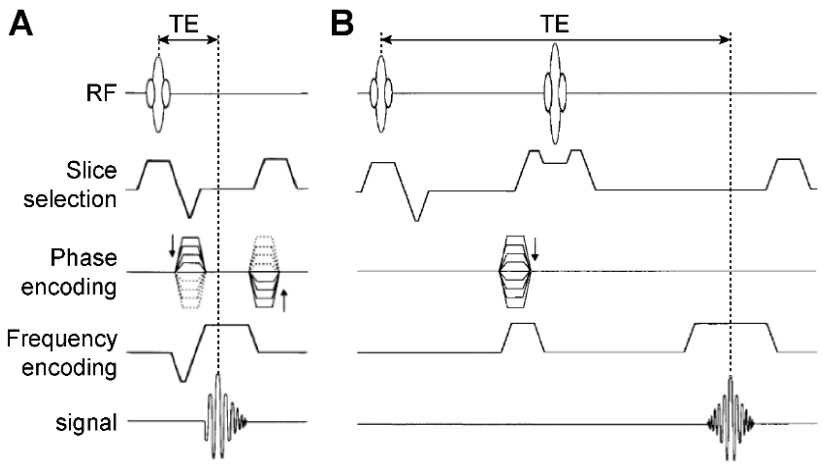

Figure 3-4 GRE and SE sequences.

Shown are examples of a gradient echo sequence (A) and a RF spin echo sequence (B) (figure reproduced from Bernstein et al., 2004).

The gradient echo sequence, also known as the gradient recalled echo (GRE) sequence, only uses a RF pulse to excite the magnetization at the beginning of a scan, and it does not use refocusing RF pulse (see below). A typical GRE sequence is presented in Figure 3-4A. The echo in the GRE sequence is produced by two sequential but opposite frequency-encoding magnetic field gradients. Frequency-encoding gradients are used to encode spatial information about the magnetization into MRI signals by slightly changing their precession frequencies to an extent that depends on the locations of the

magnetizations. The first gradient, sometimes referred to as the pre-phasing gradient, is used to prepare the magnetization for recording. It is intended to introduce phase dispersions into the spin precessions, which is then refocused by the second opposite magnetic field gradient. Because the two gradients are designed to be equivalent but with an opposite polarization, their effects on the magnetization cancel out. With respect to the echoes, the signal decays according to $\exp(-t_E / T_2^*)$, where t_E is the echo time.

MRI data acquired using a GRE sequence are typically weighted by multiple contrasts, including proton density, T_1, and T_2*. Based on the appropriate choice of echo time and repetition time, T_1-weighting can be enhanced or decreased, while contrast due to T_2^* is reduced or enhanced. Moreover, the GRE sequence is also sensitive to the susceptibility effect and can be used to produce susceptibility-weighted images.

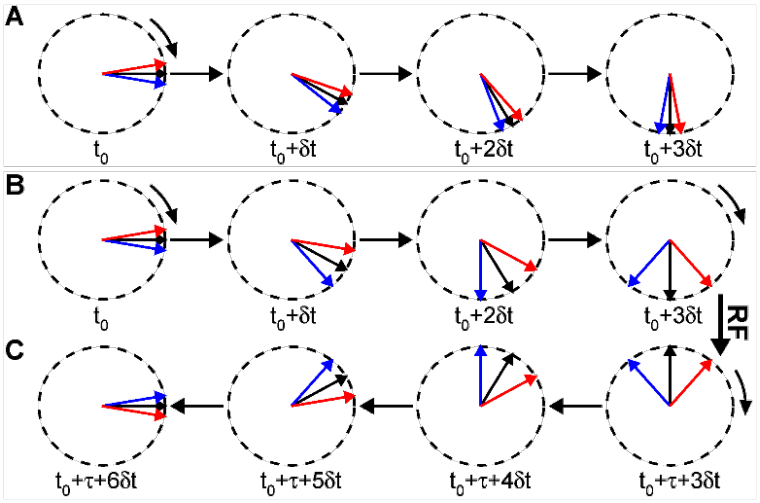

Figure 3-5 Effects of a refocusing RF pulse on spin precessions.

Shown are the precessions of a magnetization composed of three spins. In (A), the three spins have the same precession frequency (no dispersion); in (B), their precession frequency is slightly different, which leads to phase dispersion over time; and in (C), a 180 degree RF pulse reverses the precession phases of the protons and revokes the phase dispersion at the time of an echo.

The spin echo (SE) sequence, or the RF spin echo sequence, contains an additional 180 degree RF pulse, often referred to as the refocusing RF pulse, which is used to revoke the signal loss due to magnetic field heterogeneity (see Figure 3-4B). The refocusing RF pulse can reverse the precession phases of individual spins, and it also reverses the phase dispersion that accumulates due to the precession frequency shift. Therefore, the phase dispersion that accumulates after the RF pulse can cancel out the phase dispersion that accumulates between the excitation RF pulse and the refocusing RF pulse (see

Figure 3-5). When the dispersion accumulation time preceding and following the refocusing RF pulse is equal, the phase dispersions are maximally cancelled out, and an echo occurs. At the time of an echo, the signal decays according to $\exp(-t_E / T_2)$. The major advantage of the use of SE sequences is that the images can be weighted by proton density, T_1 or T_2, depending on the TR and TE values used. SE images are also more resistant to artifacts caused by an imperfect RF pulse and imaging field heterogeneity (see, for example, Bernstein et al., 2004).

GRE and SE sequences can be used with the echo-planar imaging (EPI) technique, a fast acquisition technique, to produce a GE-EPI or SE-EPI sequence. While conventional GRE and SE sequences must be applied multiple times (depending on the image matrix) to acquire data for a slice, GE-EPI and SE-EPI sequences can complete a slice using a single application. For EPI acquisition, the magnetization of a slice is first prepared using a conventional GRE, SE or other sequence, and then, a gradient echo train is used to acquire the data for a slice. Use of an EPI sequence can speed up the image acquisition process by hundreds of times, but the images are typically noisier than conventional GRE or SE images. EPI sequences are widely used when fast data acquisition is required, such as for functional imaging.

3.2 Blood-Oxygen-Level-Dependent (BOLD) Functional MRI (fMRI)

While the feasibility of nc-MRI remains under debate, BOLD fMRI, or simply fMRI, is the predominant method for non-invasive imaging of neuronal activity. Functional MRI detects neuronal activity indirectly via the BOLD effect. In this section, I provide a brief review of the neuronal basis of the BOLD signal, but for further details, the reader may wish to review fMRI textbooks (Buxton, 2009; Huettel et al., 2009) and classic articles (Menon and Kim, 1999; Logothetis et al., 2001; Arthurs and Boniface, 2002; Logothetis, 2008).

3.2.1 BOLD contrast

The BOLD effect is an endogenous contrast of regional neuronal activation in the brain. The BOLD effect directly relates to the energy consumption mechanisms in the brain. Neurons are highly energy-demanding cells. The brain consumes approximately 20% of all of the energy used in the human body (Drubach, 2000). This energy is provided via the metabolism of glucose, either oxidatively or non-oxidatively. Oxidative metabolism requires

a large amount of oxygen and produces three adenosine triphosphate (ATP) molecules (the intracellular energy carrier), while non-oxidative metabolism does not require oxygen and rapidly provides a single ATP. During the resting state, most glucose is oxidized, and the consumption rates of glucose and oxygen match their supply rates from cerebral blood flow (CBF); therefore, the blood-oxygen level remains stable. This balance is abolished during neuronal activity, as a large amount of glucose is metabolized non-oxidatively to meet the high demand of ATP. However, the oxygen and glucose supplies increase at the same rate. As a result, the oxygen concentration increases during neuronal activity. This oxygen overcompensation mechanism is the physiological basis of BOLD contrast. The brain is filled with capillary vessels that deliver oxygen and other nutrients to surrounding neurons. Typically, only nearby capillary vessels become more oxygenated during neuronal activity; therefore, their oxygenation is utilized as a marker to locate neuronal activity.

The blood-oxygen level increase has an important effect on MRI signals. Hemoglobin, the oxygen transporter in blood, is diamagnetic (with negative susceptibility) when oxygenated and paramagnetic (with positive susceptibility) when deoxygenated. When placed in a magnetic field, diamagnetic matter slightly counteracts the magnetic field, while paramagnetic matter slightly enhances the magnetic field. Because most matter in the brain is diamagnetic, paramagnetic deoxygenated hemoglobin (dHb) produces a larger magnetic field than other matter in the brain, which causes a distortion in the imaging field. As discussed in the previous section, the imaging field distortions can speed up the transverse magnetization relaxation, leading to a shorter T_2*. Therefore, blood containing a higher oxygen level (i.e., a lower dHb concentration) displays a longer T_2* (Ogawa et al., 1990b). During neuronal activity, the blood-oxygen level of local vessels increases, such that the T_2* of the vessels and surrounding tissues becomes longer. In T_2*-weighted MRI images, voxels containing these vessels and tissues produce a stronger signal than other voxels, which is used as an indicator of neuronal activity (Ogawa et al., 1990b). This effect is referred to as BOLD contrast.

The relationship between BOLD changes and neuronal activity has been examined using simultaneous fMRI and electrophysiological recording experiments. In the experiments by Logothetis et al. (2001), the time series of stimulated BOLD response in the primary visual cortex was measured in a monkey using a 4.7 T MRI scanner with a

GE-EP sequence, and intracranial electrode recordings were performed simultaneously. By comparing the BOLD signals to the LFP, the MUA, and other electrophysiological measurements, they found a strong correlation between the BOLD contrast and the electrophysiological signals in the same region, which demonstrated that the BOLD signal reflects an increase in local neuronal activity (Logothetis et al., 2001). Furthermore, they also found that the LFPs can better predict a BOLD signal than MUA. Because LFPs primarily represent the synaptic and postsynaptic activities of neurons in a given brain area (Kajikawa and Schroeder, 2011), the BOLD contrast likely reflects the synaptic input and the local processing rather than the spike output of the area (Logothetis et al., 2001).

3.2.2 Spatial and temporal properties of the BOLD signal

FMRI displays a good spatial resolution and a modest temporal resolution. Typically, fMRI images contain voxels of 2-5 mm in each direction, and enabled by EPI sequences, fMRI images of several slices can be acquired in seconds. However, BOLD fMRI images are indirect measurements of neuronal activity, as the activated brain regions are identified by a BOLD change. This prevents BOLD fMRI from producing images of neuronal activity with a high spatial or temporal resolution.

Although the latest MRI equipment is capable of acquiring images using sub-millimeter voxels, high spatial resolution fMRI images may not accurately inform neuronal activity locations (Disbrow et al., 2000; Kim et al., 2004). One assumption of BOLD fMRI is that the detected signal increases are produced by capillary vessels locally embedded in a functionally active region. However, the signal increases may also come from large vessels that are involved in the blood supply for the active region (Lai et al., 1993; Menon et al., 1993; Lee et al., 1995). These large vessel effects spatially blur the fMRI images, and this problem can be severe because large veins can be one to two centimeters away from the active brain region; the large vessels produce much brighter signals than the local capillary vessels of the active region. Although it is suggested that this problem may be avoided by targeting the “initial dip” of the BOLD response, which appears to be more spatially specific (Menon et al., 1995), this solution faces the challenge of detecting the small, short signal from the “initial dip” while avoiding detecting the much stronger signals from the main phase.

The temporal aspect of the BOLD fMRI signal has been extensively studied in the visual cortex. Using fast MRI imaging methods, such as EPI sequences, the time course of the BOLD response can be accurately determined, and an example is shown in Figure 3-6. The BOLD response is typically delayed by several seconds after the onset of a stimulus, and it lasts for several seconds after a stimulus. This response delay is thought to be caused by chemical processes occurring during the hemodynamic response to stimulus. As shown in Figure 3-6, even under short stimulation, the BOLD response lasts for approximately 20 seconds. This time delay means that fMRI cannot distinguish between two neuronal events that occur within several seconds. Although many researchers have attempted to improve the temporal resolution of the BOLD signal by de-convolving the BOLD response using a hemodynamic response function (HRF), this paradigm may predict inaccurate time courses of neuronal activity because the relationship between the BOLD signal and neuronal activity may be not linear (Yesilyurt et al., 2008).

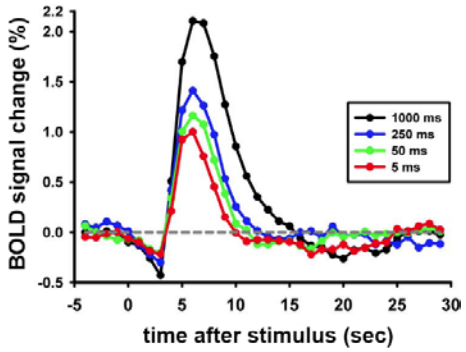

Figure 3-6 Time course of the BOLD response.

Shown are the average time course of BOLD signal changes in active voxels of the visual cortex under 5 msec, 50 msec, 250 msec, or 1000 msec of visual stimulation (figure reproduced from Yesilyurt et al., 2008).

3.3 nc-MRI experiments

Theoretically, nc-MRI can image neuronal activity without the limitations of BOLD fMRI. The technique aims to detect MRI signal changes caused by neuronal currents. Because neuronal currents represent the direct and localized effects of neuronal activity, nc-MRI has the potential to map neuronal activity at a higher spatial and temporal resolution than existing neuroimaging methods (Bandettini et al., 2005). Successful implementation of nc-MRI may benefit the study of brain function and may also have important clinical applications, such as the non-invasive mapping of epileptic foci (Liston et al., 2004). To date, a convincing nc-MRI experimental method has yet to be established, although

multiple experimental protocols have been proposed. In this section, the existing nc-MRI experimental protocols and attempts are described.

MRI experiments have been performed on phantoms to test the capability of MRI techniques to detect small magnetic fields produced by ultra-weak electrical currents (Bodurka et al., 1999; Kamei et al., 1999; Bodurka and Bandettini, 2002; Konn et al., 2003). In the experiment by Bodurka and Bandettini (2002), a transient electric pulse train was introduced into a water phantom to mimic neuronal currents, and a low-frequency oscillating current was continuously presented to simulate respiration-induced magnetic fields changes, which represent a major source of noise when neuronal currents are detected *in vivo*. They found that a transient magnetic field change of 200 pT with a duration of 40 msec could be detected using a 3T MRI scanner. This encouraging finding indicates the possibility of MRI-based neuronal current imaging because the neuronal magnetic fields in the cortex are approximately of the same order of magnitude. They also found that compared to the GE-EPI sequence, the SE-EPI sequence is more sensitive to small transient magnetic fields and more resistant to respiration-induced noise. Other phantom experiments also revealed that the MRI signal phase was more sensitive than the signal amplitude for detecting small transient magnetic fields (Bodurka et al., 1999; Konn et al., 2003). These findings may facilitate the design of practical MRI experiments to capture neuronal currents. However, they must also be interpreted carefully because electrical currents on wires behave differently from neuronal currents in the brain with respect to their geometry and temporal pattern.

Encouraged by these promising phantom experiments, many researchers have tried to detect neuronal currents in the human brain via MRI. In a study by Xiong et al. (2003), visuomotor response-evoked neuronal currents were imaged using a GE-EPI sequence with a 1.9T MRI scanner (Xiong et al., 2003). Changes in the MRI signal magnitude were detected in four different regions (see Figure 3-7). However, a similar experiment was also performed by Parkes et al. (2007), and they only detected 10 evenly scattered activated voxels throughout the brain with few clusters ($P < 0.001$, uncorrected), which are likely to correspond to random noise. One possible reason for the discrepancy between these results is that Parkes et al. used an inter-stimulus interval (ISI) of one second, while Xiong et al. used two seconds, and two seconds may allow small BOLD signals to occur (Parkes et al., 2007). Other nc-MRI experiments have reported no signal change (Chu et al., 2004),

small changes in the signal magnitude (Liston et al., 2004; Chow et al., 2006), or small changes in the signal phase (Bianciardi et al., 2004).

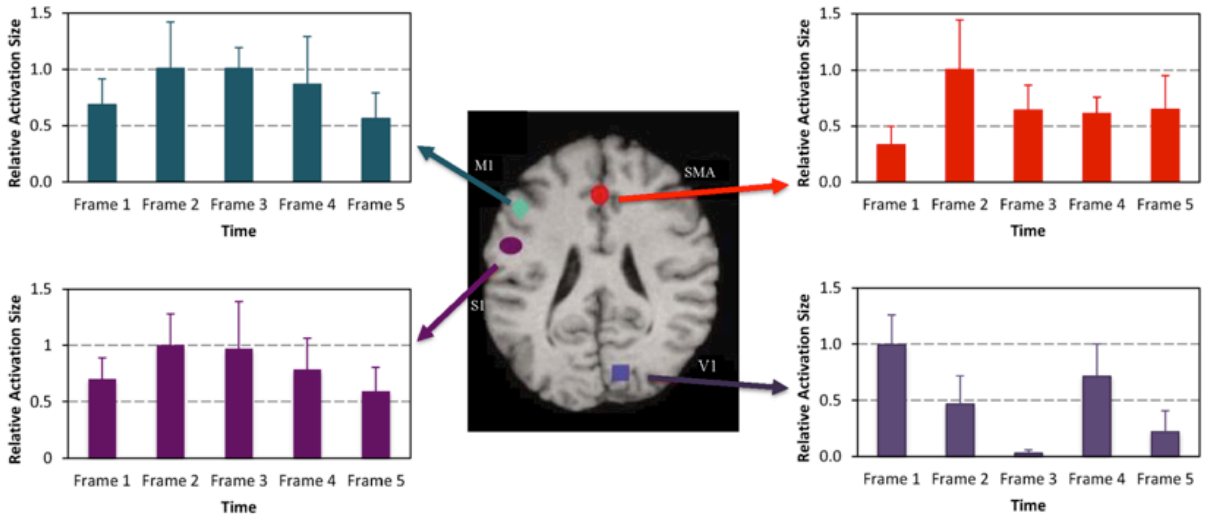

Figure 3-7 Brain regions activated during the visuomotor response, as observed by Xiong et al.

Shown are the sizes of the activated area of four brain regions: V1, M1, S1, and SMA. The activated areas were averaged across six subjects. The time frames 1-5 represent time intervals of 0-100 msec, 100-200 msec, 200-300 msec, 300-400 msec, and 400-500 msec after the visual stimulus onset, respectively (figure reproduced from Xiong et al., 2003).

To examine the neuronal current signal without the contamination of BOLD effects, nc-MRI experiments were also performed in prepared tissues devoid of blood. For example, Petridou et al. (2006) measured the neuronal current signals in organotypic rat brain cultures in which neuronal activity was elicited pharmacologically using tetrodotoxin (TTX). They detected a 3 to 14 mrad phase signal change and an absence of a signal magnitude change at 3T using a SE-EPI sequence. They also detected a 2.6 to 52 mrad signal phase change and a 0.01 to 0.4% signal magnitude change at 7T using FID. However, the magnitude of these changes may be caused by sources other than neuronal currents, such as temperature changes, water diffusion and physical motion, but these sources are unlikely to produce a systematic phase change. The experiments demonstrated that neuronal current-induced signal phase changes can be detected in vitro using currently available MRI techniques. A major challenge to achieve identical results in the living brain is the limited contrast-to-noise ratio (CNR) that can be achieved in the living brain as well as contamination by BOLD effects.

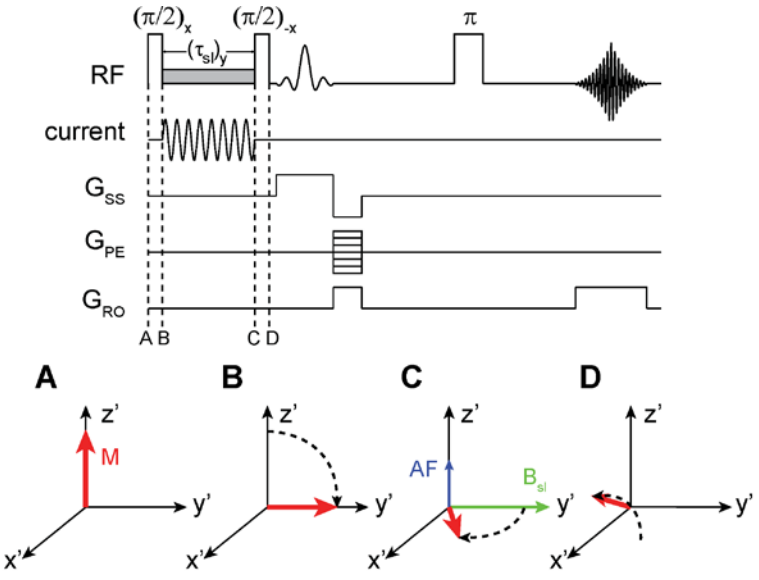

Figure 3-8 A SE sequence combined with a preceding spin-lock module.

In a spin lock module, the magnetization (red arrow) is first shifted to the transverse plane using a $(\pi/2)_x$ RF pulse, where the spin lock magnetic field (B_{sl}, green arrow) oscillating at the Larmor frequency is added. In the rotating frame, the spin lock magnetic field remains aligned along the y' axis. The audio-frequency (AF), at a frequency matching the spin lock field amplitude ($\omega_{sl} = \gamma B_{sl}$), induces the rotation of the magnetization around the z' axis. Then, a second $(\pi/2)_{-x}$ RF pulse projects and stores the y magnetization along the z axis in preparation for the imaging SE sequence. (figure reproduced from Halpern-Manners et al., 2010).

One challenge of detecting the neuronal current using conventional SE-EPI and GE-EPI sequences is that these sequences do not specifically target neuronal current signals; they also detect signals from other sources, for example physiological noise, the susceptibility effect and changes due to diffusion. One approach to avoid these interfering signals is to image neuronal currents using the stimulus-induced resonance saturation (SIRS) method (Witzel et al., 2008), which is a resonance mechanism in a rotating-frame. SIRS targets NMFs that oscillate at a specific frequency range. SIRS uses a spin-lock method to shift the NMFs to a longitudinal magnetization before a conventional SE or GE sequence is used to measure it (see Figure 3-8). In the spin-lock module, the oscillatory NMFs are used as a "RF" pulse to rotate the magnetization away from a spin-lock magnetic field (B_{sl}) in a frame rotating at the Larmor frequency around the imaging field (see Figure 3-8 and also (Witzel et al., 2008)). This mechanism is similar to the application of an RF pulse to rotate the magnetization away from the imaging field, except that it occurs in a rotating frame. The SIRS method has been demonstrated to be an effective method to image audio-frequency magnetic fields in a water phantom (Halpern-Manners et

al., 2010). However, the SIRS method suffers from low sensitivity, as the longitudinal relaxation time of the magnetization in the rotating-frame ($T_{1\rho}$) is very short (approximately 100 msec), limiting the spin lock time (τ_{sl}) used to modulate NMFs.

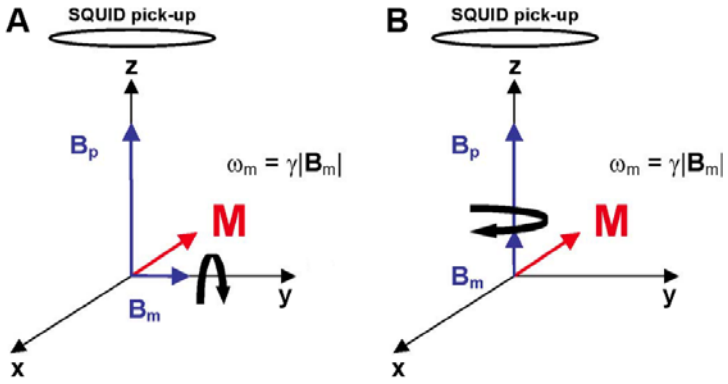

Figure 3-9 Two ULF MRI configurations for the detection of neuronal currents.

Pre-polarization fields (B_p) and imaging fields (B_m) can be orthogonal (A) or parallel (B). The orthogonal configuration is designed to capture the DC component of NMFs, while the collinear configuration is designed to capture the oscillating NMFs at a frequency matching the imaging field (figure reproduced from Kraus et al., 2007).

Nc-MRI experiments have also been performed using an ultra-low field (ULF) instrument (Kraus et al., 2008). ULF MRI must be performed in a magnetically shielded room, and the samples are first pre-polarized using a relatively strong magnetic field (B_p) of 30-300 mT before being imaged using a much smaller magnetic field (B_m), typically in the range of 1 to 100 μT. Because the MRI signal of the ULF is much weaker than that of high field MRI, a highly sensitive magnetometer, usually a superconducting quantum interference device (SQUID), is used for signal acquisition. Two ULF MRI mechanisms have been proposed for the imaging of neuronal currents (see Figure 3-9). The first mechanism uses the same configuration as other ULF MRI applications, such that the pre-polarized field is perpendicular to the imaging field. This method acquires images using the same sequence as the high field MRI except that the magnetization is induced by the pre-polarization field instead of a RF pulse. The second mechanism involves the use of the pre-polarization field parallel to the imaging field, and the magnetization can only be excited by NMFs that oscillate at a specific frequency as determined by the imaging field ($\omega_m = \gamma B_m$). The orthogonal configuration is designed to capture the direct current (DC) component of NMFs, and the parallel configuration can detect oscillating NMFs at frequencies matching the imaging field. Due to the limited signal-to-noise-ratio (SNR)

achieved using currently available hardware, ULF MRI has not been able to detect neuronal currents in the brain successfully. The feasibility of ULF nc-MRI depends on improvement of the experimental design and the signal detection technology.

In view of the conflicting results, it can be concluded that nc-MRI has yet to be convincingly demonstrated. The primary obstacle facing nc-MRI is that neuronal current-induced MRI signal change is very small relative to imaging fields and other effects contributing to MRI signal formation. It has been demonstrated in prepared tissue that the neuronal current signal is at least one order magnitude smaller than the BOLD signal (Petridou et al., 2006). To detect such small signal changes, sensitivity to signal has to increase and a lower signal-to-noise ratio must be attained. Another challenge is to separate the neuronal current signal from other concurrent signals. Aside from the BOLD signal, neuronal activity causes a temporal increase in water diffusion, which also leads to MRI signal changes (Darquie et al., 2001). The BOLD and diffusion signals may overshadow the neuronal current signals, making them undetectable. Therefore, a MRI protocol that specifically targets the neuronal current and avoids the concurrent BOLD and diffusion signals is a necessary component of a nc-MRI model. One strategy is to image the oscillatory component of the neuronal currents. Neuronal currents are thought to oscillate with neuronal activity, while BOLD changes and diffusion do not. The spin-lock method and ULF MRI are two possible candidates for this strategy, but both suffer from a limited signal-to-noise ratio. A new imaging protocol and/or new hardware are therefore required for nc-MRI experiments.

3.4 Neuronal current signal simulation

The failure of existing nc-MRI experiments was partly because the behavior of NMFs, which are expected to produce detectable MRI signal changes, is not fully understood. To bridge this gap, computer simulation has been used to study the behavior of NMFs as well as the potential nc-MRI signal. A theoretical framework for calculating the nc-MRI signal from a NMF is introduced in the following section. The different methods previously used to simulate neuronal currents, and their shortcomings, will then be described.

3.4.1 Neuronal current-induced MRI signal changes

The theoretical effects of NMFs on the MRI signal have been studied by several groups (Blagoev et al., 2007; Heller et al., 2009). In this sub-section, the theoretical framework is briefly described.

Generally, the complex MRI signal of a voxel can be written as (Haacke et al., 1999 pp.95):

$$S_0(t) = \omega_0 \int_{v_0} d^3r \, \exp\big[-t \,/\, T_2(\mathbf{r})\big] M_\perp(\mathbf{r},0) \mathcal{B}_\perp(\mathbf{r}) \, \exp\big[i\phi_0(\mathbf{r}) - i\omega_0 t + i\theta_{\mathcal{B}}(\mathbf{r})\big], \tag{3.19}$$

where ω_0 represents the Larmor frequency; $\mathcal{B}_\perp(\mathbf{r})$ corresponds to the transverse component of “signal acquired field”, which is determined by the shapes of the signal-receiving coils and their positions relative to the voxel (see Haacke et al., 1999); $M_\perp(\mathbf{r},0)$ represents the initial transverse magnetization that is induced by a RF pulse; and $\theta_{\mathcal{B}}(\mathbf{r})$ represents the initial phase of $M_\perp(\mathbf{r},0)$ that is detected by the coils. The presence of NMFs slightly changes the precession frequency of protons according to

$$\omega = \omega_0 + \Delta\omega = \omega_0 - \gamma B_z^{\mathrm{nc}}(\mathbf{r},t), \tag{3.20}$$

where $B_z^{\mathrm{nc}}(\mathbf{r},t)$ correspond to the components of the NMFs that are parallel to the imaging field of a scanner. This small frequency change modulates the magnetic resonance signals that contain information about the NMFs as

$$S(t) = \omega_0 \int_{v_0} d^3r \, \exp\big[-t \,/\, T_2(\mathbf{r})\big] M_\perp(\mathbf{r},0) \mathcal{B}_\perp(\mathbf{r}) \, \exp\left[i\phi_0(\mathbf{r}) - i\omega_0 t + i\theta_{\mathcal{B}}(\mathbf{r}) + i\int_{t_0}^{t} \Delta\omega \cdot dt\right], \tag{3.21}$$

where $[t_0, t]$ represents the NMF phase accumulation time that corresponds to the TE of the SE or GE sequence. The $\Delta\omega$ in the factor ω_0 outside the integral is ignored in this equation because it is much smaller than ω_0. Under an assumption of homogeneity, the voxel displays a homogeneous T_2 and “acquiring field”, and the magnetization is evenly excited such that the complex signal can be written as (Haacke et al., 1999):

$$S(t) = \omega_0 \exp\big[-t \,/\, T_2(\mathbf{r})\big] M_\perp(\mathbf{r},0) \mathcal{B}_\perp(\mathbf{r}) \, \exp\big[i\phi_0(\mathbf{r}) - i\omega_0 t + i\theta_{\mathcal{B}}(\mathbf{r})\big] \int_{v_0} d^3r \exp\left(i\int_{t_0}^{t} \Delta\omega \cdot dt\right). \tag{3.22}$$

Comparing equation (3.22) to equation (3.19) provides the term that contains the effects of the NMFs on the MRI signal:

$$\chi = \frac{S}{S_0} = \int_{v_0} d^3 r \exp\left[i\phi(\mathbf{r},t) \right], \tag{3.23}$$

where $\phi(\mathbf{r},t)$ represents the NMF-induced phase change, stated as

$$\phi(\mathbf{r},t) = \int_{t_0}^{t} \Delta\omega \cdot dt = -\int_{t_0}^{t} \gamma B_z^{\mathrm{nc}} dt \ . \tag{3.24}$$

The fractional magnitude change and phase change of the MR signal are

$$\begin{aligned} \Delta s &= \left| \frac{S - S_0}{S_0} \right| = \left| \chi \right| - 1 \\ \Delta\varphi &= \arg\left(\frac{S}{S_0} \right) = \arg(\chi) \end{aligned} \ . \tag{3.25}$$

Using a small angle approximation, $\exp(\mathrm{i}\,\phi) = 1 + \mathrm{i}\,\phi - 0.5\phi^2 + \cdots$, the MRI signal magnitude and phase change can be written as (Blagoev et al., 2007; Heller et al., 2009)

$$\begin{aligned} \Delta s &= 0.5\left(\left\langle \phi^2 \right\rangle - \left\langle \phi \right\rangle^2 \right), \\ \Delta\varphi &= -\left\langle \phi \right\rangle \end{aligned} \tag{3.26}$$

where $\left\langle \phi \right\rangle$ and $\left\langle \phi^2 \right\rangle$ denote the mean values of ϕ and ϕ^2 evaluated over the volume of the voxel. NMF-induced MRI signal changes, i.e., the nc-MRI signals, can be calculated using Equations (3.24) and (3.26).

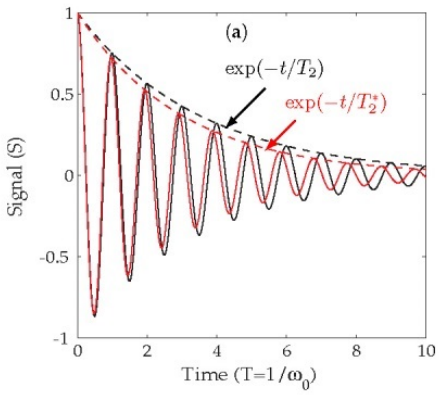

Figure 3-10 MR signals with or without NMFs.

Illustrated are the MRI signals of a voxel with (the red line) or without (the black line) NMFs.

3.4.2 Neuronal current modeling

The predominant challenge facing nc-MRI signal simulation is the accurate modeling of the spatial distribution and temporal variation of NMFs, as nc-MRI signals are functions of

the spatial and temporal integrals of the NMFs (see Equation (3.26)). Because the magnetic fields of neuronal currents can be determined based on the Biot-Savart's law, the key step to simulating NMFs is to determine the neuronal current distribution. In the literature, several paradigms have been used to simulate the neuronal current distribution.

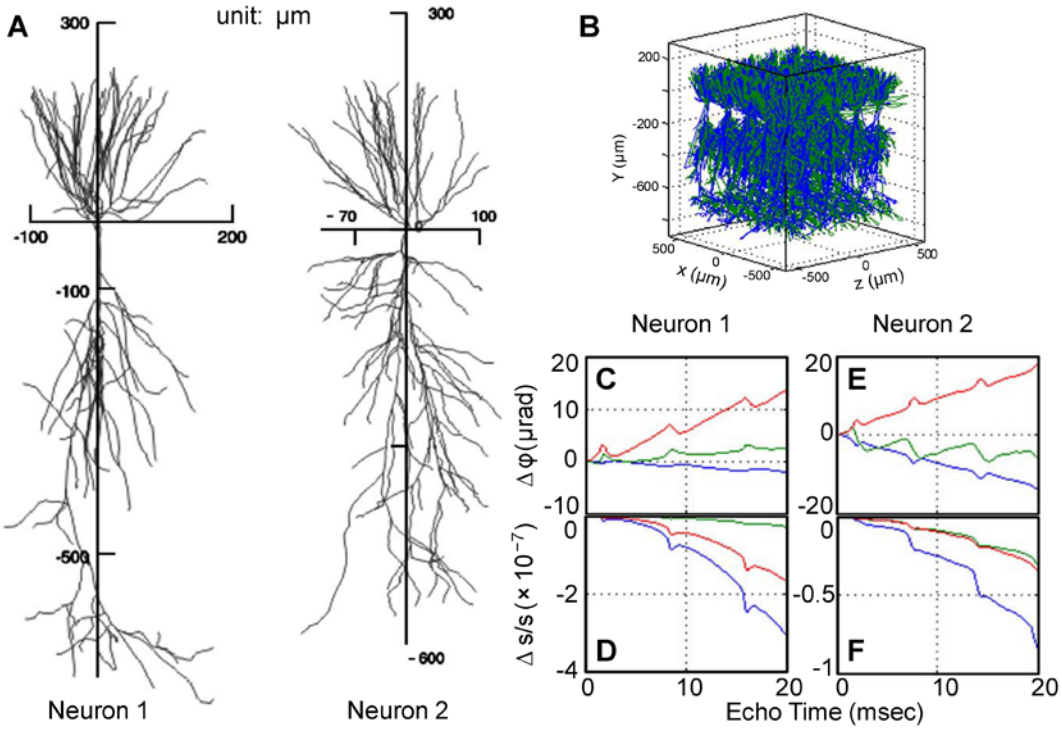

Figure 3-11 nc-MRI signal predicted using an identical neuron model.

Shown are (A) the structure of the two hippocampal CA1 pyramidal neurons, (B) an example voxel constructed by replicating and relocating a neuron, and the MRI signal phase changes (C and E) and magnitude changes (D and F) of a voxel using Neuron 1 (C and D) or Neuron 2 (E and F). The colour indicates the signal changes produced by different components of the NMFs: blue – x, green – y, and red – z. (figure reproduced from Cassara et al., 2008).

Neuronal currents have been simulated using an array of dendrites (Xue et al., 2006). This model assumes that the predominant neuronal currents are produced by the postsynaptic activity of dendrites through simplification of the currents produced by a dendrite to a small current dipole (see Xue et al., 2006), and their magnetic fields were calculated based on the Biot-Savart's law and used to estimate MRI signal changes. Two configurations were considered: parallel dendrites, in which the currents from the dendrites are aligned parallel to each other, and anti-parallel dendrites, in which the currents of adjacent dendrites are in opposing directions. The researchers found that the MRI signal change of the parallel configuration was more than twenty times larger than that of the anti-parallel configuration, and they predicted a 2% MRI signal magnitude change and a

negligible phase change (parallel dendrite, TE = 100 msec). The predicted magnitude change may be detectable using currently available MRI techniques.

Neuronal currents have also been simulated using “spherical dipoles”, a mathematical current source model consisting of uniformly distributed currents in a spherical volume (Heller et al., 2009). In this model, the neuron is simplified to a 30-branch dendrite, and each dendrite is considered to be a spherical dipole. This model allowed for either a random or specific spatial distribution of neurons, and it used MEG data to constrain the neuronal current strength. Calculations based on this model predicted a MRI signal magnitude change of 2×10^{-5} and a signal phase change of 2×10^{-3} rad. Only the signal phase change can be detected.

One disadvantage of the dendrite and current dipole models is that they ignore the structures of neurons and their arrangement in the brain, which may have a significant impact on the nc-MRI signal. In light of this limitation, several groups have simulated nc-MRI signals using neurons displaying realistic structural and physiological properties (Blagoev et al., 2007; Cassara et al., 2008; Luo et al., 2011b). For example, Cassara et al. (2008) simulated nc-MRI signals using two pyramidal neurons from the CA1 region of the hippocampus. They used the NEURON simulator (Hines and Carnevale, 1997) to generate a neuronal membrane potential distribution, from which the neuronal currents and magnetic fields were calculated. In this model, a neuron population was created by replicating a neuron thousands of times and distributing the neurons randomly in a small volume, which was treated as a voxel of a MRI image. The neurons in the voxel were aligned parallel to each other. The total NMFs, which were used to estimate MRI signal changes, were calculated by summing the NMFs of all of the neurons in the voxel (see Figure 3-11). This model predicted a MRI signal magnitude change of 2×10^{-7} and a phase change of 8×10^{-3} rad (voxel size = 1.7 mm^3, neuron density = 2084 mm^{-2}, TE = 20 msec). The authors also suggested that a new nc-MRI mechanism must be developed to detect the small signal and to avoid the noise from hardware instability and physiological processes.

These nc-MRI models may inaccurately predict the nc-MRI signals because they simulated neuronal currents by simplifying the underlying temporal and spatial variations. First, the models assumed that all neurons display identical firing patterns. Ignoring the firing differences between neurons may lead to unrealistic neuronal current time courses.

Furthermore, although neuronal morphology was considered in the models using actual neurons, the assumption that all neurons are of the same shape may lead to an unrealistic neuronal current spatial distribution.

In this thesis, I build on this notion to simulate MRI signals produced by realistic neuronal activity. Neuronal activity was simulated using a laminar cortex model, a new three-dimensional model that I developed. Rather than simulating the activity of single neurons, I decomposed neuronal activity into action potentials (APs) and postsynaptic potentials (PSPs). The geometries of the dendrites and the axons were dynamically generated to account for neuronal morphologies diversity. The magnetic fields associated with APs and PSPs were calculated during spontaneous and stimulated cortical activity, from which the neuronal current-induced MRI signal was determined. This method and its results are elaborated in the next two chapters.

Chapter 4

The laminar cortex model: a new continuum cortex model incorporating laminar architecture

4.1 Introduction

Neuronal activity in the brain display varied spatial and temporal patterns. Neurons can generate recurrent activity at frequencies from 0.1 hertz to several hundred hertz (Buzsaki and Draguhn, 2004). Neuronal activity also spatially varies across regions. The patterns of neuronal activity may have significant effect on neuronal current distribution, and thus may affect the nc-MRI signals. A reliable estimation of the signals requires realistic modelling of neuronal activity. However, a voxel of a MRI image contains more than 10,000 neurons, and simulating the dynamics of a large number of neurons faces the challenge of specifying the physiological parameters in large, inhomogeneous populations with diverse physiological properties (Connors and Gutnick, 1990). An alternative approach to simulating individual neuronal activity has been to simulate the activity in an ensemble of neurons. An example of this is the continuum cortex model, developed by Wright *et al* (Robinson et al., 1997; Rennie et al., 2000; Wright et al., 2003; Wright, 2009), which has been used to simulate ensemble activity at different scales (Wright, 2009). Existing continuum cortex models do not take into account the laminar architecture of the cerebral cortex. They are, therefore, limited in their ability to model the distribution of electric potential of the brain in three dimensions. Cortical neurons are organized in columns comprising as many as 20,000 neurons (Mountcastle, 1997; Meyer et al., 2010). Functionally, neurons in a column display similar responses to specific stimuli (Horton and Adams, 2005). In this paper, I build on this notion to expand the continuum cortex model by incorporating the laminar connection architecture of the cortex and simulating the collective of neuronal ensembles within cortical columns. To validate the model, I have used the new laminar cortex model (LCM) to simulate LFPs within the visual cortex under different conditions of visual stimulation, and compared them with empirical data.

4.2 Material and methods

4.2.1 Continuum cortex model

I give a brief overview of the continuum cortex model for completeness, but for specific details refer to (Wright, 2009). The continuum cortex model simulates the collective electrophysiological activities of the cerebral cortex. A population approximation is used to overcome the difficulty of simulating a large number of individual neurons, and to capture the essential aspects of cortical dynamics (Robinson et al., 1997; Rennie et al., 2000). The continuum cortex model divides the simulated cortical area into a $n \times n$ grid of elements, where n is an integer. Each element consists of two populations of neurons: excitatory and inhibitory (Wright, 2009). Each population is treated as a single entity capable of receiving spikes, changing membrane potential, and generating and propagating spikes (Wright, 2009).

The numbers of spikes propagating between neurons of two groups at any one time varies. In the continuum cortex model the effects of action potential shape and its temporal evolution are ignored. Instead, the average afferent spike rate (ϕ) is used to measure interaction between the two groups of neurons. The spike rate is defined as the average number of spikes a neuron of one group receives from a neuron of the other group per unit time.

The continuum cortex model contains four main components: 1) spike generation, 2) spike propagation, 3) generation of the postsynaptic potential, and 4) membrane potential aggregation. The equations describing each component are provided in Appendix A and were developed either by using theoretical approaches or by experimentally fitting observed data using an appropriate function. The mean field approximation was employed during this procedure (Wright, 2009).

4.2.2 Cortical laminar connection

The LCM exploits the laminar architecture of the cortex. Five cortical layers (layer I to VI) are considered (cortical layers II and III are combined). Each layer is simulated using the continuum cortex model, and the layers are connected by laminar synaptic connections (see Figure 4-1). A synaptic connection map is created and used to control the connection between and within cortical layers (see Table S1 in Appendix B). This

connection map was based on empirical observations of the number of synapses formed between different types of neurons by Binzegger (Binzegger et al., 2004) (see section of Appendix B for details). The connection map classifies the afferent synapses on each group of cortical neurons into three categories: 1) intracortical synapses, from within the visual cortex (ϕ_{ic}), 2) cortico-cortical synapses, from other cortical areas (ϕ_{cc}), and 3) thalamic synapses, projections from neurons in the lateral geniculate nucleus (LGN, ϕ_{th}).

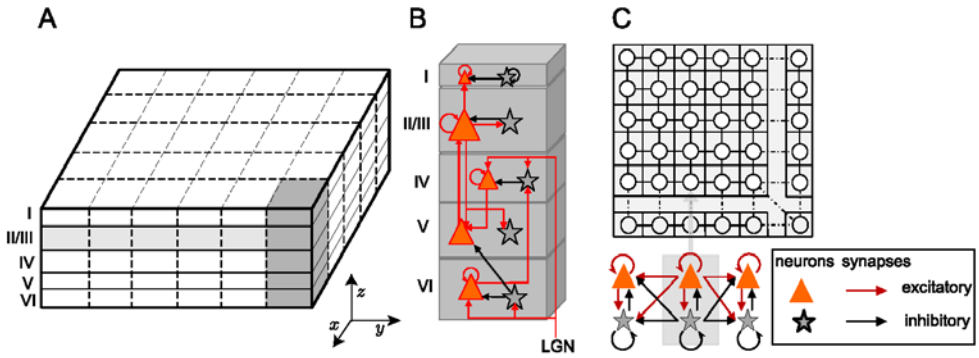

Figure 4-1 The configuration of the LCM.

(A) The LCM simulates five cortical layers. Cortical layers are discretized to a grid of elements, which contain two neuron groups: excitatory and inhibitory. (B) The laminar connection between cortical layers is illustrated. Only the strong connections are shown in the figure. For the complete connection map please refer to Table S1 of Appendix B. (C) The connections between neuron groups within a lamina are shown.

The LCM allows simulation of centimetre and column scale (micrometre) cortical regions (Wright, 2009). Since the grid elements of the centimetre scale model correspond to the size of cortical columns, the connections between cortical laminae are assumed to be local. This means that elements in the same horizontal position of all cortical layers are connected vertically (see Figure 4-1B). In contrast, the column scale implementation is approximately the size of one cortical column. Therefore, connections between cortical layers are global, and the average spike rate of a cortical layer is the input to other cortical layers. The work here is focused on simulating LFPs produced in the visual cortex. Hence, results are limited to the application of the centimetre scale model.

4.2.3 Visual stimulus

I simulated the effect of visual stimulation on LFPs using the LCM. Different forms of visual stimulation were assumed to form different spike trains projecting from the LGN to deeper cortical layers of the visual cortex (Layer IV, V and VI, see Table S1 in Appendix B). Three states of visual stimulation were examined in the model: 1) spontaneous activity

without visual stimulation, 2) constant visual stimulation, and 3) intermittent light stimulation. As illustrated in Figure 4-2, these conditions correspond to afferent spike trains with the shape of small amplitude white noise, large amplitude white noise (the random number generator from (Leemis and Park, 2006) was adopted), and recurring Gaussian peaks, respectively.

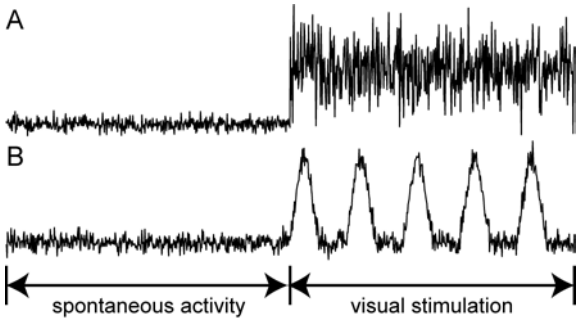

Figure 4-2 Afferent spike rates corresponding to visual stimulations.

(A) Spike rates correspond to spontaneous activity followed by constant visual stimulation, and (B) spike rates represent to spontaneous activity prior to intermittent light stimulation.

Apart from the synapses projecting from neurons in LGN and the visual cortex, there are also a large number of synapses originating from other cortical areas (see Table S1 in Appendix B). I assume that spikes from these synapses contribute to background noise, which was modelled as low-amplitude white noise.

4.2.4 Model parameters

The LCM has over 150 parameters, which fall into four categories relating to: 1) electrophysiological properties of neurons, 2) spike propagation, 3) synaptic transmission, and 4) connections between cortical laminae. Most of these parameters were estimated from experimental data, while others were left as free parameters. However, the cortex is complex, to the extent that the simplified parameters may not represent its physiology, morphology and architecture exactly. I found that a small deviation of the parameter values do not change the results reported here significantly. This is because a similar LFP outcome can be achieved by tuning free parameters.

Parameters relating to the electrophysiological properties of neurons are well established in the literature. I used the same values, derived from experimental data, as the continuum cortex model (Wright, 2009).

Spike propagation parameters and their values used are listed in Table 4-1. The propagation speed of spikes in the horizontal (lateral) direction (v_{h}) was set to 0.24 m/s, which is consistent with experimental measurements of the speed of spread of spikes in the cortex (Hirsch and Gilbert, 1991; Nauhaus et al., 2009). Since collateral branches are usually smaller in diameter than the main axon, the speed of vertical (inter-laminar) propagation of spikes (v_v) was set to 1.2 times the speed of horizontal propagation. The spike propagation range parameters were set to the similar values as continuum cortex model (Wright, 2009).

Parameter	Representing	Value
v	Spike propagation speed	Horizontal: $v_{\mathrm{h}} = 0.24\ \mathrm{m/s}$ Vertical: $v_{\mathrm{v}} = 0.288\ \mathrm{m/s}$
γ	Spike propagation range	Excitatory: $\gamma_{\mathrm{e}}^{\mathrm{h}} = 2\times10^{-3}\ \mathrm{m}$ Inhibitory: $\gamma_{\mathrm{i}}^{\mathrm{h}} = 1\times10^{-3}\ \mathrm{m}$

Table 4-1 Spike propagation parameters.

There is a wide range of published values for synaptic transmission parameters (Thomson et al., 1996; Thomson, 1997). I chose the middle parameter value when a range was provided and the average when multiple values were reported. The excitatory and inhibitory synaptic gains g_{e} and g_{i}, were treated as free parameters. Their values were determined by fitting experimental data to the LFPs generated using the LCM.

The best set of parameter values was selected as those fulfilling the following criteria: 1) the LFP power spectrum fitted the $1/f^{-n}$ function with $R^2 < 0.1$ (Buzsaki et al., 2012). 2) with simulated visual stimulation, there was an increase in gamma frequency in the power spectrum; 3) membrane potentials of neuron groups were less than 10mV above their resting membrane potentials (Carandini and Ferster, 2000).

4.2.5 Simulation

The simulation program was written using the ANSI C language and compiled with the Intel C compiler (http://software.intel.com/intel-compilers/). The program was compiled and executed on a Linux workstation (Dell® Precision T7500) with Ubuntu version10.10 (x86_64, http://www.ubuntu.com). OpenMP (http://www.openmp.org), a shared-memory

parallel programming library, was used to parallelize the code to speed up program execution.

In this paper, the LCM was used to simulate a cortical area of size 1×1 cm^2. The domain was discretized to a 20×20 grid. At the beginning of each execution of the program, the simulation time was initialized to zero, and every neuron state variable was set to its resting state value (see Appendix B). The iteration time step was 1 msec. After initialization, the program executed without particular visual stimulation for 60 seconds at which time the system is assumed to have reached steady state. Constant visual stimulation or intermittent light stimulation was then applied for 20 seconds (time = 60-80 sec). LFPs were simulated for conditions of spontaneous activity and for each mode of visual stimulation.

4.2.6 Data analysis

In the simulation, the membrane potentials of all neuron groups in the middle element of a layer are recorded during the entire execution. Data of the last 1.024 second prior to visual stimulation and after stimulation were used for frequency spectrum analysis.

For comparisons with experimental data, the LFPs of the simulated cortical area are assumed to be the average of neuronal membrane potentials of the central elements of all layers, stated as:

$$LFP = \frac{\sum_{\text{all } ly} N_{ly} V_{ly}}{\sum_{\text{all } ly} N_{ly}} \tag{4.1}$$

where N_{ly} are the numbers of neurons in the central element of layer ly and V_{ly} are the potentials of the central elements of layer ly, which is the average of membrane potentials of neurons in the element, that is

$$V = \frac{N_{\mathrm{e}} V_{\mathrm{e}} + N_{\mathrm{i}} V_{\mathrm{i}}}{N_{\mathrm{e}} + N_{\mathrm{i}}} \tag{4.2}$$

where N_{e}, N_{i} are the numbers of excitatory and inhibitory neurons and V_{e} and V_{i} are the (average) membrane potentials of excitatory and inhibitory neuron populations respectively. The frequency spectrum of the LFPs was computed using the *fast Fourier transform* as

implemented in MATLAB 2010a (http://www.mathworks.com). The LFP frequency power spectra were compared with experimentally measured data.

LFPs produced by LCM were also used to estimate current source density. The standard one-dimension current source density calculation method was used (Nicholson and Freeman, 1975; Mitzdorf, 1985b)

$$I_i = -\sigma \frac{\partial^2 u}{\partial z^2} = -\sigma \frac{u_{i-1} - 2u_i + u_{i+1}}{h^2}. \tag{4.3}$$

Here σ is electric conductance of the cortex, and was set to 0.3 S/m, u_i is the potential at the $i\mathrm{th}$ point, and h is the distance between two adjacent points. To reduce spatial noise, the three-point Hamming filter was applied (Rappelsberger et al., 1981; Ulbert et al., 2001)

$$u^{\mathrm{filt}}{}_i = 0.23u_{i+1} + 0.54u_i + 0.23u_{i-1} \tag{4.4}$$

4.3 Results

4.3.1 Parameter sensitivities

I examined the behaviour of the LCM using different parameter values. For each parameter combination, around 100 executions of the LCM were conducted, and the average LFP frequency spectrum was computed.

Figure 4-3 shows the power spectra of the LFPs obtained with different synaptic gains. The LCM was able to generate LFPs with different types and envelopes of oscillation, depending on the combination of excitatory and inhibitory synaptic gains used in the simulation. For example, when either excitatory or inhibitory synaptic gain was small, the frequency spectrum of background activity had an inverse-frequency shape. Stimulation resulted in an increase in gamma frequency. In contrast, when the excitatory and inhibitory synaptic gains were both large, particular frequency peaks dominated the LFP power spectra. Thus, variations of synaptic gains had a strong impact on LFP frequencies.

For large synaptic gains, the peaks in the power spectra did not change position with variation in synaptic gain. Dependence of peak position on other parameters was also examined by generating LFP power spectra with different parameter values. The time course of the postsynaptic potential (PSP) was found to be strongly correlated with the positions of the peaks. Peak frequency decreased with increasing PSP time course. (Four

examples of LFP power spectra with different PSP time courses are shown in Figure S2 of Appendix C). This suggests that the dominant oscillation frequency is controlled by the feedback between excitatory and inhibitory neurons.

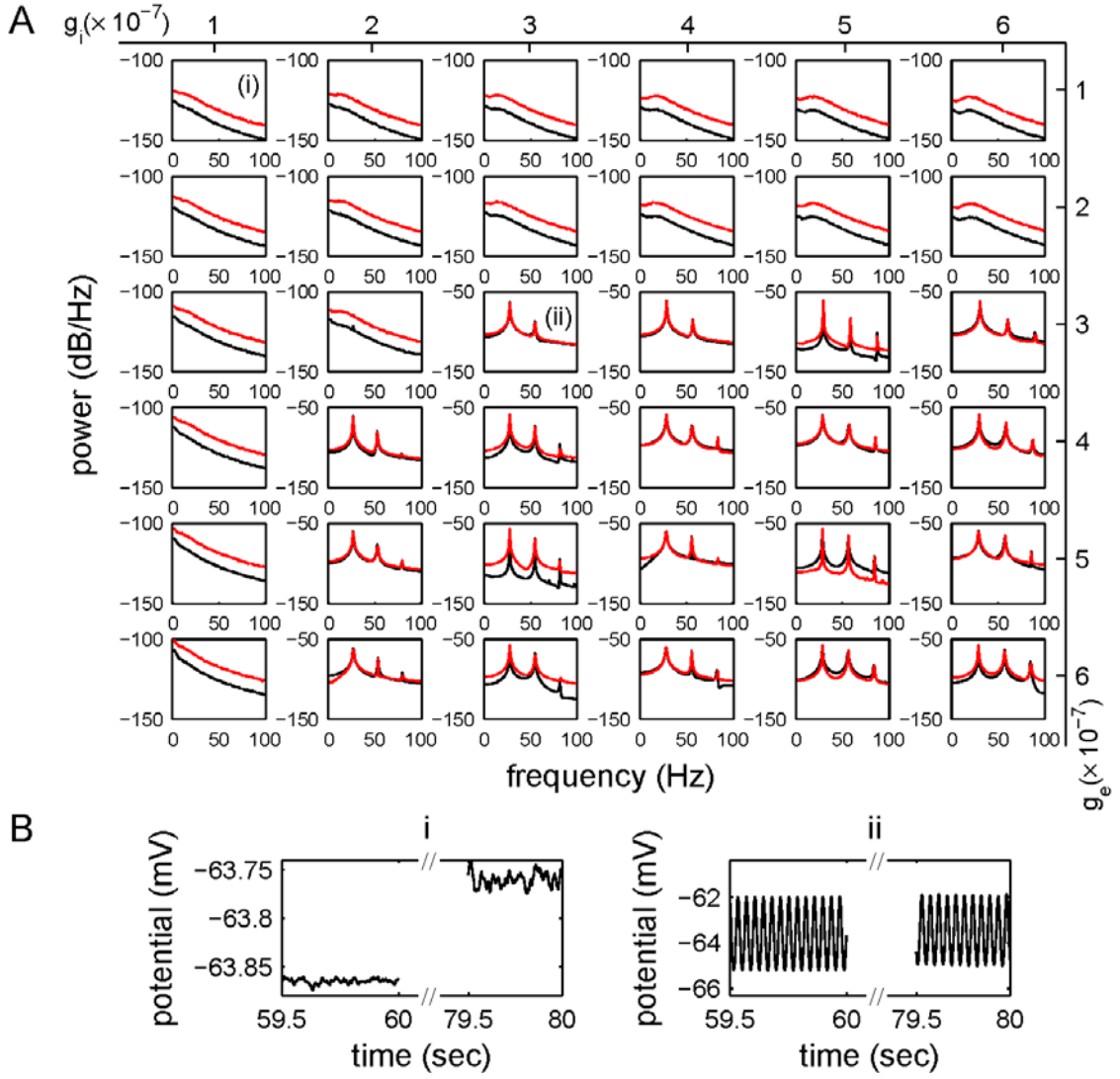

Figure 4-3 The effect of changing synaptic gains on the LFP power spectra.

(A) LFP power spectra were obtained using LCM with different combinations of excitatory (g_e) and inhibitory (g_i) synaptic gains. Black lines show the power spectra of spontaneous LFPs and red lines correspond to the activated LFPs. A more detailed synaptic gain dependent frequency map is provided in Figure S1 of Appendix C. (B) The time serials of LFPs obtained in one run with two synaptic gain combinations (i) $g_e = g_i = 2\times10^{-7}$ V/spike, and (ii) $g_e = g_i = 3\times10^{-7}$ V/spike, as corresponding to sub-figures (i) and (ii) in (A).

The shape of the power spectrum of LFPs generated by the LCM is controlled by the balance between excitatory and inhibitory postsynaptic potentials (PSPs). These are

influenced by many parameters simultaneously, including synaptic gains, spike propagation ranges and synapse numbers. Changes in PSPs caused by variation of one parameter could be compensated by other parameters. For example, increase of synaptic gains may not change PSP when the corresponding synapse number is decreased. Therefore, the LCM could produce similar LFPs using different combinations of parameter values.

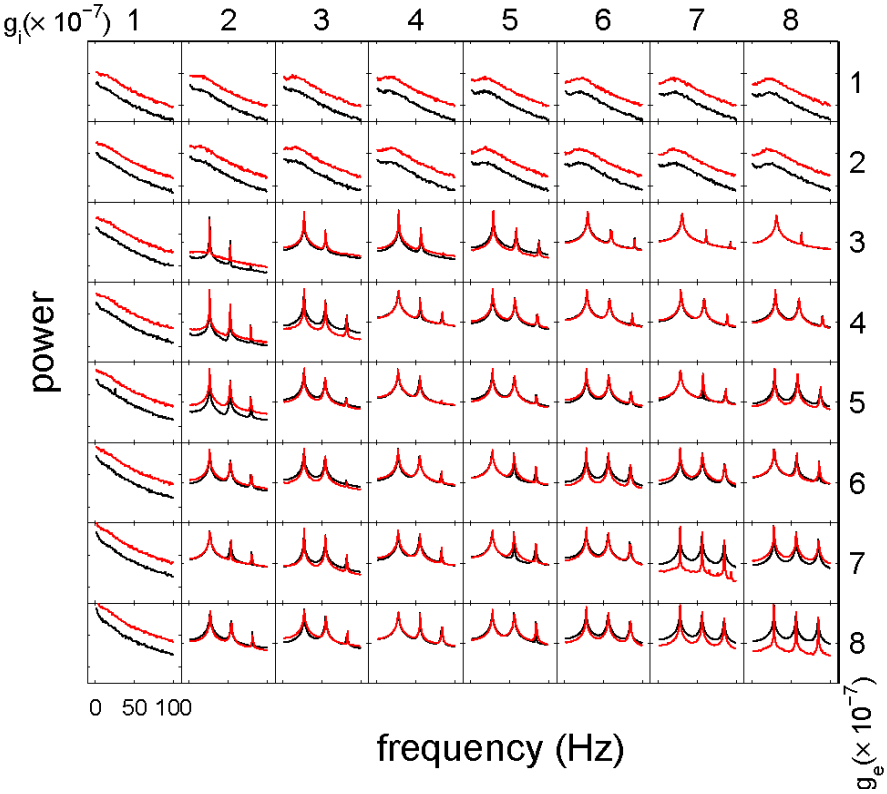

Figure 4-4 The effect of changing cortical architecture on LFP power spectrum.

This figure shows power spectra produced by LCM configured with different synaptic gains, and presynaptic neurons in layer IV decreased by 50%. The red lines and black lines illustrate the power spectra of activated and spontaneous LFPs.

Experimental models of neocortical epileptic foci suggest that reduced synaptic inhibition in layer IV plays an important role in epileptogenesis (Chatt and Ebersole, 1988; Jin et al., 2011). Focal cortical dysplasias characterized by an absence or significant reduction in layer IV are also very frequently associated with epilepsy (Blumcke et al., 2011). Figure 4-4 shows the LFP power spectrum shapes generated by the LCM when the numbers of synapses formed with presynaptic neurons in layer IV are decreased by 50%. Compared to Figure 4-3A, the power spectra show a small shift to small inhibitory gain. For example, for LFPs produced using excitatory and inhibitory synaptic gains of 2×10^{-7}

V/spike, the power spectrum changed from a frequency-inverse $1/f$ shape to one with spectral peaks as would be expected with seizures when presynaptic neurons of layer IV decrease by 50%. This suggests that, changes in neuron or synapse density may change the way LFPs oscillate dramatically. These alterations in dynamics may increase our understanding of how abnormalities in cortical architecture lead to seizures.

4.3.2 Spontaneous and visually stimulated local field potentials

Figure 4-5 shows the time courses of membrane potentials in a single run of the LCM. I found that in every cortical layer, membrane potentials oscillated with amplitudes of 0.05-0.2 mV; the amplitudes are much larger in layers IV and VI (around 0.1 mV) than in other layers (around 0.05 mV). During stimulation, the membrane potentials and its oscillation amplitudes increased in all layers except layer I. The power spectra in all layers, as provided in Figure 4-5, all showed inverse-square decreasing frequency background activities, which is observed experimentally (Buzsaki and Draguhn, 2004). Stimulation also increased high-frequency membrane potential oscillation of all deep layers.

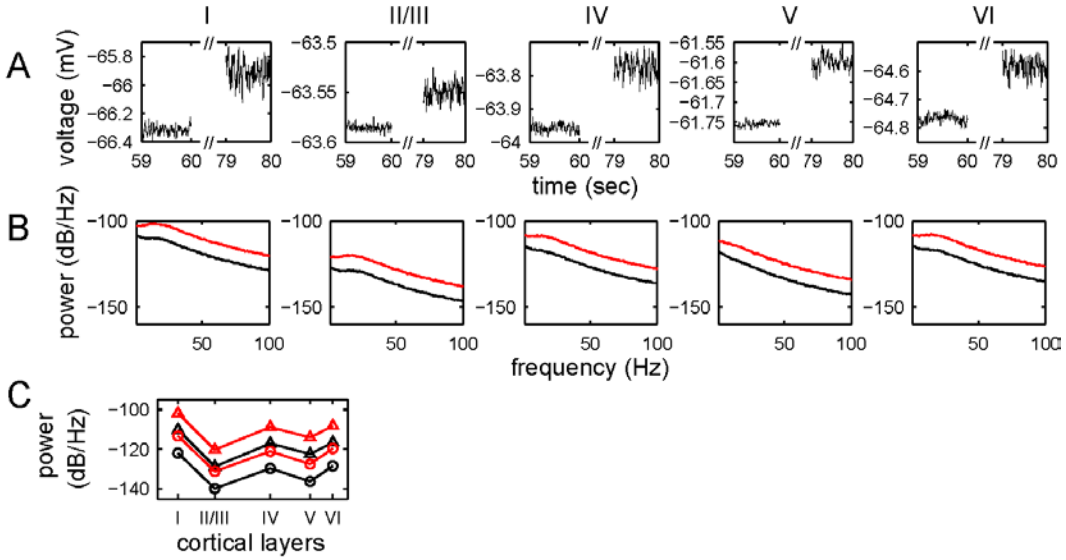

Figure 4-5 The temporal variations and power spectrum of membrane potentials in cortical layers.

Illustrated are (A) simulated field potentials of layer I, II/III, IV, V and VI, and (B) their corresponding power spectra for the general visual stimulation experiment, and (C) the average power spectra of LFPs in the gamma frequency (30-100 Hz, circles) and sub-gamma frequency (5-20 Hz, triangles) during spontaneous activity (black lines) and general stimulation (red lines). In (B) the black lines depict the resting state LFPs and red lines show the outcome of stimulation. The data are obtained using $g_e = g_i = 2 \times 10^{-7}$ V/spike.

The laminar distribution of the LFP power spectrum amplitude was examined. Figure 4-5C shows the laminar distribution of the average of the LFP power distribution in the

gamma frequency (30-100 Hz) and sub-gamma frequency (5-20 Hz) ranges for spontaneous activity and general stimulation. Higher frequency powers were observed in layers IV and VI. This is in agreement with experimentally measured laminar LFP amplitude profiles in the primary visual cortex (Maier et al., 2010). Since layers IV and VI are the main layers of the visual cortex receiving and sending projections to the LGN, the observed variation in LFP power spectra amplitudes between layers most likely results from these projections. I simulated the propagation of one spike source in the cortex using LCM. In Figure 4-6 I provide the result when a spike source is placed in the four central elements of layer IV for 20 msec after 60 seconds of spontaneous activity. Following spike onset, a strong potential is observed in the centre of all cortical layers except layer I. The potential is decreased in elements surrounding the source, simulating surround inhibition. I display the temporal profiles of current source density along a transverse line through the central point in layer IV and for the central elements of each cortical area in Figure 4-7.

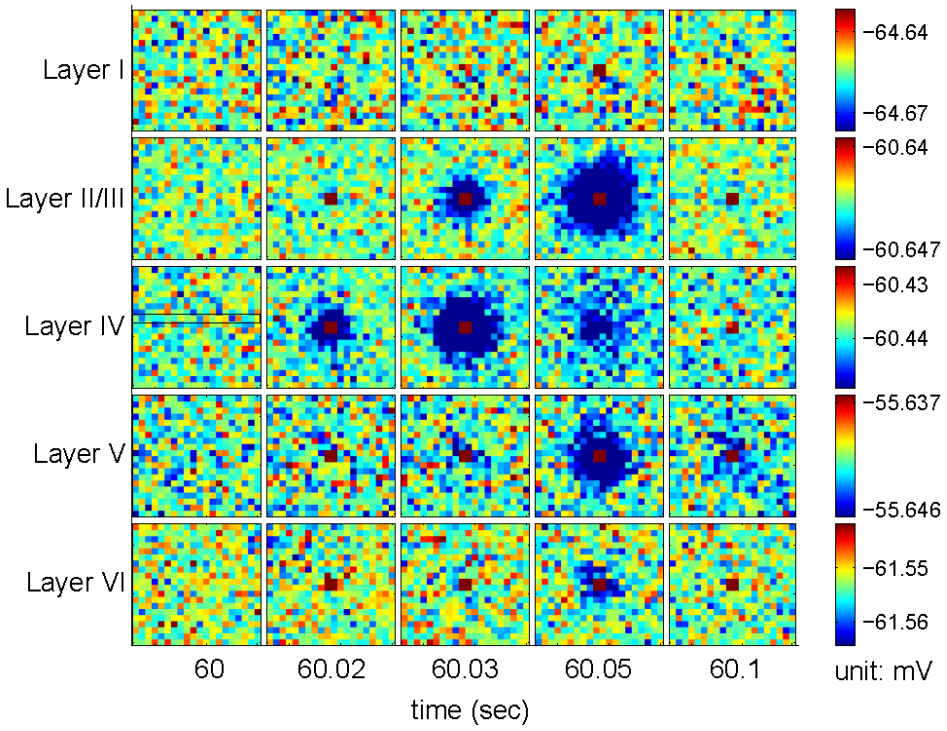

Figure 4-6 Potentials in the cortex driven by a single transient source.

The four central elements in layer IV are driven by 100 spike/sec LGN input starting after 60 seconds of spontaneous activity. The spike source lasts for 20 msec. The following parameters were used: $g_{\mathrm{e}} = 5 \times 10^{-7}$ V/spike , $g_{\mathrm{i}} = -1 \times 10^{-7}$ V/spike , $\phi_{\mathrm{LGN}} = 0.01$ spike/sec for spontaneous activity and $\phi_{\mathrm{LGN}} = 30$ spike/sec for a spike source in the central four elements of layer IV.

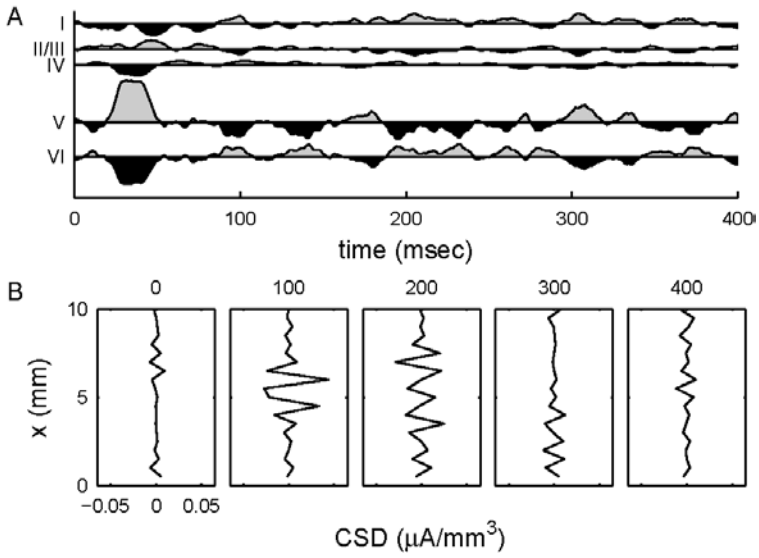

Figure 4-7 Current source densities (CSD) generated by the LCM.

Shown are (A) CSDs for the central elements of each cortical layer, and (B) temporal profile for current source density of the central line of layer IV (see Figure 4-6). The CSD plots show the difference between CSD at each time point and the mean value in the entire epoch. Time values are in milliseconds after the onset of transient LGN input. A positive CSD value indicates a current source. Results are calculated from the same dataset as Figure 4-6.

4.3.3 Steady-state visual evoked potentials (SSVEPs)

Many electrophysiological experiments have demonstrated that with intermittent light stimulation, neuronal activity in the visual cortex synchronises with stimulus frequency (Regan, 1989; Rager and Singer, 1998; Herrmann, 2001; Kim et al., 2007). Furthermore, EEG responses are enhanced at this frequency (fundamental harmonics), as well as at half the stimulus frequency (first sub-harmonic), and at multiples of the stimulus frequency (multiple harmonics). The responses to visual stimulation at specific frequencies, termed steady-state visual evoked potentials (SSVEPs), can be observed on both scalp EEG recordings (Herrmann, 2001) and invasive recordings of LFPs (Rager and Singer, 1998). I used SSVEPs to examine the effect of cortical architecture on LFPs.

The LCM was used to simulate LFPs with 10 Hz intermittent light stimulation represented by a Gaussian distribution of spike rates for neurons projecting from the LGN to the visual cortex. The peak and standard deviation of the Gaussian shape was 30 spikes/second and 6.25 msec, respectively (see Figure 4-2).

Figure 4-8 shows the variation of LFPs with time and the associated power spectra. Simulations using the LCM reproduced the power spectra reported in experimental data

(Herrmann, 2001). The LFP power spectrum had peaks at frequencies that were multiples of the stimulus frequency (i.e. capturing multiple harmonics). Notably, the amplitude of fundamental harmonic (i.e. frequency peak at 10 Hz) was smaller in layer II/III than other layers. This is probably because there are fewer projections from LGN to layer II/III than other layers. Experimentally observed sub-harmonics were not obvious in simulations using the LCM (Herrmann, 2001).

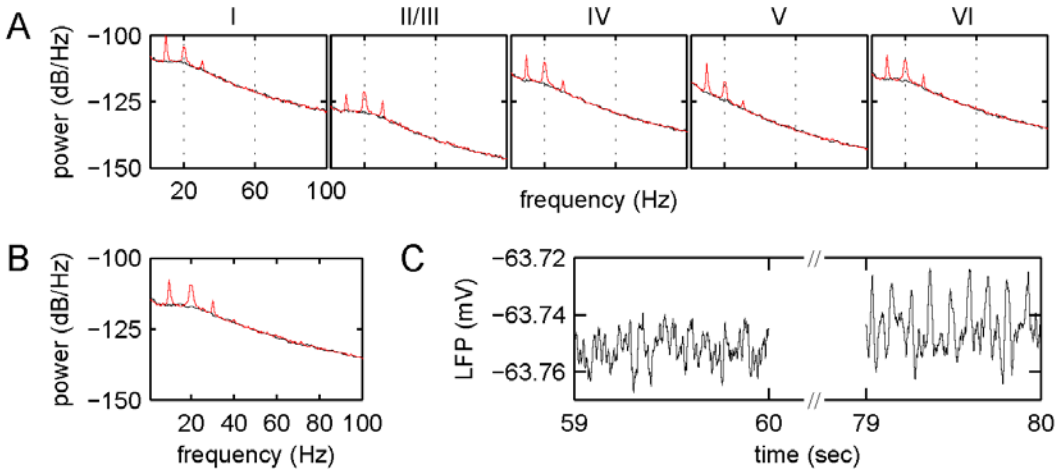

Figure 4-8 Power spectra of membrane potentials for SSVEPs generated with the LCM.

The figure shows (A) the power spectra of membrane potential in layers I, II/III, IV, V, VI and (B) power spectra of the LFP produced by the LCM under intermittent light stimulation. The black lines show power spectra of spontaneous LFPs, and red lines illustrate stimulated LFP power spectra. In (C) an example of LFPs before and after intermittent light stimulation in a single run is also shown. The following parameters were used: $g_e = g_i = 2 \times 10^{-7}$ V/spike , $\phi_{LGN} = 5$ spike/sec for spontaneous activity.

4.4 Discussion

This paper introduces the LCM and describes its use to simulate LFPs in the primary visual cortex. The LCM has the advantage that it incorporates the architecture of the visual cortex allowing the simulation of LFPs with high spatial and temporal resolution. I were able to simulate the membrane potential in each cortical layer, as well as its temporal variations. I used the LCM to investigate the relationship between visual stimulation and LFPs. I validated the model using two different experimental simulations: constant visual stimulation and intermittent light stimulation. The results were comparable to relevant experimental measurements. I also simulated the effects of changes in neuronal density in layer IV, often observed in epileptic cortical dysplastic tissue. For certain parameter combinations the changes in the power spectra were those expected in seizures. CSD

maps showed comparable features to experimental data and intra-laminar CSD profiles following transient LGN input had the appearance of surround inhibition.

With constant visual stimulation, the LCM produced LFPs oscillating in two different ways determined by the combination of parameters used in the simulation. When the cortex was activated with low levels of background noise and stimulus input (small synaptic gains), the LFP oscillation was governed by the pool of excitatory neurons. Synaptic transmission acts as a filter due to the convolution in the membrane potential aggregation function of LCM (refer to Equation S1.8 in Appendix A). Effectively, this dampens high frequency oscillations and results in an inverse-squared decreasing LFP spectrum. However, when the cortex is highly activated, inhibitory neurons play a more dominant role, resulting in oscillations in which initial activation of inhibitory neurons leads to suppression of the membrane potential of all neurons, including the inhibitory pool followed by a burst of activity cause by excitatory input.

The LFPs produced using low synaptic gains are comparable to experimentally observed LFPs in the normal brain, while the LFPs obtained with large synaptic gains are similar to those measured during seizures (Buzsaki and Draguhn, 2004). This suggests that changes in neuronal physiology can result in a change in the LFP power spectrum and may help to explain frequency changes in the EEG observed in certain neurological disorders. There are some differences between LFPs from the LCM and experimentally measured LFPs. The amplitude of low frequency (<10 Hz) LFPs produced by the model is lower than measured experimentally. A possible explanation is that the low frequency oscillation results from feedback loops between the visual cortex and other brain areas (Andersen and Andersson, 1968), which are not considered in the LCM. The gamma frequency (40-200 Hz) power of stimulated LFPs is also smaller than experimental measurements. I postulate that this is because extracellular potential changes caused by synaptic activities and spike conduction are not included in the calculation of LFPs. These are reported to have a greater influence on high frequency LFPs (Pettersen and Einevoll, 2008; Linden et al., 2010; Belluscio et al., 2012; Buzsaki et al., 2012). The LCM simplifies synaptic processes and spike propagation to a signal delivery level. It does not simulate the burst of synaptic transmission and spikes.

The CSDs calculated from LCM recreates several features from experimental observations (Schroeder et al., 1998). Within layers, the CSD profile simulated surround

inhibition (Sengpiel et al., 1997). Across cortical layers, the temporal profile of CSDs was similar to those observed by Schroeder et al. (Schroeder et al., 1998) with transition from sink to source following stimulation.

I used SSVEPs, to test the effects of incorporating cortical architecture on simulation output. In the intermittent light stimulation study, I used the LCM to reproduce the behaviour of SSVEPs. The fundamental and high order harmonics were apparent in the visual cortex. The first sub-harmonics, shown to be present empirically (Herrmann, 2001), may be brought about by feedback loops between the primary visual cortex and other visual cortical areas. These connections are not included in the LCM.

Although I showed that LCM is able to reproduce some of the results of electrophysiological experiments, it has some limitations. Firstly, only two populations of neurons (excitatory and inhibitory) are considered. The behaviour of excitatory neurons may not be best captured by a single category. For example, fast-spiking neurons generate spikes differently from other excitatory neurons (Thomson et al., 1996). In future work I will extend the LCM to include multiple categories of excitatory neurons. Secondly, simulation of neurotransmission in the LCM may be oversimplified. For example, in its current form it cannot simulate the effects of activating fast (AMPA) and slow (NMDA) excitatory glutamatergic receptors on LFPs. Thirdly, the physiological parameters used in the simulation were obtained from the results of experiments conducted in different species. In the simulations, LFPs were calculated as the aggregate membrane potential dynamics of populations of neurons, an approach commonly employed in simulation studies e.g. (Martinez and Montejo, 2008). This approach may be inaccurate because it does not take into account the filtering properties of the neural membrane (Pettersen and Einevoll, 2008; Linden et al., 2010). Methods based, for example, upon summation of conductance of synapses to pyramidal neurons (Nunez and Srinivasan, 2006; Einevoll et al., 2007; Pettersen and Einevoll, 2008) are inapplicable to the LCM, which simulates the collective activity of neuron groups. A future hybrid model is required to link continuum cortical models and models based on simulating the properties of individual neurons.

Chapter 5

MRI signal phase oscillates with neuronal activity in cerebral cortex: implications for neuronal current imaging

5.1 Introduction

While the feasibility of nc-MRI is still debated, computer simulations are an important paradigm for predicting the nc-MRI techniques that are most likely to succeed. However, a major challenge for simulating the nc-MRI signal is to accurately model the spatial distribution and temporal variation of neuronal currents. Previous attempts have computed neuronal currents using an ensemble of identical neurons, for example an anatomically realistic pyramidal neuron from rat cortex (Blagoev et al., 2007), monkey hippocampus (Cassara et al., 2008), or human cortex (Luo et al., 2011b). This approach reduces the computational complexity inherent in simulating the dynamics of a large number of individual neurons. However, the MRI signal predicted by such models may be inaccurate for two reasons. First, morphological variations between neurons, which may have a significant impact on the size of calculated neuronal magnetic fields (NMF) (Cassara et al., 2008), are ignored. Second, models in which all neurons have identical firing patterns are likely to lead to unrealistic predicted time courses of neuronal current.

In the present work, I predicted the nc-MRI signal using the laminar cortex model (Du et al., 2012a, b), a three-dimensional cortical network model incorporating realistic cortical architecture. I also simulated temporal variations in neuronal activity associated with realistic cortical architecture and neuronal morphology. The model was used to study the neuronal currents and predicted nc-MRI signal associated with different neuronal oscillatory states, at different levels of neuronal activity in the primary visual cortex of cats. The ability of current MRI techniques to detect predicted changes in MR signal magnitude and phase was also assessed.

5.2 Material and methods

5.2.1 Neuronal activity simulation

I used the LCM to simulate neuronal activity of a grid of cortical columns. For neuronal current simulation, the LCM has been changed to include more cortical architecture features. In the cortex, neurons may form synapses in multiple layers and the spatial distribution of synapses is essential for NMF calculation. Whereas the LCM described in Chapter 4 does not consider the laminar distribution of synapses and direct synaptic connections between neuron groups were assumed, the model was modified to incorporate features of cortical architecture. For example, a neuron group can be connected to another neuron group via synapses in several layers. An example is given in Table S5 in Appendix C (Data were adopted from (Izhikevich and Edelman, 2008)). I also added a new spiny stellate (SS4) neuron group in layer IV, as these neurons have a different morphology and synaptic connection pattern to the pyramidal neurons of layer IV. The neuron groups of the new LCM are listed in Table 5-1.

Index	Neuron		Neurons under 1 mm^2 area	NMF calculated?
0	E1	Excitatory neuron in layer I	36	
1	I1	Inhibitory neuron in layer I	1177	
2	P2/3	Pyramidal neuron in layer II/III	20394	Yes
3	I2/3	Inhibitory neuron in layer II/III	5726	
4	P4	Pyramidal neuron in layer IV	7216	Yes
5	SS4	Spiny stellate neuron in layer IV	14433	Yes
6	I4	Inhibitory neuron in layer IV	5412	
7	P5	Pyramidal neuron in layer V	4785	Yes
8	I5	Inhibitory neuron in layer V	1098	
9	P6	Pyramidal neuron in layer VI	14198	Yes
10	I6	Inhibitory neuron in layer VI	3138	

Table 5-1 Neuron groups simulated in LCM.

The neuron numbers were derived from (Beaulieu and Colonnier, 1983).

The LCM was used to simulate a cortical area of 1.12×1.12 mm^2, which is discretised to a 20×20 grid. The grid elements are of a size similar to mini-columns (about 56 μm) (Peters and Yilmaz, 1993). Simulation of a 60 second time course was performed starting at time *t*=0 seconds. After initialization, time evolution without particular stimulation for 50 seconds was simulated to allow the system to reach a steady state. Constant stimulation was commenced at time t=50 seconds (see Du et al., 2012a for details). The neuron

membrane potentials of the last second were recorded and used for subsequent NMF calculations.

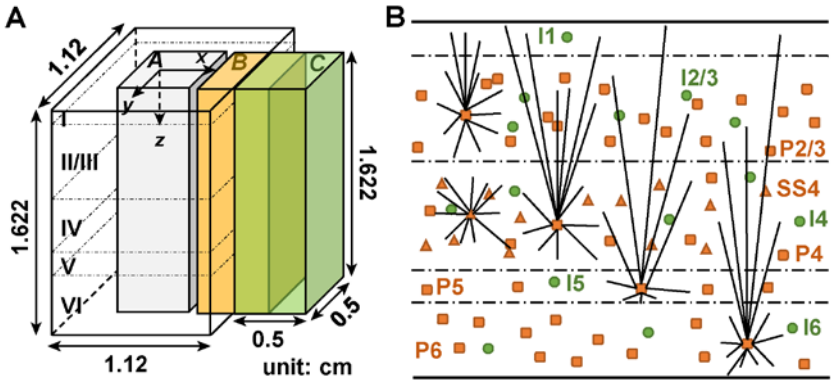

Figure 5-1 Structure of the model.

The figure shows (A) the geometry of LCM simulated cortical region (transparent box) and three equal-size voxels (filled boxes), and (B) a sketch of cortical neurons and examples of dendrite tree structures.

Spontaneous activity was simulated using the following parameter values: excitatory synaptic gain $g_{\mathrm{e}} = 0.9 \times 10^{-6}$ V/spike, inhibitory synaptic gain $g_{\mathrm{i}} = 1.98 \times 10^{-6}$ V/spike. Visual stimulation was simulated as white noise with mean=0 and deviation = 30 spike/sec (see Du et al., 2012a for details). Stimulated activity was produced using the following parameter values: $g_{\mathrm{e}} = 3.0 \times 10^{-6}$ V/spike, $g_{\mathrm{i}} = 5.2 \times 10^{-6}$ V/spike. The same visual stimulation was used. While multiple combinations of parameter values can result in similar neuronal activity, the parameter values provided above were empirically chosen to generate spontaneous and stimulated neuronal activity having different oscillation states (for details, see Du et al., 2012a).

5.2.2 Axon and dendrite geometries

Neuronal membrane potentials generated by the LCM were used as the input for the NMF model. For each neuron, the number of APs at time *t* was given by:

$$N_q^{\mathrm{AP}}(t) = Q_q(V_q) \cdot \Delta t \tag{5.1}$$

where $Q_q(x)$ is the spike generation function (see Du et al., 2012a for details), V_q is the neuron membrane potential of the group of neurons, and Δt is the time step, which was set to 1 msec. Each neuron was able to receive synaptic input from multiple presynaptic neuron groups. The number of PSPs was given by:

$$N_q^{\mathrm{PSP}}(t) = N_{qp}^{\mathrm{synp}} \varphi_p(t) \cdot \Delta t \tag{5.2}$$

where $\varphi_p(t)$ is the efferent spike rate at the synapse determined by the firing state of the presynaptic neuron group, and N_{qp}^{synp} is the number of synapses from presynaptic neurons. I also assigned a small random time delay ($< \Delta t$) to each AP and PSP to avoid unrealistic synchronisations between APs and PSPs.

The geometries of the axons and dendrites were generated dynamically. Axons and dendrites were modelled as straight cables between synapses and neuron bodies. Neuron bodies and synapses were evenly distributed within each cortical layer and each neuron was able to synapse with neurons in multiple cortical layers. The target synapse of an AP was randomly selected from all possible synapses for that neuron. For each neuron, I assumed that the target synapses for its APs within a given cortical layer were distributed according to a two-dimensional normal distribution (the standard deviation is set to 40 μm for I1, I2/3, SS4, I4, I5, I6 neurons, and 80 μm for E1, P2/3, P4, P5, P6 neurons) and that its afferent synapses were evenly distributed within a cylinder (the radius is set to 100 μm for all neurons) (see Figure 5-1B). The statistics of the APs and PSPs generated in the model are provided in Figure S3 in Appendix C.

To enable tractable simulations, I used a single membrane potential shape for all APs and for all PSPs separately (see Figure 5-2), and their amplitudes were drawn from a Gaussian distribution (mean = 21 mV, standard deviation = 2.1 mV for APs, and mean = 1.2 mV, standard deviation = 0.12 mV for PSPs). I also assumed an exponential decay for PSPs with conduction along a cable (Johnston and Wu, 1995):

$$V^{\mathrm{PSP}}(t,s) = \exp\left(-\frac{|s - s_0|}{\lambda^{\mathrm{PSP}}}\right) V^{\mathrm{PSP}}\left(t - \frac{s - s_0}{v^{\mathrm{PSP}}}, s_0\right) \tag{5.3}$$

where $V^{\mathrm{PSP}}(t,s)$ is the membrane potential at position s at time t, s_0 is the synapse location on the dendrite, $v^{\mathrm{PSP}} = 0.1$ m/sec is the velocity of PSPs, and $\lambda^{\mathrm{PSP}} = 333$ μm is the decay factor (Johnston and Wu, 1995). The conduction velocity of APs is $v^{\mathrm{AP}} = 1.0$ m/sec and they were assumed not to change shape during propagation.

5.2.3 Magnetic field of APs and PSPs

Both APs and PSPs were modelled separately as membrane potential changes of biological cables. I calculated their magnetic fields using the method of Woosley et al. (Woosley et al., 1985). The magnetic field at a radial distance ρ from the cable was expressed as:

$$B(\rho,z) = G(\rho,z) \otimes J_z^-(z) = G(\rho,z) \otimes \left[J_z^{\mathrm{i}}(z) - J_z^{\mathrm{e}}(z) \right] \tag{5.4}$$

where $\otimes$ indicates convolution on z, a is cable radius (see Figure 5-2), which was set to 0.5 μm for dendrites and 0.4 μm for axons, and J_z^{i} and J_z^{e} are the interior and exterior axial currents close to the cable membrane. In the Fourier domain, they are (Woosley et al., 1985):

$$\tilde{J}_z^{\mathrm{i}}(k) = -i \frac{\sigma^{\mathrm{i}} \gamma(k) k}{\gamma(k)+1} \tilde{V}(k), \tag{5.5}$$

$$\tilde{J}_{\mathrm{z}}^{\mathrm{e}}(k) = i \frac{\sigma^{\mathrm{e}} k}{\gamma(k)+1} \tilde{V}(k), \tag{5.6}$$

where k is the spatial frequency corresponding to the longitudinal coordinate z, $\tilde{V}(k)$ is the Fourier transform of the membrane potential $V(z)$, and $\gamma(k)$ are:

$$\gamma(|k|a) = \frac{\sigma^{\mathrm{e}} K_1(|k|a) I_0(|k|a)}{\sigma^{\mathrm{i}} K_0(|k|a) I_1(|k|a)} .$$

where $I_0(x)$ and $I_1(x)$ are Bessel functions of the first kind and of first and second order, $K_0(x)$ and $K_1(x)$ are Bessel functions of the second kind and of first and second order, and $\sigma^{\mathrm{i}} = 1.0$ S/m and $\sigma^{\mathrm{e}} = 0.154$ S/m are interior and exterior media conductivities. The tilde denotes the Fourier domain. The Green's function $G(\rho,z)$, was formulated in terms of elliptic integrals:

$$G(\rho,z) = \frac{\mu a}{\pi B \sqrt{A+B}} \left[A\mathbf{K}(m) - (A+B)\mathbf{E}(m) \right], \tag{5.7}$$

where $\mu = 1.2566 \times 10^{-6}$ H/m is the permeability, $A = \rho^2 + a^2 + z^2$, $B = 2a\rho$, and $\mathbf{K}(\mathrm{m})$ and $\mathbf{E}(\mathrm{m})$ is the complete elliptic integrals of the first and second kind, respectively, and $m = 2B/(A+B)$ is the square of the elliptic modulus. A plot of the Green's function is provided in Figure 5-2.

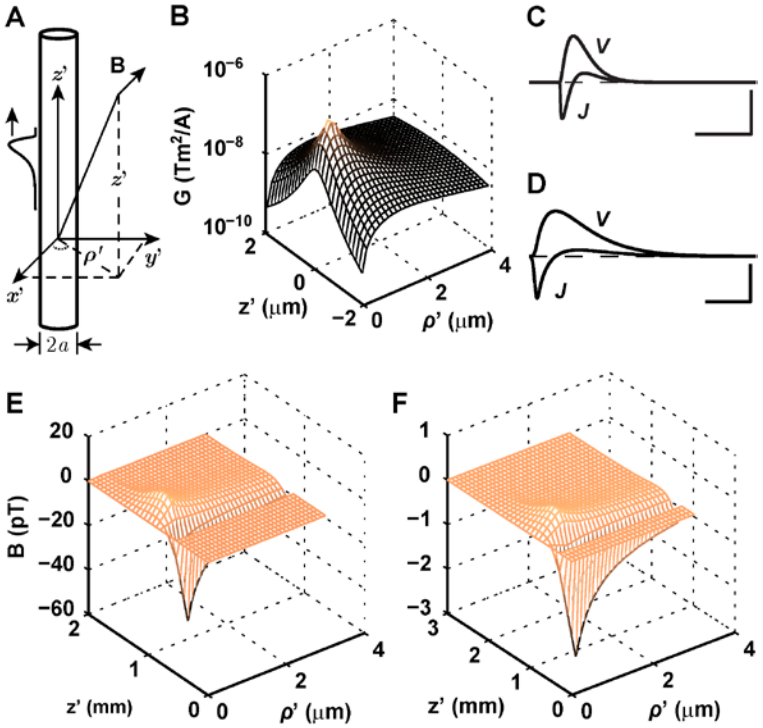

Figure 5-2 Magnetic fields of a single AP and a single PSP.

Shown are (A) the coordinate system for AP and PSP magnetic field calculation, (B) a plot of the Green's function G (see Equation (5.7)), the shape (upper line) and surface currents (lower line) of (C) the AP (scale bar: 0.5 mm, 20 mV, 200A/m^2) and (D) the PSP (scale bar: 0.5 mm, 1.0 mV, 10A/m^2) used in the simulation, and the magnetic fields of the (E) AP and (F) the PSP. In (B), the Green's function G goes to zero when ρ = 0. See also Figure S3 in Appendix C for statistical information of the APs and PSPs for an animation of PSP magnetic fields.

5.2.4 Neuronal current MRI signal

The frequency of precession of protons is determined by the magnetic field present, which is a function of the scanner field (B_0) and the NMF. The NMF-induced phase changes accumulated during t_P (Heller et al., 2009):

$$\varphi(\mathbf{r},t_0) = \gamma \int_{t_0}^{t_0+t_P} B_n^{NMF}(\mathbf{r},\tau)\, \mathrm{d}\tau\,, \tag{5.8}$$

where $\gamma = 2.675 \times 10^8\ \mathrm{rad/(T \cdot sec)}$ is the proton gyromagnetic ratio, $B_n^{\mathrm{NMF}}(\mathbf{r},t)$ is the component of NMF aligned with B_0, t_p is the phase accumulating time (PAT), which is equivalent to the echo time (TE) in gradient echo (GE) sequences, or the time to data acquisition (TA) in free induction decay (FID), and t_0 is the application time of radiofrequency (RF) pulse. If the proton density within a voxel is assumed to be

homogeneously distributed, the MRI signal modified by neuronal currents is (Heller et al., 2009):

$$S = S_0 \frac{1}{V} \int_V \mathrm{d}^3 r \exp\left[-\mathrm{i}\,\varphi(\mathbf{r},t)\right], \tag{5.9}$$

where S_0 is the complex MRI signal without neuronal currents and V is voxel volume. The magnitude and phase change are:

$$\begin{aligned} \Delta s &= \frac{\left|S\right| - \left|S_0\right|}{\left|S_0\right|} = \frac{1}{V}\left|\int_V \mathrm{d}^3 r \exp\left[-\mathrm{i}\,\varphi(\mathbf{r},t)\right]\right| - 1 \\ \Delta\varphi &= \arg\left\{\int_V \mathrm{d}^3 r \exp\left[-\mathrm{i}\,\varphi(\mathbf{r},t)\right]\right\} \end{aligned} \tag{5.10}$$

where Δs and $\Delta\phi$ are the fractional magnitude change and phase change of the nc-MRI signal. Since the magnitude of NMFs was much smaller than the magnitude of B_0, the small angle approximation for $\exp(-\mathrm{i}\,\phi)$ was applied:

$$\Delta s = \frac{1}{2}\left(\left\langle \varphi^2 \right\rangle - \left\langle \varphi \right\rangle^2\right) + \mathcal{O}(\varphi^4), \tag{5.11}$$

$$\Delta\varphi = -\left\langle \varphi \right\rangle + \mathcal{O}(\varphi^3), \tag{5.12}$$

where $\left\langle \phi \right\rangle$ and $\left\langle \phi^2 \right\rangle$ denote the mean value of ϕ and ϕ^2 evaluated over the volume.

5.2.5 Simulation

The simulation program was written in the C++ programming language and compiled with the Intel® C++ Compiler version 2013.3.163 (x86_64, http://software.intel.com/intel-compilers/) on an SGI® Altix® XE Cluster running SUSE Linux version 11 SP2 (x86_64, http://www.suse.com). The SGI® Message Passing Toolkit (http://www.sgi.com), a message passing interface implementation was used to parallelize the code to speed up program execution. The program was configured to run on 320 processors, and a run took around 48 hours to complete. The authors are willing to provide the source code upon request.

5.3 Results

I first examined the MRI signal induced by a single postsynaptic potential (PSP). I simulated a PSP propagating on a dendrite (see Figure 5-3). The magnetic fields of the PSP in two cubic volumes of interest (VOIs) were calculated. VOI 1 is symmetric about the dendrite, whilst VOI 2 is positioned alongside the dendrite. MRI signal magnitude and phase changes were calculated using different phase accumulating time (PAT). As shown in Figure 5-3, three interesting features of the signals in each VOI can be noted. First, the signal magnitude and phase changes in both VOIs tend to zero when phase accumulating time exceeds 20 msec. Second, the phase change computed for VOI 1 but not VOI 2 is essentially zero. Third, the magnitude change for VOI 1 is at least three orders of magnitude larger than for VOI 2.

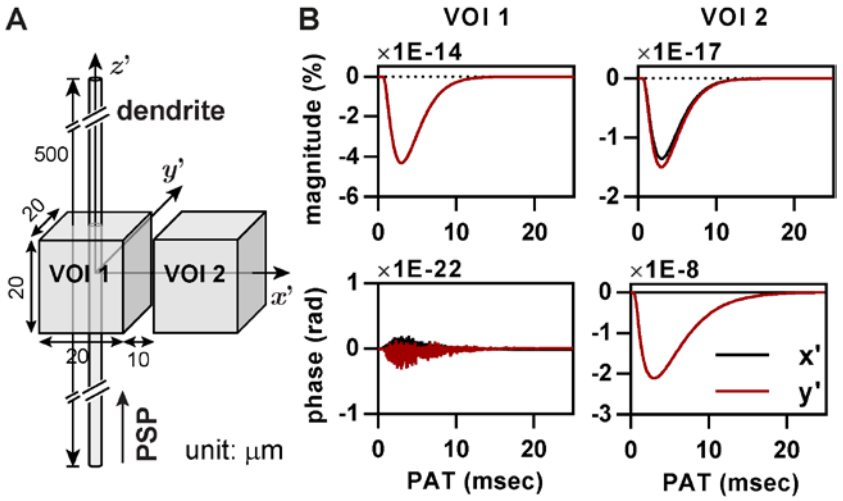

Figure 5-3 The MR signal changes induced by a single PSP.

Shown are (A) a PSP on a straight dendrite and the two small volume-of-interest (named VOI 1 and VOI 2) in which the MR signal changes were calculated, and (B) the plot of the phase and magnitude changes of the two VOIs as a function of phase accumulating time (PAT). The PAT starts at the same time as the PSP. The black and red lines in (B) show the signals produced by x'- and y'-component of NMFs, i.e. the signals predicted for the imaging fields B_0 are aligned with x-, and y-axes, respectively. Notice the order differences of the signal changes.

To assess the influence of neuronal oscillation state on nc-MRI signals, two different oscillation states were generated using the LCM. Spontaneous activity corresponds to the activity in the primary visual cortex under natural visual stimulation and stimulated activity corresponds to activity induced by intermittent photic stimulation at a fixed frequency of 25 Hz. Average neuronal firing rates in the two states are plotted in Figure 5-4. Spontaneous

activity was characterized by a frequency spectrum of average firing rates dominated by low frequencies, while stimulated activity displayed an amplified oscillation around 25 Hz. The two states of neuronal activity were then used as inputs into the NMF model, and their effects on MRI signal phase and magnitude were calculated.

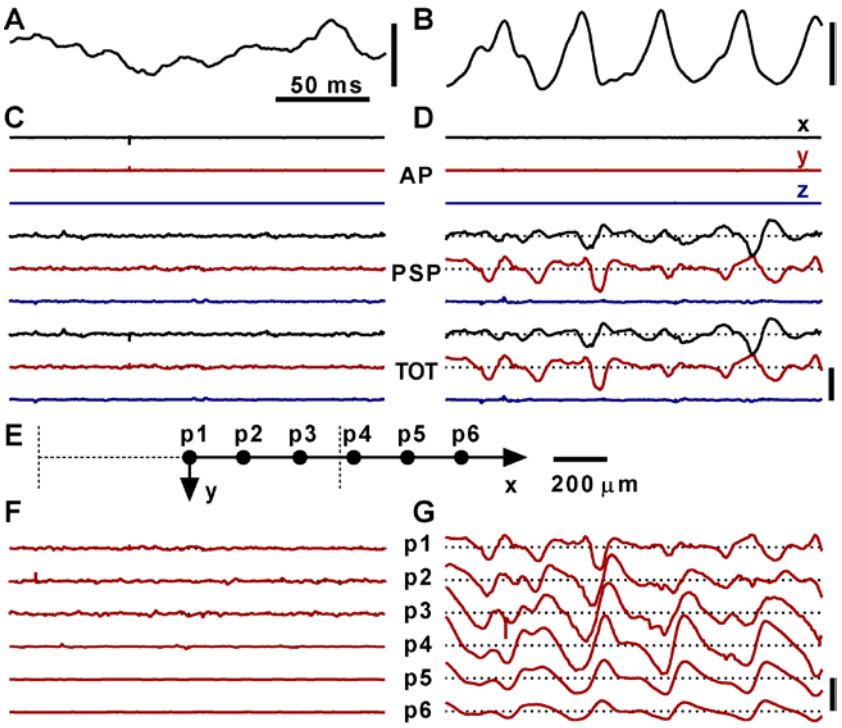

Figure 5-4 NMF time variations.

Shown are the average neuronal firing rates of (A) spontaneous activity (scale bar: 0.001 spikes/sec) and (B) stimulated activity (scale bar: 20 spikes/sec), the AP, PSP and total NMFs at the centre of voxel A during (C) the spontaneous activity and (D) stimulated activity (scale bar: 500 pT), and (E) the locations of six field points in the middle layer of the cortex and their NMFs during (F) spontaneous activity and (G) stimulated activity (scale bar: 500 pT). The dotted baselines in (C-D) and (F-G) indicate zero magnetic field level. The black, red and blue lines in (C-D) depict the x-, y- and z-components of NMFs, respectively. The vertical dashed lines in (E) indicate the boundaries of the active region. In (F-G), only the y-components of the total NMFs are shown, see Figure S4 in Appendix C for x- and y-components.

For numerical efficiency, I decomposed neuronal activities into action potentials (AP) and PSPs. The magnetic fields of APs and PSPs were calculated separately. Due to their different temporal scales, a time increment of 1 msec was used to simulate PSPs, and 0.1 msec was used for APs. PSP magnetic fields were then linearly interpolated to correspond with the time points set for APs. Total NMFs were obtained by summing AP and PSP magnetic fields, (see Figure 5-4 and Figure 5-5 for examples). As expected, the pattern of magnetic fields for APs differed significantly from that of PSPs. APs produce numerous sharp magnetic field peaks (small magnetic fields are not visible in Figure 5-4 due to

scaling), while PSPs produced smooth, comparatively slowly evolving magnetic fields. This difference can be explained by noting that a PSP lasts at least ten times longer than an AP. Stimulated activity produced NMFs about four times larger than spontaneous activity. Although neuronal firing rate was higher for stimulated activity, this is unlikely to be responsible for the difference in NMFs. I noticed that large NMFs also arise with low firing rates during stimulated activity (see Figure 5-4 and Figure S4 in Appendix C). This finding suggests that large NMFs are caused by oscillations in neuronal activity. Furthermore, NMFs during simulated spontaneous activity decayed rapidly outside the active region, to the extent that they dropped to almost zero at about 250 μm away from the region. NMFs with stimulated activity were larger outside than within the active region. Indeed, the largest NMFs with stimulated activity occurred just outside the active region (see Figure 5-4, Figure 5-5 and Figure S4 in Appendix C) and the NMFs decayed by about 50% at a distance of 500 μm. This finding suggests that collective flows of neuronal currents are produced during stimulated activity.

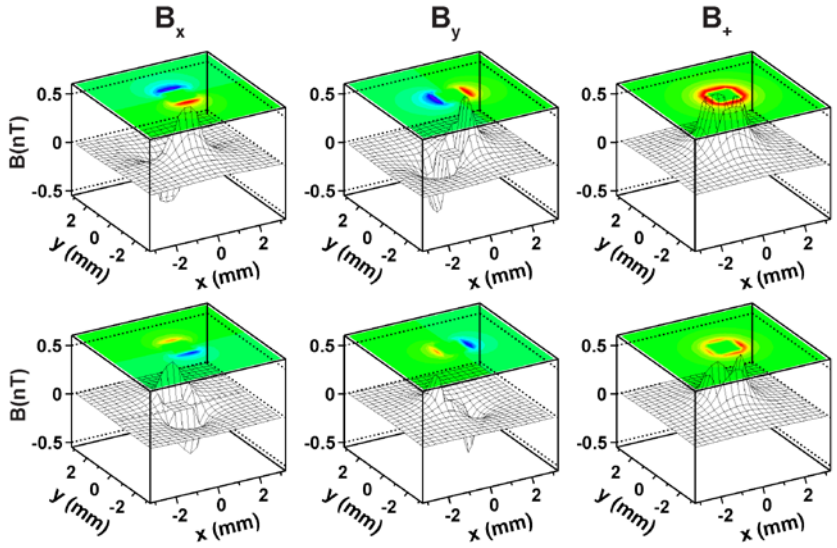

Figure 5-5 The spatial distributions of magnetic field components outside the activated cortical region.

For the case of stimulated neuronal activity, illustrated are the spatial distributions of magnetic field components (B_x, B_x, and $B_+ = \sqrt{B_x^2 + B_y^2}$) in the middle layer of the cortex at two different time points. Only magnetic fields outside the activated cortical region are shown.

To validate the method for calculating the NMF, I simulated magnetoencephalography (MEG) signals induced by a short visual stimulus, and compared them with experimental measurements. I simulated MEG signals generated by a one centimetre square cortical

region (see Figure 5-6). The cortical region was divided into a 9×9 grid, and used the LCM to simulate the neuronal activity of each element. Since the firing rates of neurons in a large cortical region have been difficult to measure, the generated neuronal responses to stimulation were computed by multiplying the spontaneous activity neuronal membrane potentials by:

$$f(x) = \begin{cases} A\lambda^n (t - t_0)^{n-1} \exp\left[-\lambda(t - t_0)\right] + 0.4 & t_0 < t < t_0 + \tau \\ 0.4 & \text{otherwise} \end{cases} \tag{5.13}$$

where τ is the duration of the stimulus, $n = 3.2$, $\lambda = 52$, and A was set to 0.01, 0.02, 0.03, 0.04 for four stimulation intensities. The use of the Gamma function accounts for the rapid increase of firing rates at the onset of stimuli and the slow decrease at the end of the stimuli, and these parameter values were chosen empirically to generate the average neuronal firing rates as shown in Figure 5-6B. The MEG signal was obtained by summing the magnetic fields of all elements and displayed two magnetic field peaks with opposite polarity, similar to the MEG signals observed in auditory cortex during brief exposure to an audible tone (Nakamura et al., 1997). The signal magnitude is of the same order of magnitude as the experimentally observed signal (Brenner et al., 1975). The linear relationship between the simulated intensity of neuronal activity and MEG signal magnitude was also comparable to the relationship between stimulation strength and measured MEG signal magnitude (Nakamura et al., 1997).

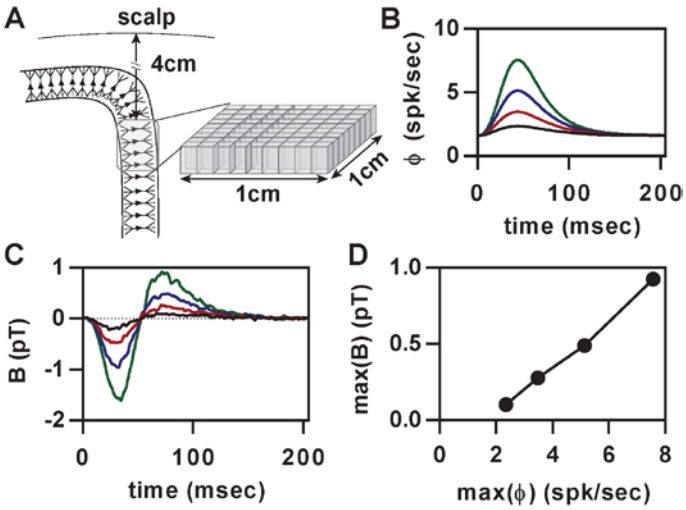

Figure 5-6 Simulated MEG signals.

Shown are (A) the structure of the MEG model, (B) average neuronal firing rates used in simulation and (C) the corresponding simulated MEG signals, and (D) the relationship between neuronal firing rate intensity and MEG signal magnitudes.

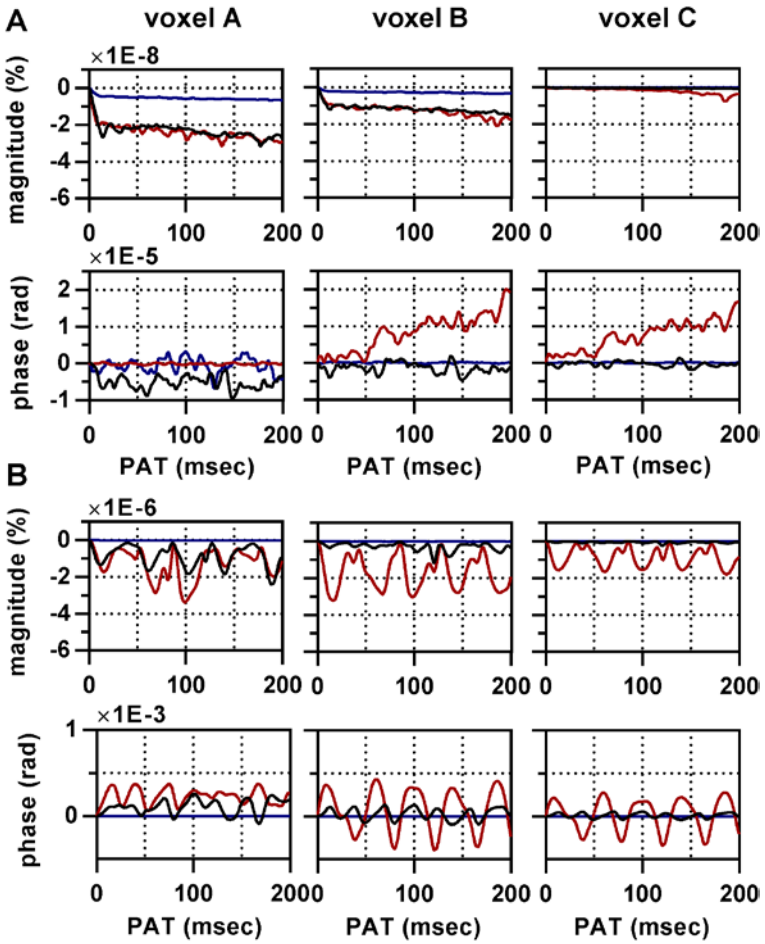

Figure 5-7 The MR signal magnitude and phase changes induced by spontaneous activity (A) and stimulated activity (B).

The signal changes are plotted against phase accumulating times. The black, red and blue lines show the signals produced by the x-, y- and z-components of NMFs, i.e. the signals predicted for the imaging fields B_0 are aligned with x-, y-, and z-axes, respectively. Results were calculated from the same dataset as Figure 5-4. See also Figure 5-8.

To assess the spatial variation of nc-MRI signals, I calculated the neuronal current induced MRI signal magnitude and phase changes in three voxels: voxel A is located in the centre of the activated cortical region, voxel B is located on the boundary of the region (half the voxel is within the activated region and half is outside), and voxel C is located just outside the region (see Figure 5-1). In each of the voxels, neuronal magnetic fields were calculated at 3200 equally-spaced points and then used to evaluate nc-MRI signals. The results are shown in Figure 5-7 and Figure 5-8 (also see Figure S5 in Appendix C). In general, I observed very small variations in signal magnitude, about 2-5 parts-per-billion (ppb) for spontaneous activity and 20-40 ppb for stimulated activity (phase accumulation time = 200 msec). A signal magnitude change of this size is well below the limit of

detectability of current MRI techniques. However, larger relative changes in signal phase were observed, up to 15 µrad for spontaneous activity and 820 µrad for stimulated activity (phase accumulation time = 200 msec). Changes of this order of magnitude should be detectable using current MRI techniques. Moreover, changes in phase are larger at the boundary of the activated region. Phase changes in voxel B were larger than for voxels A and C for both spontaneous and stimulated activity.

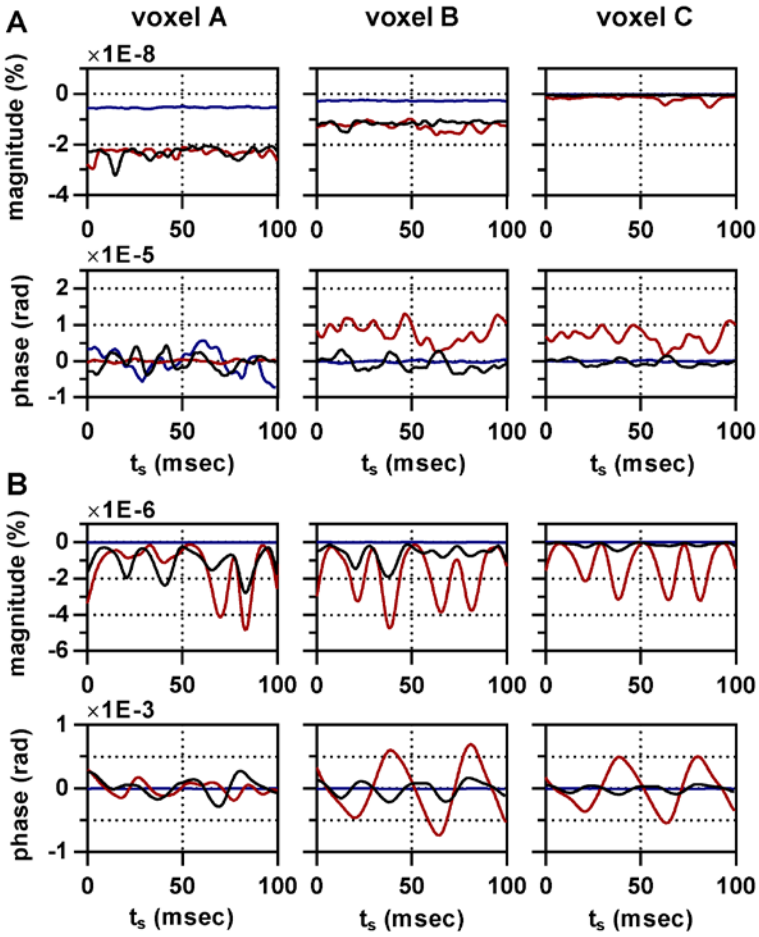

Figure 5-8 The dependence of nc-MRI signals on the starting point of phase accumulating time for spontaneous activity (A) and stimulated activity (B).

Shown are the nc-MRI signals calculated using phase accumulating times (PAT) starting at different times (ts). The PAT was set to 100 msec. The black, red and blue lines show the signals produced by the x-, y- and z-components of NMFs, respectively. Results were calculated from the same dataset as Figure 5-4. The results shown in Figure 5-7 were calculated with t_s = 0 msec.

The temporal evolution of the nc-MRI signal differed between spontaneous and stimulated activity. For spontaneous activity, signal phase in voxel A fluctuated about zero and signal magnitude increased over time suggesting that the magnetic fields within an active region are spatially inhomogeneous. In voxels B and C, changes in both signal

phase and magnitude accumulated over time, suggesting that a homogeneous magnetic field component was the predominant influence. With stimulated activity, signal magnitude and phase evolution displayed recurring peaks at a frequency corresponding to neuronal firing rates (see Figure 5-4). A relationship between firing rates and simulated signals was evident from the results (see Figure 5-4, Figure 5-7 and Figure 5-8).

Due to the computational resources required by the simulations, I was not able to simulate directly the nc-MRI signal of large cortical regions and larger voxels. From the results shown above, however, I could estimate the MRI signal phase changes produced by a cortical region consisting of a number of sub-regions. I constructed an extended cortex region consisting of a matrix of 10x10 sub-regions (see Figure 5-9A), each sub-region having the dimension and neuronal activity pattern as the cortical setup from above. I calculated the magnetic field components produced by each cortical region at sampling points inside and outside the extended region (see Figure 5-9A). To allow the magnetic fields produced by individual cortical sub-regions to be estimated, it was assumed that the neuronal currents produced by the cortical sub-region are aligned with z-axis, and a far field approximation of Biot-Savart's Law was adopted, assuming that their magnetic field decayed according to $1/r^2$ when away from the source. Then the magnetic field produced by a cortical sub-region at an arbitrary location P outside the region can be expressed in terms of a known magnetic field of a reference point B as:

$$\begin{aligned} B_{\mathrm{P}x} &= \frac{r_{\mathrm{B}}^2}{r_{\mathrm{P}}^2}\left(B_{\mathrm{B}x}\cos\theta - B_{\mathrm{B}y}\sin\theta\right) \\ B_{\mathrm{P}y} &= \frac{r_{\mathrm{B}}^2}{r_{\mathrm{P}}^2}\left(B_{\mathrm{B}x}\sin\theta + B_{\mathrm{B}y}\cos\theta\right) \end{aligned} \tag{5.14}$$

where r_{B} and r_{P} are the distance of the centre of the cortical sub-region to position P and B, respectively, and $(B_{\mathrm{B}x}, B_{\mathrm{B}y})$ is the magnetic field at point B. I used the centre of voxel B as the reference point, and assumed its magnetic fields is equal to the mean magnetic field of the voxel. When their magnetic fields inside the cortical sub-region cannot be estimated in a straightforward manner, because the far field approximation does not hold. I avoided this problem by placing the point in the centre of the sub-region and use the already calculated mean magnetic field of voxel A. The magnetic fields of five example sampling points highlighted in Figure 5-9A are provided in Table 5-2. The cortical region comprising 100 sub-regions resulted in larger magnetic fields than a single cortical sub-

region. At the boundary of the domain (the centre of voxel B and voxel II), for example, magnetic fields due to the extended cortical region were found to be 69.1% larger than those produced by the small cortical region of Figure 5-1.

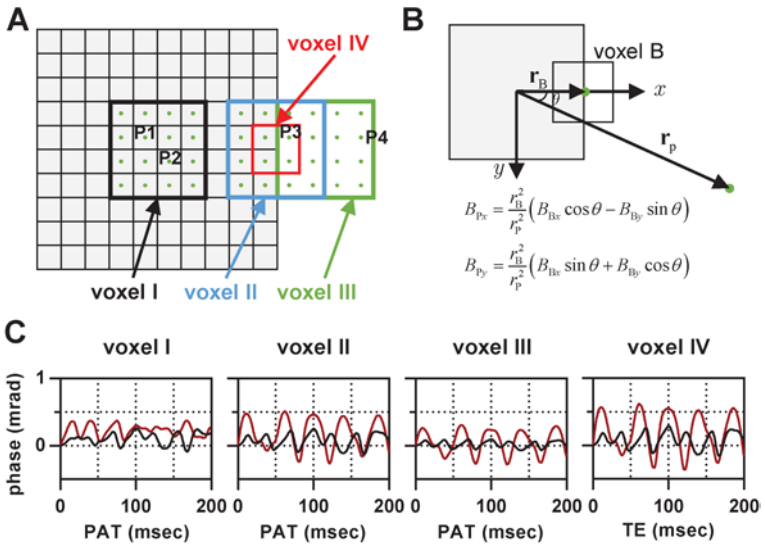

Figure 5-9 The MRI signal phase change produced by an extended cortical region consisting of 10x10 sub-regions.

Shown are (A) the extended cortical region, the cortical sub-regions (gray squares), the locations of voxels of interest, and the sampling points, and (B) the analytic expression used to calculate the magnetic fields at location P, and (C) the MRI signal phase changes in four voxels in the presence of an extended cortical region. The black and red lines in (C) show the signal phase produced by the x- and y- NMF components, respectively. The signal phases were calculated based on the same data as used in Figure 5-7. The spatial NMFs produced by the extended cortical region are also shown in Figure S6 in Appendix C.

	B_x	B_y
P1	$B_{Ax} - 0.07B_{Bx} + 0.07B_{By}$	$B_{Ay} - 0.07B_{Bx} - 0.07B_{By}$
P2	$B_{Ax} + 0.07B_{Bx} - 0.07B_{By}$	$B_{Ay} + 0.07B_{Bx} + 0.07B_{By}$
P3	$1.22B_{Bx} + 0.04B_{By}$	$-0.04B_{Bx} - 1.22B_{By}$
P4	$0.39B_{Bx} + 0.02B_{By}$	$-0.02B_{Bx} + 0.39B_{By}$

Table 5-2 Expressions for the x- and y-components of the magnetic field for the four locations, as shown in Figure 5-9, as a function of the magnetic field of voxel A and B.

The signal phase changes was calculated for three 4.5x4.5 mm voxels, labelled voxel I, II and III in Figure 5-9A. In each of the voxels, the magnetic fields produced by the extended cortical region are calculated at sampling 16 points and used to calculate the signal phase change. The results are shown in Figure 5-9C. In comparison to Figure 5-7, voxel I has the similar signal phase changes as voxel A, but voxel II has slightly larger signal phase changes than voxel B. Similarly, voxel III has slightly larger signal phase than

voxel C. Overall, the increase in voxel volume from 2.0 mm^3 to 200 mm^3 has increased the signal phase change by approximately 17.6% at the edge and 11.2% away from the cortical region (peak to peak comparison for voxel B and II, and voxel C and III,), and the effect is negligible inside the cortical region (voxel I). To example the effect of voxel size on the phase signal, I have provided a extended cortical region result for voxel IV with dimensions 2.2x2.2 mm. A reduction in voxel volume leads to increased signal phase changes. The results indicate that both voxel size and location affect NMF signals, important information for planning experiments to maximize the potential of observing an effect.

5.4 Discussion

MRI-based detection of neuronal currents is yet to be convincingly demonstrated. An important technique to inform experimental design is to simulate realistic neuronal current distributions to study likely effects on MRI signal magnitude and phase. Here, I simulated the expected nc-MRI signal using a new NMF model based on my previous work. I have made three important advances over previous studies: a). the LCM was used to simulate neuronal activities with different types of neuronal oscillations, allowing their effects on the MRI signal to be elucidated; b). the LCM is based on a realistic cortical architecture incorporating lamination, cortical synaptic connections and varying neuronal morphology, all of which contribute to the simulation of realistic spatial neuronal current distributions; and c). I simulated the conduction of APs and PSPs, allowing the evolution of temporal NMF variations to be examined.

5.4.1 Neuronal current MRI signals

The signal differences between the spontaneous and stimulated activity and across the voxels predicted by this study may be explained by the temporal and spatial cancellation of NMFs. Temporal cancellation occurs because PSPs comprise changes with opposing phases reflecting membrane depolarization and repolarization (see Figure 5-2). These produce sequential changes in magnetic fields of opposite sign with opposing effects on signal phase resulting in cancellation over time. Temporal cancellation may explain signal differences between spontaneous activity and stimulated activity. During spontaneous activity, neuronal activity is unsynchronised, with little correlation between PSPs. At any

given time, there are almost the same number of membrane potential depolarisations and repolarizations taking place in a given volume. Because the produced magnetic fields largely cancel out, only the residuals contribute to the MRI signal. Temporal cancellation, however, diminishes during stimulated activity. Strong neuronal oscillatory behaviour produces synchronised PSPs, which exert their effects at about the same time. The PSPs also produce synchronised membrane potential depolarisations and repolarizations. The resulting collective membrane potential depolarization does not overlap with the collective membrane potential repolarization over time. Therefore, they do not cancel out but produce two sequential magnetic fields of opposite polarity. Synchronised neuronal activity thus produces oscillatory magnetic fields. Temporal cancellation does not affect AP magnetic fields because of their shorter durations.

Neuronal current MRI signals may also be damped by spatial cancellation of NMFs. In principle, a membrane potential change produces opposite magnetic fields on different sides of the axon/dendrite. If they are both included in a voxel, they may also cancel each other out, and contribute little to the mean NMF. The effect of spatial cancellation explains the differences observed between the three voxels studied. The MRI signal change for voxel A is strongly reduced through spatial cancellation, because the voxel is symmetric around the neuron. Voxels B and C have much weaker spatial cancellation, because they are located eccentrically with respect to the neuron. One consequence of spatial and temporal cancellation is that the nc-MRI signal does not depend directly on the intensity of neuronal activity. Instead, it is more likely to be a function of spatial and temporal differences (i.e. spatial gradients and temporal variations) in neuronal activity.

The simulation results imply that the magnetic fields produced by PSPs are much larger than those produced by APs. The primary reason for this is that PSPs outnumber APs by a factor of thousands, and PSPs have a 10 times longer duration than APs. This finding, however, does not agree with the result generated by the identical neuron model (Cassara et al., 2008), where APs were found to mostly contribute to the NMFs. Three factors may contribute to the discrepancy. Firstly, neurons of the identical neuron model were set to fire with the same temporal pattern. Therefore APs of all neurons completely overlapped and resulted in strong magnetic field peaks. Because the temporal pattern of APs in the model is asynchronous, strong NMF peaks due to firing of APs alone is unlikely. Secondly, the neuron in the identical neuron model has as little as 100 active synapses on

the dendritic tree, while a neuron in the model can have more than 5000 synapses that are able to receive afferent spikes from other neurons. Consequently, in my model, neurons can have 50 or more times as many PSPs as those in the identical neuron model. Thirdly, back-propagation of APs on dendrites is evident in the identical neuron model (see Figure 6 of (Cassara et al., 2008)) and is likely to add to the AP magnetic field peaks. The present model does not incorporate this effect.

The effect of voxel size on signal phase change was examined. Small voxels are likely to produce large phase changes. For example, the phase change of voxel IV (shown as a blue square in Figure 5-9) is 22% larger than that of voxel III. Furthermore, neuronal currents produce inhomogeneous magnetic fields that have peaks and troughs around the boundary of neuronal activity (see Figure 5-5). The averaging of NMFs within a voxel behaves as a low-pass filter with cut-off frequency determined by the inverse of the voxel size. Therefore, the magnetic field peaks and troughs can only be discerned by employing small voxels. The use of large voxels tends to reduce the magnetic field inhomogeneity and smooth out the peaks and troughs. In the extreme case when the voxel is much larger than the activated brain region, the signal phase change is zero, because magnetic fields must form closed loops (the curl of the magnetic field is zero).

The simulation results indicate that neuronal current induced signal phase changes depend on the location of the voxel relative to the activated brain region, and a maximized phase change can be observed at the boundary of neuronal activity (see Figure 5-1 and Figure 5-9). Such a clear boundary of may not be present in the brain. Hence, cortical signalling is likely to be a combination of the behaviour observed for voxels A, B and C. Besides, the neuronal activity of a large brain region may not be synchronous, since oscillations of cortical sub-regions may have different phases. This spatial inhomogeneity of neuronal activity can reduce the level of spatial cancellation of NMFs, which may result in an increased neuronal current signal. The size of the effect depends on the extent of the spatial inhomogeneity of neuronal activity.

In a previous study, the neuronal current signals in organotypic rat brain cultures were measured (Petridou et al., 2006). A 3 to 14 mrad phase signal change and an absence of signal magnitude change at 3T with a spin-echo echo-planar imaging (TE = 60 msec, TR = 1sec) sequence were observed. The results confirm my prediction that neuronal current-induced signal phase changes are more pronounced than changes in signal magnitude. I

compared the size of the observed phase change with my predictions. The volume of the culture (1.9-3.2 mm^3) is comparable to the cortical volume simulated in the present model (2.0 mm^3, see Figure 5-1), but the volume of the voxel (24 mm^3) is about 60 times larger than the small voxels of Figure 5-1 (0.4 mm^3). Since the locations of the voxels relative to the culture are unclear, I estimated the phase change in voxels with a similar volume at various locations. The maximum predicted signal phase change for voxels at different locations is in the range of 0.01-0.1 mrad. Therefore, the experimentally observed signal phase is around 140 times more than my prediction. Several factors may account for this difference. The seizure-like activity of the brain culture imaged in the experiments is likely to produce stronger neuronal currents than the neuronal activity generated by LCM. In my simulation, the amplitude of the neuronal oscillation is about 15 spikes/sec (from 10 spikes/sec to 25 spikes/sec), however, pyramidal neurons in the brain can fire at more than 100 spikes/sec. If a linear relationship between the oscillation amplitude and the signal phase change is adopted, the difference in neuronal activity may account for up to 10 times the difference. Furthermore, a free induction decay or gradient echo sequence was assumed in the simulation, but a spin echo sequence was used in the experiments. The spin echo sequence may acquire two times larger signals, if the 180 degree refocusing pulse is applied when neuronal magnetic fields change sign (Petridou et al., 2006). Other factors, such as the shape of the culture and neuronal arrangement may also affect the predicted signal but their effects are difficult to estimate. Having taken all of these factors into consideration, the experimentally observed phase changes may still be 3-7 times bigger than predicted.

The finding that NMFs oscillate with neuronal activity aligns with MEG measurements. In MEG experiments, when a subject is presented with an intermittent visual stimulus at a certain frequency, NMFs of the same frequency can be observed at the scalp. This effect has been used to study neuronal activity during a visual attention task, a method called “frequency-tag” (Tononi et al., 1998; Srinivasan et al., 1999; Chen et al., 2003). My simulations provide a theoretical explanation for the frequency-tag effect.

5.4.2 Implications for nc-MRI

The simulation results imply that nc-MRI may not be useful as a general tool for imaging neuronal activity as a form of functional magnetic resonance imaging because nc-

MRI signals are sensitive to spatial gradients and temporal variations as opposed to the intensity of neuronal activity. Given the small size of the signal, the results of this study predict that neuronal current signal may only be detectable for strong bursts of neuronal activity, as induced by stimuli or associated with pathological synchronised discharges such as epileptic seizures. The simulations demonstrate that the magnitude change of the induced MRI signal change is too small to be detectable with current techniques but that the phase signal can potentially be detected. This coincides with previous experimental findings (Bodurka et al., 1999; Petridou et al., 2006). However, careful consideration must be given to experimental design.

A key prediction of the present simulations is that synchronised neuronal activity produces a periodic phase signal (see Figure 5-7). In view of this, the echo times (TE) for MRI acquisitions should be matched with the frequency of neuronal activity to maximize the chance of observing an effect. The simulation suggests that the optimal echo time is n+0.5 times the period of the major oscillation in neuronal activity, where n is a non-negative integer. For example, to measure a neuronal activity with 25 Hz oscillation (period = 40 msec), a time of 20, 60 or 100 msec should be chosen. Sample induction time needs to be appropriately chosen to ensure that NMFs do not change sign during the echo time. This requires MRI scans to be synchronised with the onset of stimulated neuronal activity.

It has been demonstrated that transient magnetic fields as small as 200 pT lasting for 40 msec, similar to the NMFs predicted by my model, can be detected in phantoms using MRI (Bodurka and Bandettini, 2002). But, detection of neuronal currents of the brain still faces numerous technical challenges. Neuronal activity is also associated with BOLD and diffusion signal effects, which may lead to temporal signal phase changes that mask the action of neurons. The BOLD effect produces signal phase changes that are approximately one tenth of a radian at 4 Tesla (Menon, 2002), which is two orders of magnitude larger than the neuronal current induced phase change. Water diffusion changes the phase of proton precession in a random manner. Essentially, the phase changes cancel and MRI signal magnitude decreases. Another challenge facing nc-MRI experiments is to suppress the noise caused by scanner instability and physiological processes, including respiration and cardiac actions. Scanner-related and physiological noise affect signal phase more prominently than signal magnitude (Hagberg et al., 2008; Petridou et al., 2009). Hagberg et al. (2012) showed the respiration-related signal phase

change averaged across an imaging slice is about 280 mrad in the human brain at 3T, corresponding to a 0.012 ppm change of the imaging magnetic field, and the phase change due to the instrumentation and caused by thermal noise contribute at nearly the same level. They also demonstrated that high-pass spatial filtering can suppress the noise in signal phase to below 5 mrad, because the noise usually has a large spatial extent (> 1 cm) (Hagberg et al., 2012). In view of the simulation results, the noise in signal phase has to be further suppressed by at least one order of magnitude to be able to deduce the neuronal current induced signal phase change.

The simulations also predict that the nc-MRI signal in the direction orthogonal to the cortex is likely to be significantly smaller than in the tangential (horizontal) direction, in line with the results of previously conducted phantom (Bodurka et al., 1999) and simulation (Luo et al., 2011b) experiments. This is a natural consequence of the dendritic trees of pyramidal neurons being spread more widely in the vertical than in the horizontal direction. Because the architecture of cerebral cortical convolutions of the cerebral cortex results in multiple orientations of cortical neurons, nc-MRI needs to be performed in at least two directions to capture the complete neuronal current signal (see, for exmaple, Lother et al., 2013), and images in all three coordinate directions are required to reconstruct the spatial distribution of signal sources.

In conclusion, I have developed a new model to calculate neuronal current induced MRI signal magnitude and phase changes. The results suggest that the phase change produced by synchronised neuronal activity may be detectable with current MRI equipment whereas signal magnitude changes are below currently detectable levels. Signal acquisition timing and duration have to be appropriately chosen to maximise the effect of NMFs on the MRI signal.

Chapter 6

Detection of neuronal current *in vivo* using MRI: the challenge of noise in MRI signal

6.1 Introduction

Several MRI protocols have been proposed to image neuronal currents. Bodurka and Bandettini (2002) found that a transient 200 pT magnetic field change lasting 40 msec in a physical phantom, which is similar to the NMFs in the brain, could be detected using a 3T MRI scanner. Petridou et al. (2006) were able to detect consistent MRI signal phase changes in organotypic rat brain cultures, in which neuronal activity was pharmacologically elicited. However, inconsistent results have been reported for *in vivo* human experiments (see, for example Xiong et al., 2003; Chu et al., 2004; Parkes et al., 2007). Early nc-MRI experiments explored the use of gradient recalled echo echo-planar imaging (GRE-EPI) and spin echo echo-planar imaging (SE-EPI) sequences (Joy et al., 1989; Scott et al., 1991; Scott et al., 1992; Kamei et al., 1999; Bodurka and Bandettini, 2002). EPI is sensitive to the direct current components of NMFs. However, one prediction from my simulation studies is that neuronal activity generates relatively small direct current NMFs and relatively large oscillating NMFs and that the NMFs change sign periodically (refer to Figure 5-7 and Figure 5-8 in Chapter 5). When imaged with an EPI sequence, the oscillating NMFs may change signal phase during the spatial encoding period, producing inconsistent phase changes in acquired images.

A number of new MRI paradigms have been proposed to image oscillating NMFs. Stimulus-induced rotatory saturation (SIRS) sequences rely on neuronal currents producing rotary saturation of spin-locked magnetization (Witzel et al., 2008). The spin-lock state can be tuned to match the frequency of oscillating NMFs (Halpern-Manners et al., 2010). However, the grey and white matter in the brain have short spin-lattice relaxation time in the rotating frame (known as $T_{1\rho}$) (less than 100 msec at 1.5T)

(Borthakur et al., 2006), which imposes a primary limitation on the spin-lock time and consequently reduced the sensitivity of the technique. Ultra-low field MRI, in which the micro Tesla imaging field allows resonant interactions between NMFs and spin magnetization, has also been proposed to detect neuronal currents (Kraus et al., 2008). Even with many theoretical advantages, *in vivo* nc-MRI experiments using these techniques face the challenge of overcoming the noise in MRI signals and a low signal-to-noise ratio (SNR) level.

In this chapter, I first calculate the neuronal current-related MRI signal changes under acquisitions using two common MRI techniques, namely gradient echo and spin echo sequences. Based on the calculation, I tested the imaging of neuronal currents using synchronised multi-echo gradient recalled echo (MEGRE) and synchronised multi-echo spin echo (MESE) sequences. These tests involved neuronal currents evoked by intermittent photic stimulation. To study neuronal current-related signal changes in the low SNR regime, I also examined methods to reduce the effects of various factors that contribute to noise in MRI signals. My work provides a platform for further studies to improve MRI hardware and software (sequences and image analysis methods) to the degree required to capture the nc-MRI signal in the human brain.

6.2 Theory

To analytically calculate the nc-MRI signal, a mathematical representation of temporal NMFs in response to a stimulus, i.e. a NMF response function, is required. Neuronal activity (i.e. spike and PSP densities[1]) in the brain may display different temporal profiles associated with different stimuli, however I confined my calculation to the case of synchronous neuronal activity in the brain, as evoked by intermittent photic stimulation at a specific frequency. For this case, the temporal profile of the signal is likely to follow a periodic function (Rager and Singer, 1998; Nunez and Srinivasan, 2006). Though the

[1] Strictly speaking, PSP density is not always consistent with spike density in the brain. However, in the cortex where most local neuronal processes happen, the two variables are generally consistent in relatively large volumes (>1 mm^3) (see, for example, Berens et al. 2010). In this chapter, I do not differentiate the two and broadly refer to them together as "*neuronal activity*".

periodic function may also have a complex shape (some examples are shown in Figure 6-1), I represented it using a simple sinusoidal function (i.e. neuronal activity (A) of Figure 6-1). The sinusoidal shape helps to simplify the calculation of nc-MRI signal whilst keeping the periodic characteristics of the neuronal activity. The impact of the temporal profile of neuronal activity on nc-MRI signal formation is discussed later.

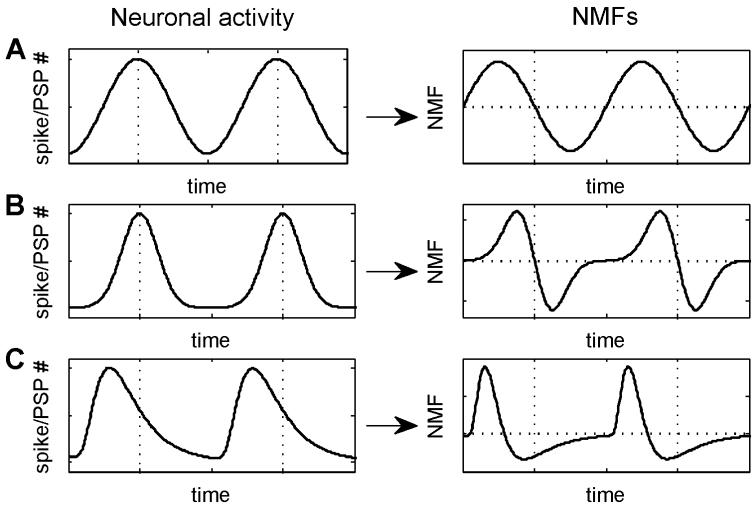

Figure 6-1 Illustrated are three possible temporal profiles for neuronal activity and the corresponding NMF shapes.

The three temporal profiles are driven from (A) a sine function, (B) a Gaussian function, and (C) a log-normal function. The NMFs shown in the right panel are calculated as the temporal derivatives of the corresponding neuronal activity. The vertical dashed lines indicate the time point that the 180 degree refocusing RFs are applied during MESE acquisition (see the text for more information). The figures are plotted in arbitrary units.

My simulations, presented in Chapter 5, suggest that NMFs are likely to be a function of the derivative of neuronal activity (refer to Section 5.3 and 5.4 in Chapter 5); thus a neuronal activity with sinusoidal temporal profile also produces sinusoidal NMFs (see Figure 6-1). With this notion in mind, the NMFs of a voxel can be written as

$$B_z^{\mathrm{NMF}} = B_{z0}^{\mathrm{NMF}} \sin(\omega t + \phi_0)\,, \tag{6.1}$$

where B_z^{NMF} represents the neuronal magnetic field components that are parallel to the imaging field, and B_{z0}^{NMF} represents the amplitude of oscillation, ω is the oscillation frequency, and ϕ_0 is the initial phase. For a GRE acquisition, the signal phase change caused by NMFs is

$$\begin{aligned}\Delta\varphi^{\mathrm{GRE}} &= \gamma\frac{1}{V}\int_V\int_0^{t_{\mathrm{E}}} B_{z0}^{\mathrm{NMF}}\sin(\omega t+\phi_0)\ dtdv \\ &= \frac{2\gamma}{\omega}\sin\left(\frac{\omega t_{\mathrm{E}}}{2}\right)\sin\left(\phi_0+\frac{\omega t_{\mathrm{E}}}{2}\right)\left\langle B_{z0}^{\mathrm{NMF}}\right\rangle_V\end{aligned} \tag{6.2}$$

and for a SE acquisition, it is

$$\begin{aligned}\Delta\varphi^{\mathrm{SE}} &= \gamma\frac{1}{V}\int_V\left[\int_{t_{\mathrm{E}}/2}^{t_{\mathrm{E}}} B_{z0}^{\mathrm{NMF}}\sin(\omega t+\phi_0)dt-\int_0^{t_{\mathrm{E}}/2} B_{z0}^{\mathrm{NMF}}\sin(\omega t+\phi_0)dt\right]dv \\ &= \frac{2\gamma}{\omega}\left\langle B_{z0}^{\mathrm{NMF}}\right\rangle_V\cos\left(\phi_0+\frac{\omega t_{\mathrm{E}}}{2}\right)\left[1-\cos\left(\frac{\omega t_{\mathrm{E}}}{2}\right)\right]\end{aligned}, \tag{6.3}$$

where V is the volume of the voxel, $\left\langle B_{z0}^{\mathrm{NMF}}\right\rangle_V$ represents the average value of B_{z0}^{NMF} in volume V, and t_{E} is the time to echo (TE) (refer to Section 3.4.1 in Chapter 3 for the derivation). The detected phase change can be maximized through optimization of TE and ϕ_0, which for the GRE and SE sequences are

$$\max\left(\left|\Delta\varphi^{\mathrm{GRE}}\right|\right)=\frac{2\gamma}{\omega}\left\langle B_{z0}^{\mathrm{NMF}}\right\rangle_V \tag{6.4}$$

and

$$\max\left(\left|\Delta\varphi^{\mathrm{SE}}\right|\right)=\frac{4\gamma}{\omega}\left\langle B_{z}^{\mathrm{NMF}}\right\rangle_V \tag{6.5}$$

respectively, and the corresponding t_{E} and ϕ_0 are

$$\begin{aligned}&t_{\mathrm{E}}=(2\,\mathrm{n}+1)\pi\ /\ \omega \\ &\sin(\phi_0)=0\end{aligned}, \tag{6.6}$$

for the GRE acquisition, and

$$\begin{aligned}&t_{\mathrm{E}}=(4\,\mathrm{n}+2)\pi\ /\ \omega \\ &\sin(\phi_0)=0\end{aligned}. \tag{6.7}$$

for the SE acquisition, where n is a non-negative integer.

In Chapter 5, I showed that synchronous neuronal currents produce NMFs that change sign regularly (see Section 5.3 in Chapter 5 and Figure 6-1). When imaged using a GRE sequence, positive and negative NMFs shift the phase of magnetization precession to the opposite direction, which could lead to a reduced phase change for certain echo times. For the GRE sequence, signal phase change could be maximized by using an echo time that covers only the positive (or only the negative) NMF range of an oscillation period. However,

this is not the case for SE sequences. Because the refocusing RF pulse can reverse the phase of the magnetization (refer to Figure 3-5 in Chapter 3 for the effects of the refocusing RF pulse), the phase accumulated before and after the application of the refocusing RF pulse will cancel out when the NMFs have the same sign before and after the application of the RF pulse, or enhance each other if they have different signs. Hence, if the refocusing RF pulse is applied when NMFs change sign, both positive and negative NMFs shift the signal phase to the same direction, producing an enhanced signal phase change. Therefore, a SE acquisition may potentially measure a larger phase change than a GRE acquisition.

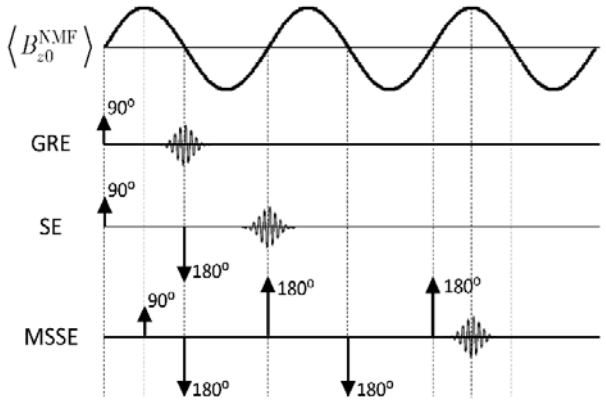

Figure 6-2 Sequences used to detect MRI phase change produced by oscillating magnetic fields.

Illustrated are the oscillating neuronal magnetic fields, and signal detected using gradient echo, spin echo and multi-echo spin echo sequences.

Based on the foregoing observations, I proposed that a synchronised MESE sequence can be used to increase the potential detectability of neuronal current signals. While a SE acquisition can accumulate signal phase change in one oscillation period, a multi-echo spin echo (MESE) sequence has the potential to accumulate the phase change in multiple oscillation periods, because multiple refocusing RF pulses are applied at times when the oscillatory NMFs change sign, further increasing the influence of neuronal currents on the MRI signal. The maximum detectable signal phase change measured by the MESE acquisition is

$$\max\left(\left|\Delta\varphi^{MESE}\right|\right) = N_{\mathrm{echo}} \cdot \frac{2\gamma}{\omega}\left\langle B_{z0}^{\mathrm{NMF}} \right\rangle_V = N_{\mathrm{echo}} \cdot \max\left(\left|\Delta\varphi^{\mathrm{SE}}\right|\right) \tag{6.8}$$

where N_{echo} is the echo train length (ETL). The corresponding TE and ϕ_0 are

$$TE = \pi/\omega$$
$$\cos(\phi_0) = \pm\pi \ / \ 2 \tag{6.9}$$

MESE sequence can measure a phase change N_{echo} times larger than SE sequence.

Though equations (6.4)-(6.9) are derived based on a sinusoidal neuronal activity, similar formulae can be generated for all neuronal activity with symmetric temporal profiles within a single period. However, for neuronal activity with asymmetric temporal profiles within a single period, the MESE acquisition would measure a much smaller phase change. For example, neuronal activity A and B shown in Figure 6-1 both produce an enhanced phase change, whilst neuronal activity C produces a phase change 40% smaller than neuronal activity A and B, if they have the same magnitudes and imaged with a MESE sequence satisfying equation (6.9). This is because the refocusing RF pulse is not applied when NMFs change sign, and phase changes produced by positive and negative NMFs cancel out partially. Due to the neuronal adaptation effect, slow-varying intermittent stimulation (<5 Hz) is likely to produce neuronal activity with temporal profile similar to shape C of Figure 6-1 (Saul and Cynader, 1989; Kohn, 2007). But neuronal activity under fast intermittent stimulation displays a more symmetric temporal profile (Rager and Singer, 1998; Noguchi et al., 2004). For such reasons, the MESE approach is likely applicable for imaging neuronal currents produced by rapidly oscillating neuronal activity.

Even with these advantages, the MESE sequence is likely to be susceptible to contamination from signal phase noise. Firstly, the refocusing RF pulses of the MESE sequence are usually not perfectly homogeneous in space. The flip angles produced by the RF pulses are not homogeneous across a slice. They can introduce additional phase changes to the signal, leading to an increase in phase noise. Secondly, the formation of a spin echo usually takes a longer time than a gradient echo. The increased time to echo can lead to a low signal-to-noise ratio and large phase noise (Petridou et al., 2009). The noise in MRI signals poses a major challenge to nc-MRI experiments, because MRI signal change due to NMFs has been estimated to be small. In light of this, I also propose that neuronal current signals can be extracted from noisy MRI signals using a synchronised MEGRE sequence. Because a gradient echo can be formed within a few milliseconds, MEGRE sequences can be used to acquire MRI signals at multiple consecutive time points. A key prediction of the simulations presented in Chapter 5 is that the signal phase change induced by oscillatory neuronal currents also oscillates at the same frequency.

This feature could potentially be used to distinguish the neuronal current signal from changes due to BOLD effects or noise, because BOLD effects remain relatively constant once saturated and signal noise is uncorrelated with neuronal oscillation. Thus, when measured at different time points within a narrow time window, neuronal current signal but not BOLD effect or noise, would vary with neuronal oscillation. Because a MEGRE sequence is capable of acquiring MRI signals at a series of closely-spaced time points, the inherent oscillation of neuronal current signals may potentially be deduced from the temporal profile of the MRI signals.

The two proposed methods are innovative because they harness two temporal characteristics of NMFs. It is important to test both proposed solutions because each has theoretical advantages. Since MESE is less susceptible to the BOLD effect, it may reflect neuronal currents more accurately than MEGRE. In addition, the fidelity of neuronal current signals measured by MESE can easily be tested by changing the time delay between stimulus onset and MRI acquisition.

In this Chapter, five experiments were conducted to help evaluate the potential of detecting nc-MRI signal using existing MRI techniques. As demonstrated in Chapter 5, MRI signal phase is more sensitive to changes due to neuronal activity than signal magnitude, in the first three experiments I investigated factors that may influence signal phase (Experiments 1, 2 and 3). I then conducted nc-MRI experiments using MESE and MEGRE sequences (Experiments 4 and 5). Experiment 1 evaluates the effectiveness of removing unwanted signal phase changes from raw MRI signal using post-processing methods. Experiment 2 establishes the relationship between the noise in MRI signal phase and echo time. It also evaluates noise in averaged signal phases of data from multiple acquisition. Experiment 3 investigates the impact of motion in MRI signal phase. Experiments 4 and 5 employ MESE and MEGRE sequences to detect the signal phase changes due to neuronal activity stimulated by intermittent light visual.

The MEGRE nc-MRI experiments were conducted on a 1.5T MRI system, and the MESE nc-MRI experiments were conducted on a 3T MRI system. The 1.5T system was used for the MEGRE nc-MRI experiments because the BOLD effects and signal noise are likely to be smaller at 1.5T. The 3T scanner was used for the MESE nc-MRI experiments, because the MESE sequence is resilient against contamination of BOLD effects and other

MRI noise, and the 3T system has current generation hardware and software, which may yield a higher signal-to-noise ratio than the 1.5 T system.

6.3 Experiment 1: corrections for MRI signal phase

In this experiment, I evaluated the effectiveness of high-pass spatial filtering and linear regression temporal correction methods in removing unwanted phase changes from raw MRI signal. I tested the hypothesis that phase changes caused by sources outside the brain are predominantly at low spatial frequencies and thus can be removed using high-pass spatial filtering, and that phase changes caused by tissue susceptibility effects and saturated BOLD response vary slowly during a scan and thus can be minimised by using a linear regression temporal correction post-processing method.

6.3.1 Materials and methods

MRI scanner: A Siemens MAGNETOM Sonata 1.5 T human scanner was used for this experiment. This field strength was used rather than higher field strengths because it has been reported that noise in MRI signal phase scales with imaging field strength (Wowk et al., 1997; Van de Moortele et al., 2002; Hagberg et al., 2008). Ethics approval was obtain from the Human Research Ethics Committee of The University of Queensland. The experimental data were collected using a Siemens 4-channel receive-only head coil.

Subject and phantom: A healthy 31 year old male volunteer was scanned. For comparison, a standard Siemens phantom, which contains water with 0.125% $NiSO_4$ and 0.5% NaCl, was imaged using the same sequence and parameter settings as the human experiments. The diameter of the phantom is 12 cm, and the height is 25 cm.

Data collection: The Siemens proprietary Fast Low Angle Shot (FLASH) sequence with the following parameter settings was used to collect data: the flip angle was 25 degrees; ten TEs from 5 msec to 50 msec in 5 msec steps were used; the TR was 200 msec; the in-plane resolution was 1.3 by 1.3 mm^2 (the image matrix was 192 by 192) with a slice thickness of 2 mm. The acquisition was repeated 50 times. Magnitude and phase images were obtained from the scanner and used to reconstruct raw MRI signals.

Image processing: Besides NMFs, factors such as brain tissue susceptibility, BOLD response, and thermal noise, can affect MRI signal phase. Two phase image processing

methods, a high-pass spatial filtering method and a linear regression temporal correction method, were tested for their effectiveness in removing unwanted phase changes from raw MRI signals. For *high-pass spatial filtering*, a two-dimensional spatial high-pass homodyne filter was employed to remove low spatial frequency phase noise (Noll et al., 1991). This method was chosen because I hypothesised that phase changes caused by external magnetic fields such as those generated by the heart and imperfect field gradients concentrated at low spatial frequencies (Brainovich et al., 2009; Hagberg et al., 2012). The high-pass filtering can be stated as

$$\varphi^{\mathrm{H}} = \angle(S \,/\, S^{\mathrm{L}}) \tag{6.10}$$

where S and S^{L} are the raw complex signal, low-pass filtered complex signal, respectively; $\angle(\bullet)$ computes the phase of a complex number, and φ^{H} is the high-pass filtered signal phase. The low-pass filtered signal was generated via

$$S^{\mathrm{L}} = \tilde{\mathrm{F}}^{-1}\left[\tilde{\mathrm{F}}(S) \cdot H\right]. \tag{6.11}$$

where $\tilde{\mathrm{F}}(\cdots)$ and $\tilde{\mathrm{F}}^{-1}(\cdots)$ denote the Fourier and inverse Fourier transforms, and H is a 2-dimensional symmetric Hamming window (Bernstein et al., 2004). The size of the Hamming window was set to one fourth of the image size. The process of homodyne filtering automatically resulted in unwrapped high-pass phase images. The high-pass spatial filtering was implemented using MATLAB 2014a.

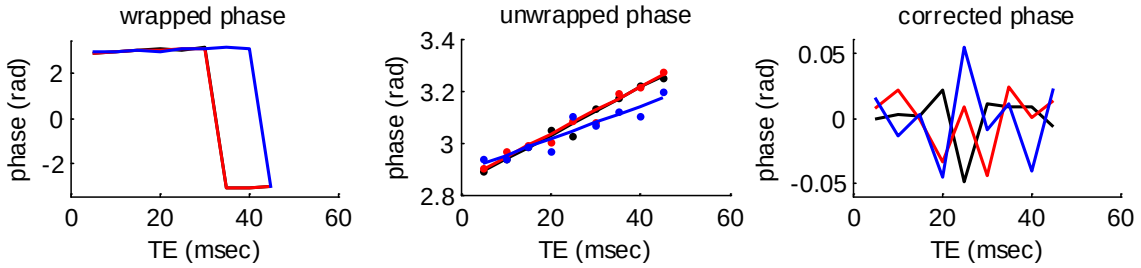

Figure 6-3 Linear regression temporal correction of phase time courses.

Shown are the steps used to correct the phase time course of MEGRE signals. The left panel shows the phases measured by the scanner, the middle panel shows the unwrapped temporal phases (dots) and the linear regression lines, and right panel shows the corrected phase time course. The data come from a MEGRE phantom image. The colours represent signal phases of three voxels in the centre of the phantom.

In the *linear regression temporal correction* method, the signal phases of each voxel were first unwrapped in time, then fitted with a linear function, i.e.

$$\phi = \Delta f \cdot TE + \varphi_0 \,, \tag{6.12}$$

where Δf is the slope of the function, corresponding to the frequency shift of spin precession. The resultant linear signal phases represent the phase changes produced by effects that remain unchanged, or vary slowly, during a scan. These effects may include inhomogeneous imaging fields, tissue susceptibility effects, and the saturated BOLD effect. The deviation of the measured phases from the fitted phases, referred to as *temporally corrected phases*, are produced by effects that vary significantly during a scan, such as NMFs, electronic instability, and thermal noise. Therefore, the temporally corrected phases potentially contain information of NMFs. Figure 6-3 illustrates the steps involving in the linear regression temporal correction post-processing of MRI signal phases. This method was also implemented using MATLAB 2014a.

Noise evaluation: The noise level of phase images was quantified to assess signal phase stability. The phase noise level was computed as the standard deviation of signal phases of a voxel across different repetitions of the data. Furthermore, a two-sample voxel-by-voxel *F*-test, as implemented in Matlab 2014a, was employed to test the noise level difference between the spatially filtered signal phases and temporally corrected signal phases. The two samples compared in the *F*-test comprised the spatially filtered phases and temporally corrected phases of a voxel acquired from different repetitions of data. The null hypothesis was that the noise level of the corrected phases was not different from that of the filtered phases. The p-values of the *F*-test were calculated and reported.

6.3.2 Results and discussion

Figure 6-4 illustrates the effects of applying the two methods to a phantom image and a human brain image. In the figure, (A) and (F) are the magnitude images acquired from the scanner, and (B) and (G) are the corresponding phase images; (C) and (H) are spatially filtered phase images, and (D) and (I) are temporally corrected phase images; and (E) and (J) represent the slopes of phase time courses, i.e. Δf in Equation (6.12), for each voxel in the images. Figure 6-5 displays the noise maps of the spatially filtered phase images and temporally corrected phase images for the phantom data and the brain data. In the figure, (A) and (E) displays the phase noise maps after spatial filtering; (B) and (F) displays the phase noise maps after temporal correction; (C) and (G) displays the p-value of the

voxel-by-voxel F-test of phase noises; (D) shows a brain magnitude image with four regions of interest (ROI).

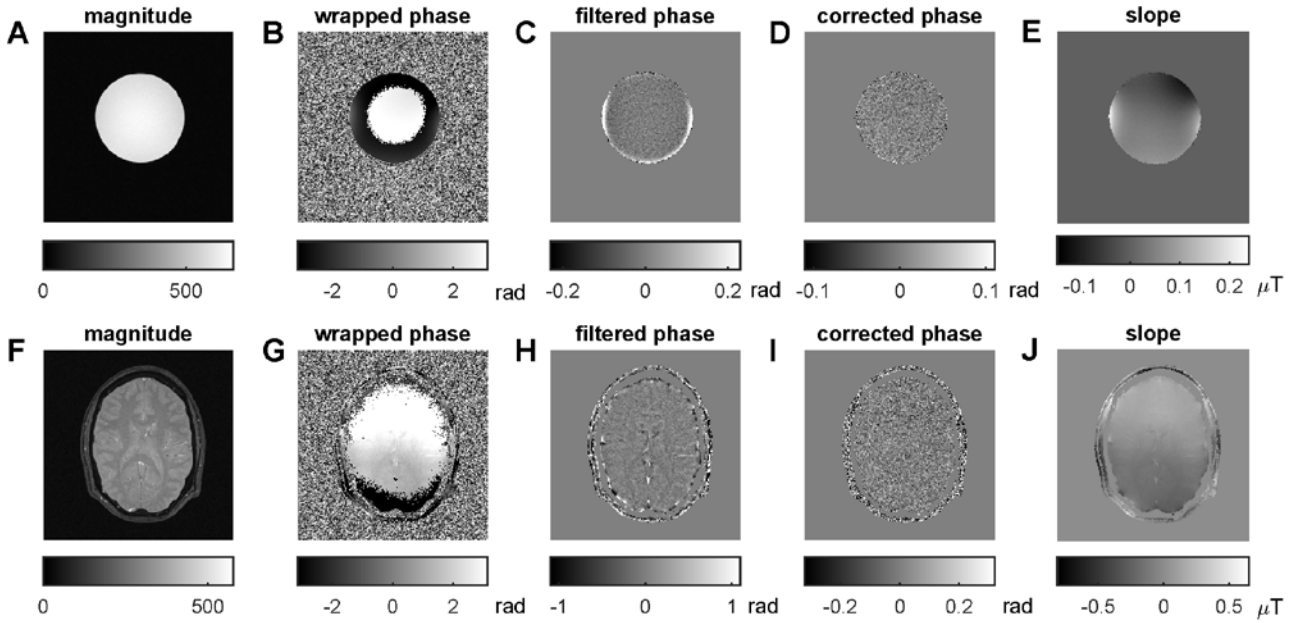

Figure 6-4 The effect of high-pass spatial filter and linear regression temporal correction on the phase image.

Shown are the magnitude (A and F) and phase (B and G) images obtained from the scanner, the high-pass spatially filtered phase images (C and H), linear regression corrected phase images (D and I), and the slopes of phase time course (E and J) of a sample phantom image (A-E) and a sample brain image (F-J). For clarity, the background is removed from the corrected, filtered phase images, and the slope images. The slope value shown in E and J were converted into magnetic field variations via $\Delta B = \Delta f/\gamma_p$, where Δf is the phase time course slope and γ_p is the proton gyromagnetic ratio. The phases were acquired at TE=40 msec. The brain image was acquired without specific stimulation or head holder.

While the two methods reduced phase noise significantly, the temporal correction method was more effective than the spatial filtering method (see Table 6-1). Firstly, the spatial filtering method introduced phase noise in regions where signal magnitude varies significantly. For example, the signal phase noise was significantly higher at the edge of the phantom in the filtered image, but this was not the case for the phase residual image. Similar effects were also observed in the brain image (see Figure 6-4). Furthermore, in the noise map of the filtered brain images, phase noise around the boundary of the cortex and the midline of the brain was significantly greater than within the brain parenchyma, but this was not observed in the noise map of the corrected images (see Figure 6-5). Secondly, the linear regression correction method removed phase change due to susceptibility effects (which may overshadow phase changes due to neuronal currents) simply through

the fitting process. The susceptibility effect was evident in the spatially filtered phase images, but it was not visible in the temporally corrected phase images (see Figure 6-4H and Figure 6-4I). The susceptibility effect was observable in images of the phase time course slopes (see Figure 6-4J).

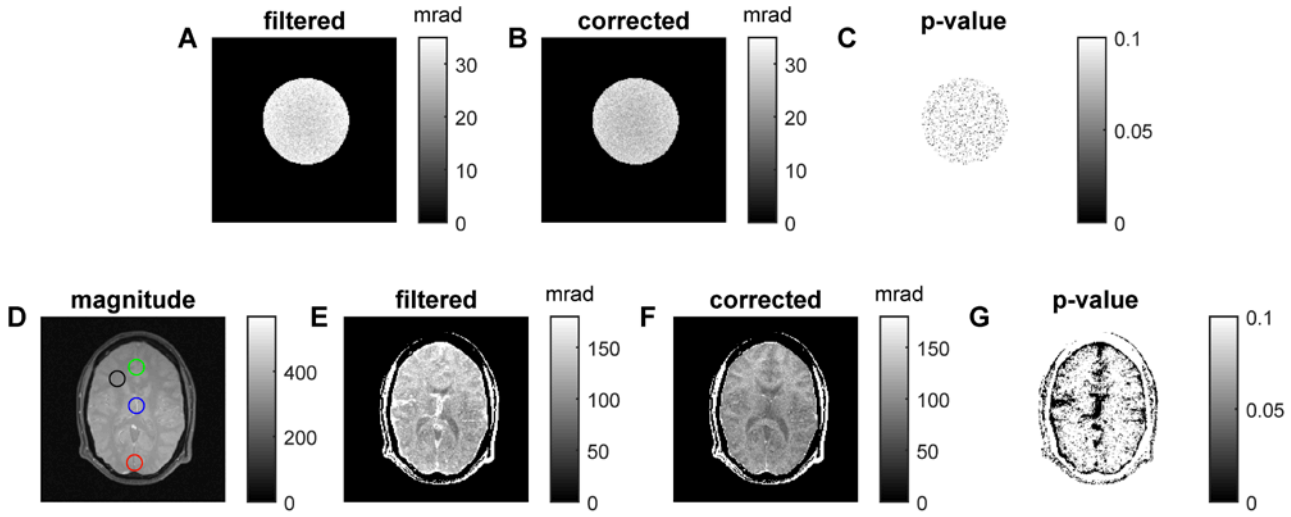

Figure 6-5 Phase noise maps under MEGRE acquisition.

Shown are phase noise maps in the phantom (A and B) and the brain (E and F) after high-pass spatial filtering (A and E) and linear regression temporal correction (B and F), four ROIs marked in a brain magnitude image (D), and the p-value for the F-test for the phantom image (C) and the brain image (G). The noise was calculated as the standard deviation of signal phases across about 50 datasets. The circles mark the regions, the mean noise levels of which are listed below (see Table 6-1). The brain images were acquired without specific stimulation or use of a head holder.

	Noise of filtered phases (mrad)	Noise of corrected phases (mrad)
ROI 1 (red)	153.9	112.4
ROI 2 (blue)	174.0	90.0
ROI 3 (black)	146.5	126.0
ROI 4 (green)	146.5	105.4

Table 6-1 Phase noise after high-pass spatial filtering and linear regression temporal correction.

Shown are the mean phase noise in four regions after the application of high-pass spatial filtering and linear regression temporal correction. The locations of the regions were indicated in Figure 6-5D.

One interesting finding of this experiment is that phase noise in the corrected phase images (as shown in Figure 6-5F) was higher in white matter than in grey matter. The phase noise in white matter was about 15-20% higher than that in grey matter (see ROI 3 and ROI 4 in Table 6-1). This phase noise difference was noticeable but less evident in the filtered phase image (see Figure 6-5E). The difference may be due to the magnetic susceptibility difference between white matter and grey matter. Because white matter has

a larger susceptibility, it produces a larger phase change than the grey matter under the same magnetic field conditions Therefore, temporally varying magnetic field disturbances produce larger phase noise in white matter in comparison to grey matter.

6.4 Experiment 2: phase noise as a function of echo time and voxel size

In this experiment, I aimed to evaluate the signal phase noise as a function of echo time and voxel size. I also investigated the behaviour of noise in signal phases when averaged over multiple datasets. The hypotheses were (1) phase noise is larger in MRI signal acquired at longer echo time and in smaller voxels (i.e. SNR is lower at long echo times and in small voxels), and (2) phase noise decreases when averaged over multiple datasets.

6.4.1 Materials and methods

This experiment used the same MRI scanner, subject and phantom as Experiment 1.

Data collection: MRI data collected in Experiment 1 were also analysed in this experiment. Additionally, lower resolution (1.95 by 1.95 mm^2 in-plane resolution with slice thickness of 2.50 mm) MRI data were collected using the same image acquisition parameters. Effectively, the voxel volume for the two datasets were 3.4 m µl and 9.4 µl. The low resolution data were collected for both the subject and phantom, and data acquisition was repeated 50 times to examine the effect of averaging.

Image processing: Raw MRI signals were processed using the linear regression temporal correction pipeline described under Experiment 1.

Noise evaluation: In this experiment, I assessed the effectiveness of averaging signal phases over multiple datasets on phase noise reduction. Averaged signal phases were calculated for N repetitions as:

$$\bar{\phi}(x,y) = \frac{1}{N}\sum_{i=1}^{N}\phi_i(x,y), \tag{6.13}$$

where $\phi_i(x,y)$ is the signal phase at voxel (x,y) of image i, N is the number of measurements used in the averaging. The noise level of averaged signal phases was defined as the standard deviation of averaged signal phases calculated from different

combinations of datasets. Noise was calculated for signal phases averaged from different number of datasets.

6.4.2 Results and discussion

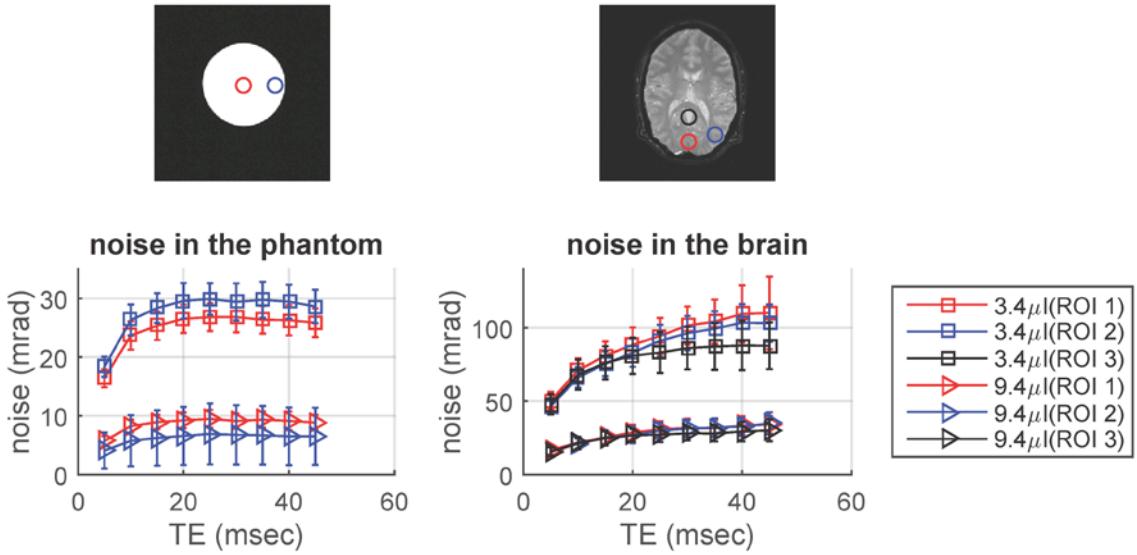

Figure 6-6 The dependence of phase noise on echo time and voxel size.

Shown are the phase noise levels measured at different echo times and with different voxel size in the phantom (left panel) and the brain (right panel). The colour of the plots corresponds to that of the different regions of interest (ROI) indicated in the magnitude image. The mean phase noise within ROIs is plotted, and the error bars represent the standard deviation of phase noise across voxels within the region.

Figure 6-6 displays the noise level in MRI signal phases measured at different echo times and with different voxel sizes. Generally, phase noise increases with echo time. For example, in the brain the phase noise at TE=40 msec is about 15-20% higher than that at TE=20 msec for each resolution. However, unlike in the human brain, the phase noise in the phantom study saturated after 20 msec. This was expected because the solution in phantom has a longer T_2* than brain tissue, hence the SNR does not drop as quickly in the phantom. Furthermore, as expected, large voxels have significantly smaller phase noise. When voxel size was increased from 3.4 µl to 9.4 µl, the noise level decreased on average by about 70% in the phantom and by about 67% in the brain.

Phase noise can be reduced through averaging multiple phase images acquired using the same sequence settings and parameters. Figure 6-7 shows the noise of signal phases averaged over multiple datasets. Phase noise decreases rapidly when averaged across multiple datasets. The relationship between noise level and number of averages (N) is

close to $N^{-1/2}$. However, the noise level in the brain is about 5 times larger than that measured in the phantom. The difference may be attributed to physiological noise, cardiac action and motion, all of which do not influence phantom measurements.

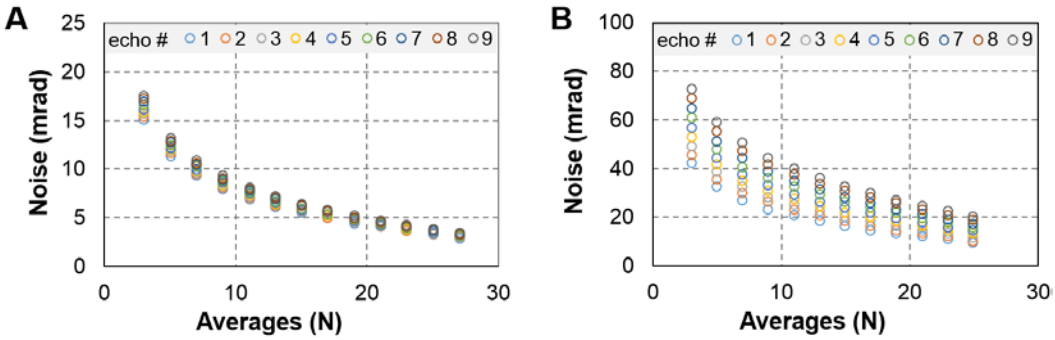

Figure 6-7 Dependence of phase noise level on number of averages for the phantom and the human brain.

The figure shows the phase noise level at echo times calculated with different number of averages for the phantom (A) and the human brain (B). Only results for the 3.4 µl voxel volume.

6.5 Experiment 3: phase noise due to motion

The subject's motion relative to the scanner has been reported to be a dominant source of phase noise in MRI signals (Hagberg et al., 2008; Brainovich et al., 2009; Petridou et al., 2009; Hagberg et al., 2012). Motion may be caused by physiological processes, such as respiration and cardiac action, and scanner vibration. In this experiment, I aimed to assess the effects of the subject's motion on signal phase noise. Two motion reduction methods have been tested: temporarily turning off the helium pump off to reduce scanner vibration, and restraining the subject's head motion using a head holder. The hypothesis was that signal phase noise can be reduced by minimising the subject head motion.

6.5.1 Materials and methods

The experiment used the same scanner, subject and phantom as provided under Experiment 1.

Motion control: To minimize head motion, a head holder was built for the subject using the 3D printing technique. The inner surface of the head holder was reconstructed from a 3D high resolution T_1-weighted MRI image of the subjects' head. The T_1-weighted image was acquired using a Siemens MAGNETOM TRIO 3T human scanner located at the Centre of Advanced Imaging with 1 mm isotropic resolution. The 3D model of the head holder was

created using the following steps. The subject's scalp was first manually segmented on the T_1-weighted image using the software Medical Imaging Interaction Toolkit (MITK, www.mitk.org). Then, a 3D model of the subject's scalp was generated from the segmented images, and digitized using the software Leios 2 (EGS, www.egsolutions.com). Based on the digitized scalp model, a head holder was created using the software Solid Edge ST6 (Siemens, www.plm.automation.siemens.com). The head holder was manufactured using the 3D printing service provided by the School of Information Technology and Electrical Engineering at the University of Queensland. The design of the head holder is shown in Figure 6-8.

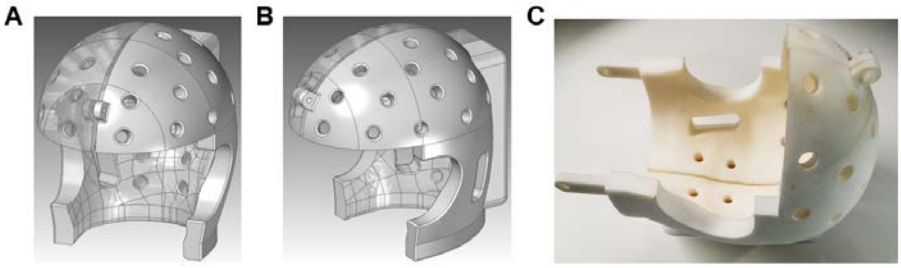

Figure 6-8 A head holder designed for nc-MRI experiment.

Shown are two views of a head holder design (A and B) and the 3D printed head holder (C). The head holder consists of two parts. The inner surface of the head holder fitted the shape of the subject's head, which was extracted from a 3D anatomical MRI image. The protrusion on the back of the head holder was inserted into the head coil of the scanner to fixing purposes.

Data collection: MRI data were collected using the same sequence and parameter settings as described above for Experiment 1. Three experimental setups were tested: (1) the helium pump on and no head holder used; (2) the helium pump off and no head holder used; and (3) the helium pump off and the head holder used. Twenty datasets were collected for each condition. For comparison, the phantom was also scanned using the same sequence and parameter settings. The phase noise of both the phantom images and the brain images were calculated and reported.

Image processing: Raw MRI signals were processed using the linear regression temporal correction pipeline provided under Experiment 1. A two-sample voxel-by-voxel *t*-test, as implemented in , as implemented in MATLAB 2014b, was used to test the phase noise difference between MRI images acquired under different conditions. The two samples of the *t*-test comprised the noise of individual voxels in corresponding regions of the images

acquired under two experiment conditions. Statistical significance was assessed at $p<0.05$ and $p<0.001$.

6.5.2 Results and discussion

Figure 6-9 displays the signal phase noise measured under the three experimental conditions. I found that turning off the helium pump slightly reduced the phase noise by about 2% in the phantom, but it did not affect the phase noise in the brain. The phantom data suggest that the operation of helium pump causes small vibrations in the scanner, which produce extra noise in measured signal phase that is reduced by turning off the pump. For the subject, however, respiration and cardiac actions produce more significant head motion overshadowing any effect from the helium pump so that no significant noise reduction was observed with turning the pump off.

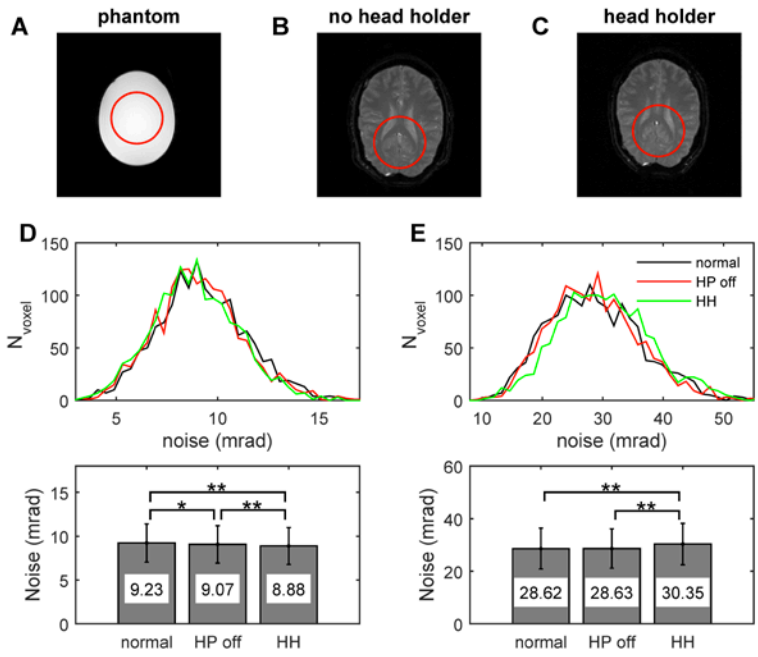

Figure 6-9 Effects of the head holder and helium pump on the noise level in measured MRI signal phase.

Shown are the magnitude images for (A) the phantom, (B) the brain without head holder, and (C) the brain with a head holder, and histograms of the phase noise in (D) the phantom images and (E) the brain images under different experimental conditions, and the mean values of the phase noise in (F) the phantom images and (G) the brain images. The error bar in (F) and (G) shows the standard deviations of the phase noise across the regions. The coloured lines in (D) and (E) represent the phase noise in MRI signals acquired under different conditions: black – helium pump on; red – helium pump off; green – helium pump off and head holder used. The red circle in (A-C) indicates the region used for phase noise comparisons. In (F) and (G), the numbers on the bar shows the mean phase noise level, and the stars represent the significance level of a t-test between the phase noises: * $p<0.05$, ** $p<0.001$. Data shown here are for the images acquired at TE = 40 msec.

Furthermore, I found that the use of head holder further reduced the noise in the phantom by about 2%, but it increased the phase noise in the brain by about 6% (see Figure 6-9). The phase noise reduction in the phantom is likely because the head holder may reduce the motion of the phantom by physically stabilizing it. The head holder was designed to allow firm attachment to the head coil, and the phantom was firmly fixed inside the head holder. Since the same head holder was used for the phantom and the brain experiments, the phase noise increase in the brain is unlikely caused by the head holder itself. The extra phase noise may be caused by temperature increase around the brain, which is caused by heat accumulated inside the head holder. The temperature increase may cause extra thermal noise in MRI signal magnitude and phase. The increased temperature may also increase the blood flow inside the brain, which may also produce noise in MRI signal magnitude and phase (Wang et al., 2014). In light of these results, the head holder was not used in Experiments 4 and 5.

6.6 Experiment 4: detecting NMF induced phase changes using MESE sequence

In this experiment I tested the potential to detect nc-MRI signal using the MESE sequence. Intermittent light stimulation at 15 Hz was used to evoke synchronised neuronal activity in the visual cortex. Functional MRI experiments were conducted to image the BOLD response, and nc-MRI experiments using the MESE sequence were conducted. The hypotheses were that (1) NMFs produce observable changes in MESE phase images; and (2) the presence of NMFs increase signal phase variations because NMFs produce positive or negative signal phase changes depending on the start of the scan relative to the oscillation periods of the stimulus (refer to Section 6.2).

6.6.1 Materials and methods

MRI scanner: A Siemens MAGNETOM TRIO 3T MRI human scanner was used to collect data for this experiment. The higher imaging field strength was used for the experiments on the basis that compared to 1.5T the SNR would be higher at the long TEs as used in MESE sequence. Ethics approval was obtain from the Human Research Ethics Committee of The University of Queensland. MRI data were collected using a Siemens 32-channel head coil.

Subject: A healthy 31 year old male subject with normal vision was scanned for this experiment.

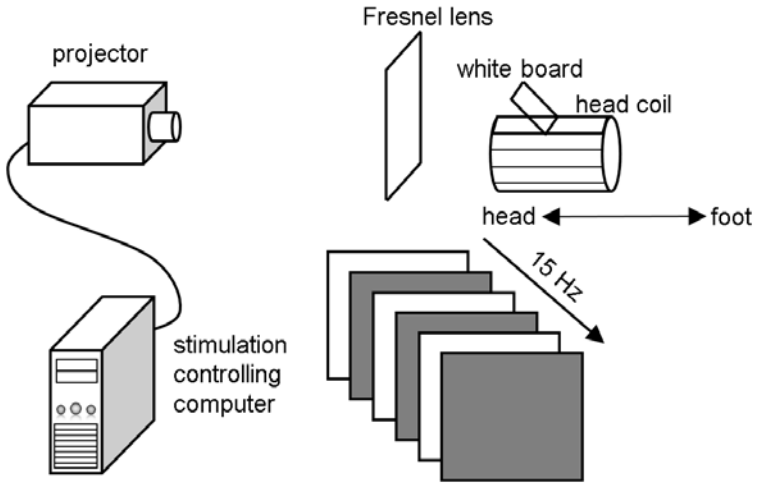

Figure 6-10 Stimulation system used for the nc-MRI experiment on the 3T scanner.

Shown is the configuration of the stimulation system, in which the stimulation controlling computer delivered accurately-timed white and black frames to the projector, the light from which was then focused by a Fresnel lens onto a white board that is fixed to the head coil.

Visual stimulation: The visual stimulation for the functional MRI and nc-MRI experiments consisted of alternating black and white screens. Each cycle of the stimulus lasted 66.6 msec comprising a 33.3 msec white screen followed by a 33.3 msec black screen. This corresponded to a frequency of 15 Hz with a 50% duty cycle. The stimuli were generated using a computer and presented with an MRI-compatible projector. The projector had a refresh rate of 60 Hz. To increase the stimulation strength inside the scanner, a 24 by 36 cm Fresnel lens with a focus of 50 cm was used to focus the light from the projector onto a 5 cm by 14 cm white board fixed to the head coil. The white board was adjusted to be at a distance of about 10 cm away from the subject's eyes. Figure 6-10 illustrates the experimental setup. The stimuli were started manually before MRI scans, and the onset times of the stimulus cycles were recorded for analysis. The average time difference between the onset of stimulus and MRI scan was about 8 sec. EEG recording was performed in the scanner separately to confirm the presence of steady state visual evoked potentials (SSVEPs) in the visual cortex of the subject during stimulation.

Data collection: Three types of MRI data were acquired: 3D whole brain T_1-weighted images, functional MRI images, and nc-MRI images. The T_1-weighted images were acquired using an inversion-recovery GRE sequence to help localise the primary visual

cortex of the subject. Five contiguous slices were set across the visual cortex aligned with the calcarine sulcus of the subject for both the functional MRI and nc-MRI data acquisition. Functional MRI data were acquired using a GE-EPI sequence with the following parameters: the flip angle was 80 degree; the TE was 30 msec; the TR was 1.5 sec; the in-plane resolution was 1.64 by 1.64 mm^2 (the image matrix was 128 by 128) with a slice thickness = 2.00 mm. A total of 380 fMRI datasets were collected, consisting of one half with and the other half without visual stimulation. Neuronal current images were acquired using a MESE sequence using parameter settings as follows: three TEs of 33.3, 66.6, and 99.9 msec were used; the TR was 1 sec; and the resolution was the same as the functional MRI data. The TEs were derived to match the oscillation period of the stimulus. A total of 32 datasets were acquired for the nc-MRI experiment consisting of one half with and one half without visual stimulation. The stimulated and non-stimulated datasets were acquired in an alternating fashion.

Image processing: For the fMRI data, a two-sample voxel-by-voxel *t*-test, as implemented in MATLAB 2014b, between the stimulated and non-stimulated data was used to map the activated regions. Activated voxels were identified with a p-value threshold of $p<0.0001$.

For the nc-MRI data, raw k-space data was downloaded from the scanner and used to reconstructed complex images, because the phase images were not collected in the scanner. The phase images were processed using the high-pass spatial filtering pipeline as provided under Experiment 1. The linear regression temporal correction method was not applied because signal phases were acquired at only three echo times, which were not sufficient for using the temporal correction method. A voxel-by-voxel two-sample *t*-test was used to compare the phases and magnitudes between stimulated and non-stimulated MESE signals, and a voxel-by-voxel two-sample *F*-test was used to compare the phase variations between the stimulated and non-stimulated signals. The alternative hypothesis of the *F*-test was that the stimulated signals have greater phase variations than the non-stimulated signals. The p-values of the *t*-test and *F*-test were calculated and reported.

6.6.2 Results and discussion

Figure 6-11 shows the activation map obtained from the functional MRI data. As expected, clear activation regions were present in the visual cortex across all the five slices. Strong activations were observed in the occipital cortex, at the calcarine sulcus.

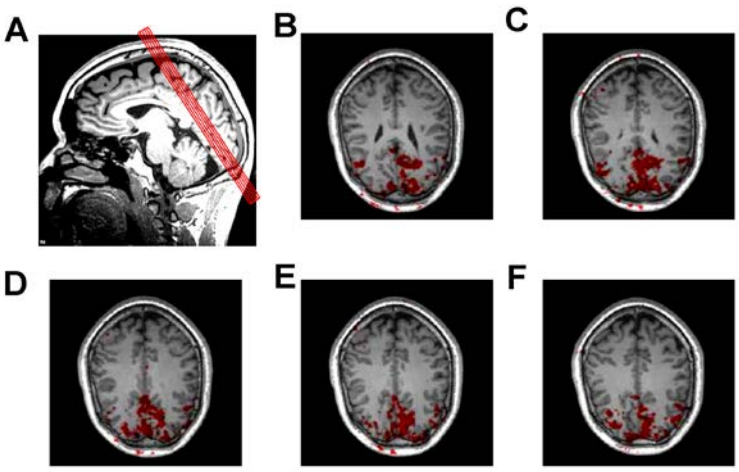

Figure 6-11 The activation map identified by functional MRI.

Shown are (A) the positioning of the five slices imaged with both the fMRI and neuronal current sequences, and (B-F) activation maps across slices identified via the fMRI analysis. In (A) the left lower slice is slice one, and the right upper slice is slice five. Slice 3 is positioned to across the calcarine sulcus. As per standard imaging, the right hemisphere of the brain is on the left-hand-side in the images.

In Figure 6-12, I show the magnitudes and phases of the stimulated and non-stimulated MESE images. Both the non-stimulated and stimulated data had inhomogeneous signal phases across the brain, ranging from -20 mrad to 20 mrad. Such a large phase variation can easily overshadow possible signal phase changes due to NMFs. The phase variations are likely to be caused by the RF pulses, because RF pulses, i.e. B_1 fields, are usually not homogenous across a slice (Haacke et al., 1999). The inhomogeneous B_1 field produces inhomogeneous flip angles and lead to spatially varied signal phases.

Figure 6-13 displays the phase variations across repetitions of data acquisition for the stimulated and non-stimulated MESE images. The phase variation was significantly higher in the centre of the brain compared to other regions. This is likely to be caused by the lower SNR in the centre of the brain, being further far away from the head coil than more peripheral brain structures (Haacke et al., 1999). The only region with an increase in phase variation with visual stimulation was a small region lying in a cortical region that also showed a significant increase in BOLD signal with visual stimulation (see Figure 6-13). It is possible that the increased phase variation is an effect of NMFs. However, further experiments are required to investigate the phenomenon further given that the change was highly localised.

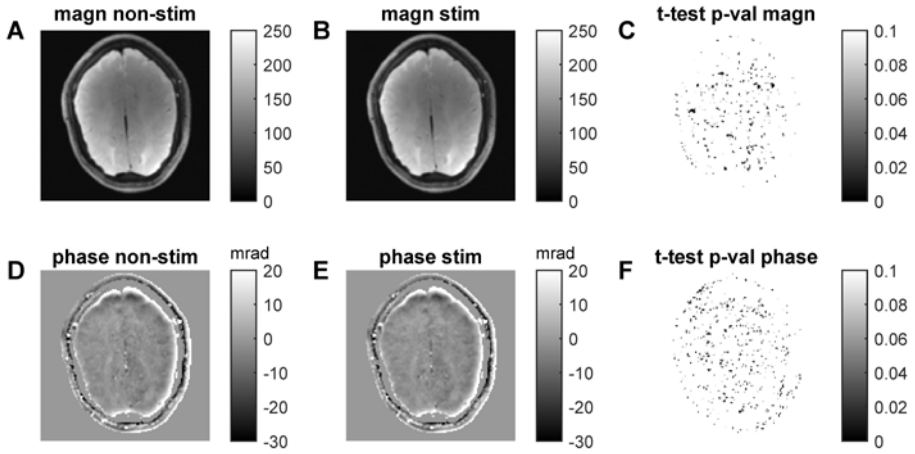

Figure 6-12 Signal magnitude and phase of the MESE images.

Shown are the magnitudes of the (A) non-stimulated and (B) stimulated MESE images, the phases of the non-stimulated (D) and stimulated (E) MESE images, and the *t*-test p-values of the magnitudes (C) and phases (F) between the stimulated and non-stimulated signals. The magnitude and phase images were averaged across 16 datasets. For clarity, the background in the region outside the subject's head was removed in (C-F). The results were calculated from data of the second slice at the second echo.

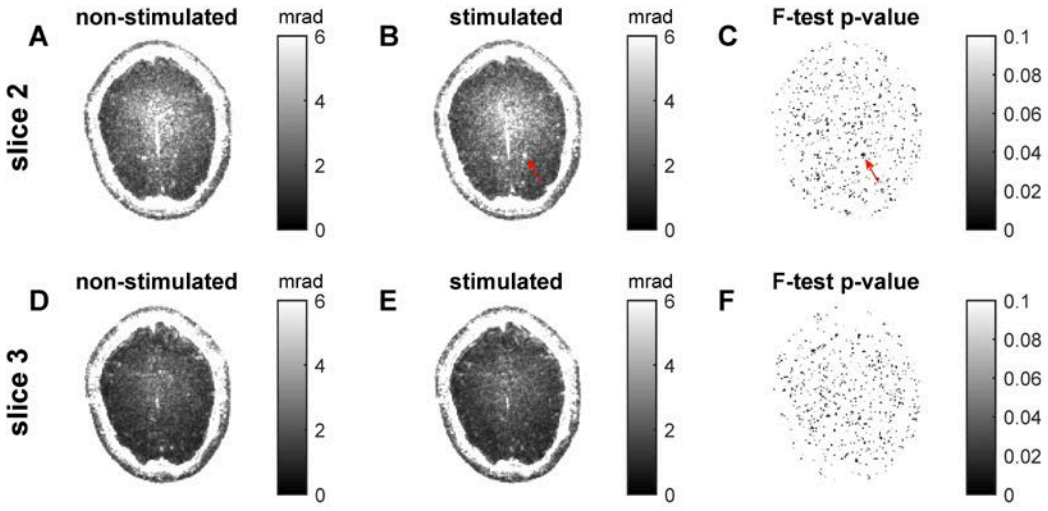

Figure 6-13 Phase variations of stimulated and non-stimulated MESE images.

Shown are the phase standard deviations over repetitions of data acquisitions for (A, D) non-stimulated and (B, C) stimulated images, and the *F*-test p-values of signal phases between the stimulated and non-stimulated signals (C, F) for slice 2 (A-C) and 3 (D-F).

6.7 Experiment 5: detecting NMF induced phase changes using MEGRE sequence

In this experiment I tested the potential to detect nc-MRI signal using the MEGRE sequence. As in Experiment 4, intermittent visual stimulation was used to evoke

synchronised neuronal activity in the visual cortex of two subjects. MRI scans were synchronised with the intermittent stimulation by matching the stimulus phase to a fixed time at the beginning of MRI scans. Two stimulation methods, in which MRI scans were synchronised to phases in the stimulus cycle were tested. The hypothesis tested was that nc-MRI signals can be obtained by comparing the MRI phase data acquired from different parts of the stimulus cycle because my simulations predicted that nc-MRI signal should oscillate with the stimulus cycle.

6.7.1 Materials and methods

MRI scanner: The experiment used the same MRI system as Experiment 1.

Subjects: Two adult male volunteers aged 31 and 48 years with normal vision were scanned for the experiment. EEG experiments were performed to confirm the presence of SSVEPs in both subjects under intermittent visual stimulation.

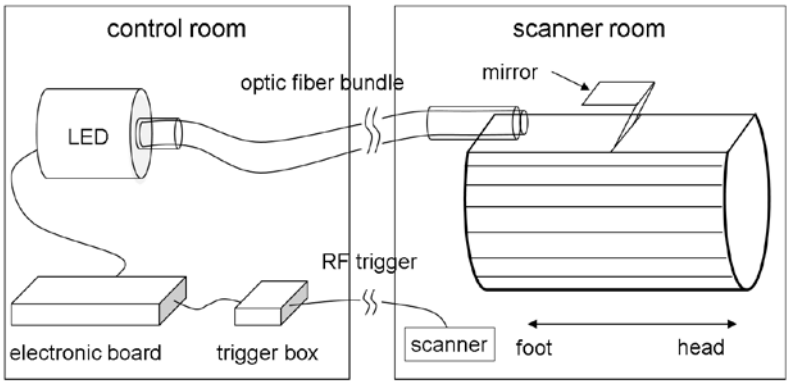

Figure 6-14 The MRI-compatible strobe light system used with the 1.5T scanner.

The system consisted of an electronic system placed in the control room, which was used to generate intermittent light stimulation for the subject, and optic fibres to deliver the stimulus into the scanner.

Visual stimulation: An MRI-compatible strobe light system was developed to generate intermittent light stimulation for the MEGRE experiments (see Figure 6-14 and Appendix D). Visual stimulation consisted of 20 Hz intermittent light with a duty cycle of 40% (i.e. 20 ms light on followed by 30 ms light off). The 40% duty cycle was used because it has been reported to be the most effective duty cycle for inducing fundamental SSVEP harmonics (Wu, 2009). The intermittent light was turned on for at least 8 seconds before the scan started to saturate the BOLD signal. To enable images from different nc-MRI acquisitions

to be averaged, the intermittent light stimulation was synchronised with the first RF pulse of each scan (see Figure 6-15).

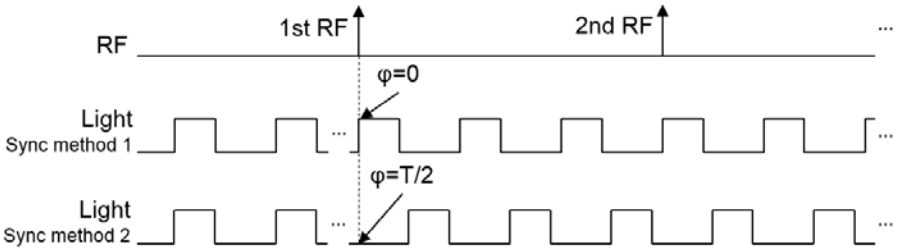

Figure 6-15. The stimulation mechanisms used in the MEGRE nc-MRI experiment.

The intermittent light was synchronised with the first RF pulse of a scan at phase φ=0 for method 1, and at phase φ=T/2 for method 2.

To distinguish nc-MRI signal from other effects on signal phase, two synchronisation methods were used: (1) upon receiving the RF pulse trigger, the intermittent light stimulation was set to the beginning of an oscillation period (i.e. beginning of the light on session, $\varphi = 0$); (2) upon receiving the RF pulse trigger, the intermittent light stimulation was set to the middle of an oscillation period (i.e. 10 ms after the light on session, $\varphi = T / 2$). This is illustrated in Figure 6-15.

Four stimulation conditions were studied: (S1) the subject's eyes were closed for the entire scan and visual stimulus not presented; (S2) the subject's eyes were open for the entire scan and a constant light was presented; (S3) the subject's eyes were open and 20 Hz flashing light was presented synchronised at $\varphi = 0$; and (S4) the subject's eyes were open and 20 Hz flashing light was presented synchronised at $\varphi = T / 2$. To deal with the delay in brain responses to visual stimulation (approximately 100 msec), data from the first slice was excluded from the analysis.

Data collection: A MEGRE sequence with the following parameter settings was used: the flip angle was 25 degree; ten TEs from 5 msec to 50 msec in the step of 5 msec were used; the TR was 200 msec; and the receiver bandwidth was set to 250 Hz/pixel. To minimise phase noise, a low resolution of 4 by 4 by 4 mm voxel (i.e. voxel volume of 64 μl) was used. Four slices across the visual cortex aligned with calcarine sulcus were used for data collection. 16 datasets were collected for each experimental condition.

Image processing: The images were analysed using the following steps. First, for all datasets, the phase time course of each voxel was processed using the linear regression

temporal correction pipeline, as described above for Experiment 1. Corresponding signal phase images of each condition (i.e. S1, S2, S3 and S4) were then averaged. Second, the temporal signal phase changes of different stimulation conditions were compared. I calculated the correlation coefficient between different pairs of conditions. Because in a oscillation cycle the synchronisation position of stimulus S4 was delayed by 25 ms in comparison to S3, the first five signal phases acquired with stimulus S3 were moved to the end of the time course to match the periodicity of S4. In the following text, I refer to signal pairs with the above adjustment as the *stimulation matched signals,* and the signal pairs without the adjustment as *TE matched signals*. The phases of stimulation matched signals were acquired at the same points relative to the stimulation oscillation cycles, and the phases of TE matched signals were acquired at the same TEs. Signal change due to neuronal current should increase the correlation between stimulation matched signals but not TE matched signals.

6.7.2 Results and discussion

Figure 6-16 displays the averaged phase time courses of three typical voxels to illustrate the temporal behaviour of MEGRE signal phases captured in the data. The phase time courses after temporal correction still displayed similar temporal shapes, and the shapes vary from voxel to voxel. This indicates that a common phase component with non-linear temporal behaviour is present under all stimulation methods. The component is likely to be caused by effects related to the properties of the brain tissue in individual voxels, such as eddy currents. To highlight the difference between the phase time courses, I used the phases acquired under constant light stimulation as a baseline, and subtracted it from other phase time courses (see Figure 6-16). The resultant phase time courses were used for the calculation of the correlation coefficient.

Figure 6-17 displays the correlation coefficient maps between signal phases acquired under different conditions for the two subjects, and Figure 6-18 displays the mean correlation coefficients of a region in the visual cortex and two regions outside the visual cortex. First of all, for all stimulation conditions, strong positive correlations were observed between the TE matched signals, and strong negative correlations were observed between the stimulation matched signals. The positive correlation between TE matched signals suggests that the signal phase evolution is influenced by effects independent from

stimulation that outweigh effects due to neuronal currents. These effects are likely to be caused by the interactions between imaging components (i.e. imaging fields and field gradients) and brain tissues. The negative correlation between stimulation matched signals is likely caused by the signal phase adjustment process. Secondly, I found that the phase correlations in the visual cortex were weaker than outside the visual cortex. This could be due to signal phase evolution in the visual cortex being influenced by effects related to neuronal activity during visual stimulation, which are absent from other brain regions. These effects could include BOLD response and diffusion effects (Le Bihan et al., 2006). In the visual cortex but not in other brain regions, the correlation between signal phases of S3 and S4 was consistently stronger than the correlation between those of S1 and S3. This is a possible indicator of a neuronal current signal, however the differences were not statistically significant and further refinement and experimental evaluation is required.

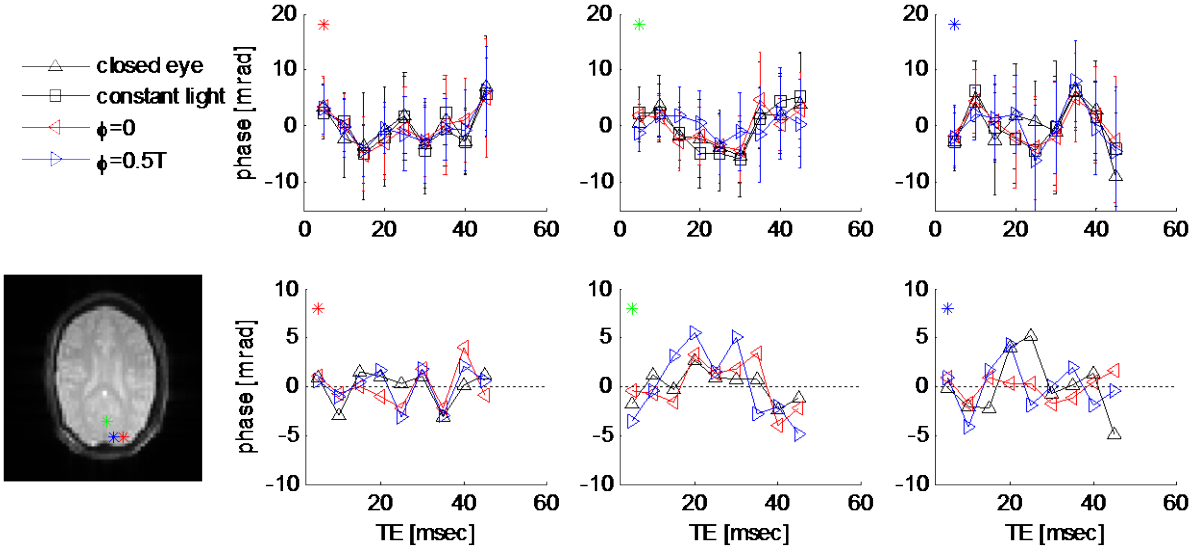

Figure 6-16 Typical signal phase time courses acquired using the MEGRE sequence.

Shown are signal phase time courses of three typical voxels under the four stimulation methods. The upper panel displays the original signal phases, and the phases shown in the lower panel are subtracted by a baseline, which is the phases acquired with the constant light stimulation. The coloured lines and markers indicate images acquired the four different conditions: S1 - closed eye, S2 – constant light, S3 – intermittent light stimulation with φ=0 and S4 – intermittent light stimulation with φ=T/2. Voxel locations are indicated on the magnitude image. Each time course is averaged across 16 datasets, and the error bars display the standard deviation of signal phases.

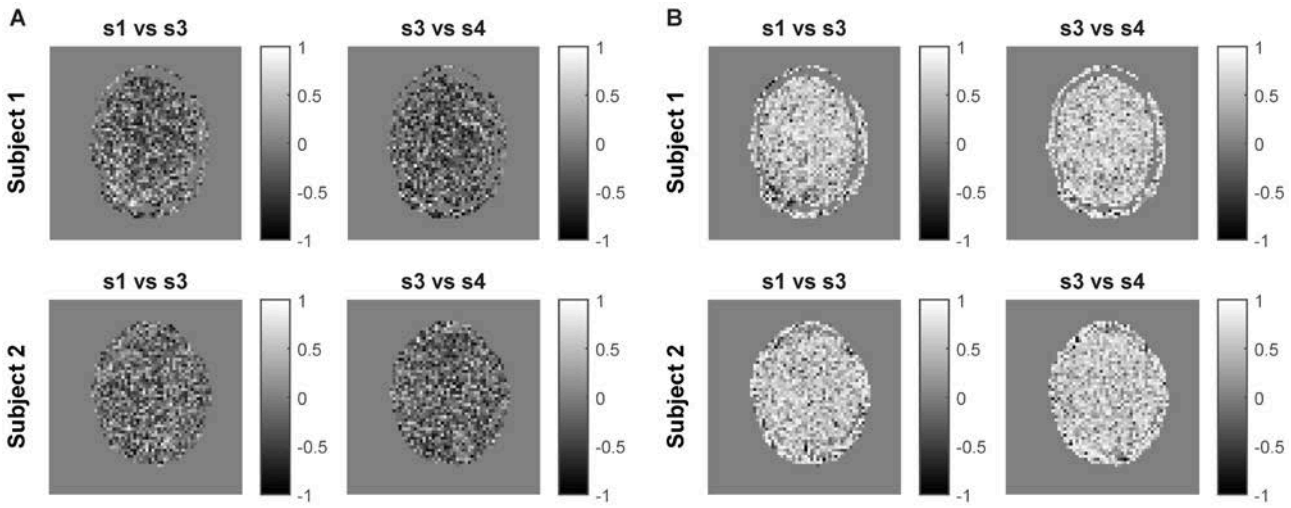

Figure 6-17 Spearman's rank correlation coefficient between signal phase time courses acquired across different conditions.

The figure displays the correlation coefficient maps between phase time courses acquired with S1 and S3, and between S3 and S4 for the two subjects. The correlation coefficient shown in (A) was calculated using stimulation matched phase time courses (see text for more information), and the correlation coefficient in (B) was calculated with TE matched phase time courses.

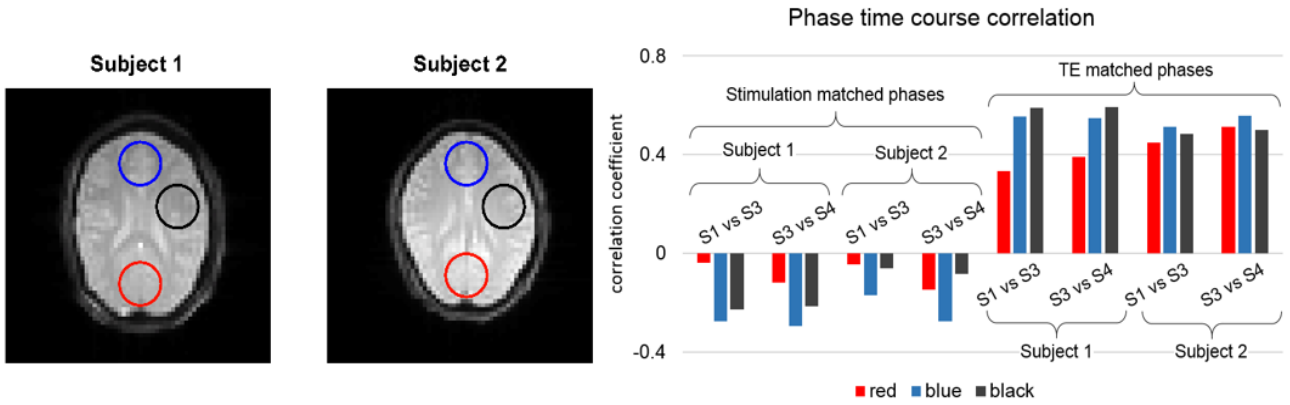

Figure 6-18 Correlation between phase time courses in different brain regions.

The figure displays the mean correlation coefficient values of a region in the visual cortex (red circle) and two regions outside the visual cortex (blue and black circle) for the two subjects.

6.8 Conclusions

In this Chapter, I describe the MRI experiments that I conducted to test the potential to detect nc-MRI signal. I observed that the noise level was much larger than the expected neuronal current-induced changes. My computer simulations suggest neuronal currents produce NMFs in the order of 100 pT (refer to Chapter 5), which can change MRI signal

phase by about 1 mrad. In my experiments, however, I found the phase noise in MEGRE images is about 100 mrad for 3.4 μl voxels, about 30 mrad for 9.4 μl voxels, and about 10 mrad for 64 μl voxels, which is one to two orders of magnitude larger than the predicted neuronal current signal. The phase noise in MESE images is about 5 mrad for 5.4 μl voxels, which is also several times larger than the predicted neuronal current signal. Lower phase noise level can be achieved by using larger voxels. However, this may not be helpful for nc-MRI experiments, because neuronal current-induced phase change is expected to be smaller in large voxels (refer to Chapter 5). Hence, a better noise suppression method is required for future nc-MRI experiments.

Essentially, the signal phase is a fingerprint of the magnetic field shift averaged over both the voxel volume and the echo time. Any factors that cause fluctuations in the local magnetic fields can introduce noise in phase images. Hagberg et al. (2012) identified two major sources of phase noise: scanner instability and the subject's motion relative to the scanner. The thermal fluctuation and instability of the electronics of the scanner can cause time-dependent variations in the imaging field B_0 and in the gradient fields, which may directly alter the magnetic fields within voxels and produce troublesome noise in phase images. Another type of noise source is the subject's motion relative to the scanner, which may be caused by scanner vibration, respiration, the ballistocardiogram, and movement by the subject. Effectively, the motion shifts voxel locations relative to the imaging volume. The shift changes the local magnetic fields of voxels, resulting in a change in MRI signal phase. Continuous and non-linear motion and vibrations in the presence of field gradients result in noise MRI signal phase. Previous studies (Petridou et al., 2009; Hagberg et al., 2012) showed that the noise originating from vibration due the helium pump and respiration-related and cardiac motion are the dominant sources of noise. In my experiment, the signal phase noise of brain data is 2-3 times larger than that of phantom data, indicating that the contribution of motion to signal phase noise is larger than that of scanner-related instability and vibration.

Several methods may be used to suppress phase noise. First of all, a short scan time is preferred for nc-MRI experiments, because motion-related phase noise accumulates with time. For example, in the MEGRE experiments, the phase noise at the ninth echo (TE = 45 msec) is about 50% higher than that at the first echo (TE = 5 msec) in the phantom, and the difference is more than 100% for the brain images. In light of this, fast-acquisition

sequences, such as the EPI technique, may be more useful for nc-MRI experiments. In a SE and GRE sequence, phase noise can accumulate between the excitation RF pulse and the echo in all repetitions, therefore the total phase noise accumulation time is $N_{TR} \times TE$ where N_{TR} is the repetition time, i.e. the number of phase encoding lines. However, the EPI sequence can acquire an image in one or a few shots, in turn reducing sequence repetition times, and potentially reducing the time over which phase noise can accumulate. Secondly, besides head movement restriction methods, electrocardiogram (ECG) gating techniques may also be useful to minimize motion-induced phase noise. Triggering MRI scans using ECG signal enables the acquisition of MRI data at the same time in the cardiac cycle, which may help to reduce the phase noise related to the ballistocardiogram. Furthermore, the motion may be corrected using prospective motion correction, which can maintain a constant spatial relationship between the imaged subject and the imaging volume of the scanner (Maclaren et al., 2013). This has been achieved by accurate tracking of the subject motion and by adjusting the MRI pulse sequence accordingly, such that the imaging volume adjusts to the subject (Maclaren et al., 2013).

Nc-MRI signal may be revealed by correlative analysis of the MRI signals in adjacent voxels. This strategy has the theoretical advantage that nc-MRI signals of adjacent voxels are likely to be correlated because NMFs have no curl (refer to Chapter 5). Non-parametric cluster-based analysis methods (see, for example, Heller et al., 2006) could be adapted for this analysis. Existing cluster-based analysis methods have been developed for fMRI data analysis, and may require modification to be applicable to nc-MRI data. Unlike fMRI in which neural activation results in an increase in signal magnitude, nc-MRI signals can present either as an increase or a decrease in signal phase. Hence, whereas an fMRI signal cluster is identified as adjacent voxels showing increased signal magnitude, a nc-MRI signal cluster may contain both positive phase change and negative signal phase change, with the phase changes being constrained by the Biot-Savart law (refer to Chapter 5). Development of such a method is an important direction for future work.

I studied signal phase changes related to visual stimulation using a synchronised MESE sequence and a synchronised MESE sequence. Although I observed suggestive changes described in the results, I did not observe significant phase changes at the level of 1 mrad predicted by my simulations because of the extent of noise in signal phase. The

noise in signal phase has to be suppressed by at least two orders of magnitude before the neuronal current induced signal phase change can be reliably deduced.

Chapter 7

Summary and Future Work

I developed a laminar cortex model to simulate the neuronal activity of the primary visual cortex. I have used the model to study the neuronal currents and predicted nc-MRI signal associated with different neuronal oscillatory states, at different levels of neuronal activity in the primary visual cortex. I performed MRI experiments to examine the potentials of detecting the neuronal current signals using multi-echo spin echo (MESE) and multi-echo gradient recalled echo (MEGRE) sequence. Based on the simulation and experimental results, I have been able to answer the following research questions:

1. Is neuronal current detectable using present MRI techniques?

   Neuronal currents produce a potentially detectable phase change and a negligible MRI signal magnitude change. The signal magnitude change is orders of magnitude below the detectable level, but the signal phase change is close to the sensitive of current MRI instrument.

2. How is neuronal current MRI signal related to neuronal activity?

   I found that neuronal current signals are determined by the temporal and spatial variation of neuronal activities. Therefore, large signal changes are likely to be produced by oscillating neuronal activity at boundaries of the activated region.

3. What MRI protocol should be used to detect neuronal current signal?

   I proposed to image neuronal currents using synchronised MESE sequence or synchronised MEGRE sequence. The MESE sequence has the potential to enhance the neuronal signal while suppressing phase changes produced by saturated BOLD response and other effects. MEGRE may be used to extract neuronal current signal from noisy MRI signals. However, the noise level in the signal phase is about 10-100 times larger than the phase change of neuronal

currents. An effective noise suppression method is required for future nc-MRI experiments.

The ultimate goal of the project was to aid the development of MRI protocols that can reliably measure neuronal currents. Following on from my experiments, future nc-MRI experiments need to deal with two challenges: further suppressing noise in MRI signal phase, and separating neuronal current signal from changes due to other effects, especially BOLD response. My experiments described in Chapter 6 suggest noise in MRI signal phase may be partly removed through optimizing the image processing pipeline. The experiments also suggest that though motions can cause noise in signal phase, physically stabilizing the subject's head may not help to reduce phase noise. Further nc-MRI experiment should seek other approaches for phase noise reduction. Furthermore, nc-MRI signal may be separated from changes caused by other effects based on its temporal characteristics. Several methods were introduced and implemented in Chapter 6. However, these methods may only be effective if a significantly higher SNR level can be achieved.

To aid future nc-MRI experiment design, computer simulation may be used to study MRI signal phases in the presence of motion. Such a model can be used to study the noises produced by scanner vibration, subject respiration and cardiac actions, and subject voluntary motions. It may also be used to predict the upper limits of motions allowed for detecting the signal phase changes produced by neuronal currents. These predictions can help design MRI experiments to avoid the major source of noise in signal phase, and develop noise removal methods applicable to phase-based imaging.

Theoretically the neuronal current signals are independent of the imaging field strength, but the noises encountered in phase imaging is imaging field strength dependent (Raj et al., 2000). Therefore, it is necessary to investigate the signal-to-noise ratio of phase images across a range of field strengths. The outcome of such a study may help with the choice MRI scanner field strength for nc-MRI experiments.

While the project has provided insight into MRI-based neuronal current imaging, it may continue to benefit the research through the following works.

Firstly, the LCM developed as part of this research project may be used to simulate abnormal responses to intermittent light stimulation such as the photoparoxysmal

response observed in forms of genetic generalized epilepsy. This can be achieved by varying LCM parameters, and by comparing the simulation output with measured EEG data. This has the potential to generate testable hypotheses relating to underlying neurophysiological mechanisms.

Secondly, I developed a framework to simulate NMFs produced by various types of neuronal activity. This framework is not only useful for pre-experiment testing of nc-MRI protocols, it can provide also an effective way to study the neuronal basis of MEG signals. It is possible that the model can be expanded to simulate the NMFs produced not in just a specific brain region, but across the entire brain. The outcome of which may be a useful in solving the signal-to-source inverse problem faced in MEG.

Bibliography

Andersen P., Andersson S.A. (1968) Physiological basis of the alpha rhythm. New York: Appleton-Century-Crofts.

Arthurs O.J., Boniface S. (2002) How well do we understand the neural origins of the fMRI BOLD signal? *Trends Neurosci* 25:27-31.

Bak P., Tang C., Wiesenfeld K. (1987) Self-organized criticality: An explanation of the 1/f noise. *Phys Rev Lett* 59:381-384.

Bak P., Tang C., Wiesenfeld K. (1988) Self-organized criticality. *Phys Rev A* 38:364-374.

Bandettini P.A., Petridou N., Bodurka J. (2005) Direct detection of neuronal activity with MRI: Fantasy, possibility, or reality? *Appl Magn Reson* 29:65-88.

Beaulieu C., Colonnier M. (1983) The number of neurons in the different laminae of the binocular and monocular regions of area 17 in the cat, Canada. *J Comp Neurol* 217:337-344.

Bedard C., Destexhe A. (2009) Macroscopic models of local field potentials and the apparent 1/f noise in brain activity. *Biophys J* 96:2589-2603.

Belluscio M.A., Mizuseki K., Schmidt R., Kempter R., Buzsaki G. (2012) Cross-frequency phase-phase coupling between theta and gamma oscillations in the hippocampus. *J Neurosci* 32:423-435.

Berens P., Logothetis N.K., Tolias A.S. (2010) Local field potentials, BOLD and spiking activity -- relationships and physiological mechanisms. In: Visual Population Codes: Toward a Common Multivariate Framework for Cell Recording and Functional Imaging (Kriegeskorte N, Kreiman G, eds), pp 599-623. Cambridge: MIT Press.

Bernstein M.A., King K.F., Zhou Z.J. (2004) Handbook of MRI pulse sequences. Amsterdam ; Boston: Academic Press.

Bianciardi M., Di Russo F., Aprile T., Maraviglia B., Hagberg G.E. (2004) Combination of BOLD-fMRI and VEP recordings for spin-echo MRI detection of primary magnetic effects caused by neuronal currents. *Magn Reson Imaging* 22:1429-1440.

Binzegger T., Douglas R.J., Martin K.A. (2004) A quantitative map of the circuit of cat primary visual cortex. *J Neurosci* 24:8441-8453.

Biswal B., Yetkin F.Z., Haughton V.M., Hyde J.S. (1995) Functional Connectivity in the Motor Cortex of Resting Human Brain Using Echo-Planar Mri. *Magn Reson Med* 34:537-541.

Blagoev K.B., Mihaila B., Travis B.J., Alexandrov L.B., Bishop A.R., Ranken D., Posse S., Gasparovic C., Mayer A., Aine C.J., Ulbert I., Morita M., Muller W., Connor J., Halgren E. (2007) Modelling the magnetic signature of neuronal tissue. *NeuroImage* 37:137-148.

Blumcke I. et al. (2011) The clinicopathologic spectrum of focal cortical dysplasias: a consensus classification proposed by an ad hoc Task Force of the ILAE Diagnostic Methods Commission. *Epilepsia* 52:158-174.

Bodurka J., Bandettini P.A. (2002) Toward direct mapping of neuronal activity: MRI detection of ultraweak, transient magnetic field changes. *Magn Reson Med* 47:1052-1058.

Bodurka J., Jesmanowicz A., Hyde J.S., Xu H., Estkowski L., Li S.J. (1999) Current-induced magnetic resonance phase imaging. *J Magn Reson* 137:265-271.

Borthakur A., Hulvershorn J., Gualtieri E., Wheaton A.J., Charagundla S., Elliott M.A., Reddy R. (2006) A pulse sequence for rapid in vivo spin-locked MRI. *J Magn Reson Imaging* 23:591-596.

Brainovich V., Sabatini U., Hagberg G.E. (2009) Advantages of using multiple-echo image combination and asymmetric triangular phase masking in magnetic resonance venography at 3 T. *Magn Reson Imaging* 27:23-37.

Brenner D., Williamson S.J., Kaufman L. (1975) Visually evoked magnetic fields of the human brain. *Science* 190:480-482.

Buxton R.B. (2009) Introduction to functional magnetic resonance imaging : principles and techniques, 2nd Edition. Cambridge ; New York: Cambridge University Press.

Buzsaki G. (2002) Theta oscillations in the hippocampus. *Neuron* 33:325-340.

Buzsaki G., Draguhn A. (2004) Neuronal oscillations in cortical networks. *Science* 304:1926-1929.

Buzsaki G., Anastassiou C.A., Koch C. (2012) The origin of extracellular fields and currents--EEG, ECoG, LFP and spikes. *Nat Rev Neurosci* 13:407-420.

Carandini M., Ferster D. (2000) Membrane potential and firing rate in cat primary visual cortex. *J Neurosci* 20:470-484.

Cassara A.M., Hagberg G.E., Bianciardi M., Migliore M., Maraviglia B. (2008) Realistic simulations of neuronal activity: a contribution to the debate on direct detection of neuronal currents by MRI. *NeuroImage* 39:87-106.

Chatt A.B., Ebersole J.S. (1988) Comparisons between Strychnine and Penicillin Epileptogenesis Suggest That Propagating Epileptiform Abnormalities Require the Potentiation of Thalamocortical Circuitry in Neocortical Layer-4. *Exp Neurol* 100:365-380.

Chen Y., Seth A.K., Gally J.A., Edelman G.M. (2003) The power of human brain magnetoencephalographic signals can be modulated up or down by changes in an attentive visual task. *Proc Natl Acad Sci U S A* 100:3501-3506.

Chow L.S., Cook G.G., Whitby E., Paley M.N. (2006) Investigation of MR signal modulation due to magnetic fields from neuronal currents in the adult human optic nerve and visual cortex. *Magn Reson Imaging* 24:681-691.

Chu R., de Zwart J.A., van Gelderen P., Fukunaga M., Kellman P., Holroyd T., Duyn J.H. (2004) Hunting for neuronal currents: absence of rapid MRI signal changes during visual-evoked response. *NeuroImage* 23:1059-1067.

Connors B.W., Gutnick M.J. (1990) Intrinsic firing patterns of diverse neocortical neurons. *Trends Neurosci* 13:99-104.

Dalal S.S., Baillet S., Adam C., Ducorps A., Schwartz D., Jerbi K., Bertrand O., Garnero L., Martinerie J., Lachaux J.P. (2009) Simultaneous MEG and intracranial EEG recordings during attentive reading. *NeuroImage* 45:1289-1304.

Darquie A., Poline J.B., Poupon C., Saint-Jalmes H., Le Bihan D. (2001) Transient decrease in water diffusion observed in human occipital cortex during visual stimulation. *Proc Natl Acad Sci U S A* 98:9391-9395.

Disbrow E.A., Slutsky D.A., Roberts T.P., Krubitzer L.A. (2000) Functional MRI at 1.5 tesla: a comparison of the blood oxygenation level-dependent signal and electrophysiology. *Proc Natl Acad Sci U S A* 97:9718-9723.

Drubach D. (2000) The brain explained. Upper Saddle River, NJ: Prentice Hall Health.

Du J., Vegh V., Reutens D.C. (2012a) The Laminar Cortex Model: A New Continuum Cortex Model Incorporating Laminar Architecture. *PLoS Comput Biol* 8:e1002733-e1002733.

Du J., Vegh V., Reutens D.C. (2012b) Cortical local field potential simulation using the laminar cortex model. *Society for Neuroscience Abstract Viewer and Itinerary Planner* 42.

Einevoll G.T., Kayser C., Logothetis N.K., Panzeri S. (2013) Modelling and analysis of local field potentials for studying the function of cortical circuits. *Nat Rev Neurosci* 14:770-785.

Einevoll G.T., Pettersen K.H., Devor A., Ulbert I., Halgren E., Dale A.M. (2007) Laminar population analysis: estimating firing rates and evoked synaptic activity from multielectrode recordings in rat barrel cortex. *J Neurophysiol* 97:2174-2190.

Freeman W.J., Rogers L.J., Holmes M.D., Silbergeld D.L. (2000) Spatial spectral analysis of human electrocorticograms including the alpha and gamma bands. *J Neurosci Methods* 95:111-121.

Haacke E.M., Brown R.W., Thompson M.R., Venkatesan R. (1999) Magnetic resonance imaging : physical principles and sequence design. New York: Wiley.

Hagberg G.E., Bianciardi M., Maraviglia B. (2006) Challenges for detection of neuronal currents by MRI. *Magn Reson Imaging* 24:483-493.

Hagberg G.E., Bianciardi M., Brainovich V., Cassara A.M., Maraviglia B. (2008) The effect of physiological noise in phase functional magnetic resonance imaging: from blood oxygen level-dependent effects to direct detection of neuronal currents. *Magn Reson Imaging* 26:1026-1040.

Hagberg G.E., Bianciardi M., Brainovich V., Cassara A.M., Maraviglia B. (2012) Phase stability in fMRI time series: effect of noise regression, off-resonance correction and spatial filtering techniques. *NeuroImage* 59:3748-3761.

Halpern-Manners N.W., Bajaj V.S., Teisseyre T.Z., Pines A. (2010) Magnetic resonance imaging of oscillating electrical currents. *Proc Natl Acad Sci U S A* 107:8519-8524.

Hamalainen M., Hari R., Ilmoniemi R.J., Knuutila J., Lounasmaa O.V. (1993) Magnetoencephalography - Theory, Instrumentation, and Applications to Noninvasive Studies of the Working Human Brain. *Rev Mod Phys* 65:413-497.

Handwerker D.A., Gonzalez-Castillo J., D'Esposito M., Bandettini P.A. (2012) The continuing challenge of understanding and modeling hemodynamic variation in fMRI. *NeuroImage* 62:1017-1023.

Hansen P.C., Kringelbach M.L., Salmelin R. (2010) MEG : an introduction to methods. New York: Oxford University Press.

Heller L., Barrowes B.E., George J.S. (2009) Modeling direct effects of neural current on MRI. *Hum Brain Mapp* 30:1-12.

Heller R., Stanley D., Yekutieli D., Rubin N., Benjamini Y. (2006) Cluster-based analysis of FMRI data. *NeuroImage* 33:599-608.

Henze D.A., Borhegyi Z., Csicsvari J., Mamiya A., Harris K.D., Buzsaki G. (2000) Intracellular features predicted by extracellular recordings in the hippocampus in vivo. *J Neurophysiol* 84:390-400.

Herrmann C.S. (2001) Human EEG responses to 1-100 Hz flicker: resonance phenomena in visual cortex and their potential correlation to cognitive phenomena. *Exp Brain Res* 137:346-353.

Hille B. (2001) Ion channels of excitable membranes, 3rd Edition. Sunderland, Massachusetts: Sinauer.

Hines M.L., Carnevale N.T. (1997) The NEURON simulation environment. *Neural Comput* 9:1179-1209.

Hirsch J.A., Gilbert C.D. (1991) Synaptic physiology of horizontal connections in the cat's visual cortex. *J Neurosci* 11:1800-1809.

Horton J.C., Adams D.L. (2005) The cortical column: a structure without a function. *Philos Trans R Soc Lond B Biol Sci* 360:837-862.

Huang Y.L., Xiong H.C., Yao D.Z. (2010) Direct MRI detection of the neuronal magnetic field: the effect of the dendrite branch. *Phys Med Biol* 55:5599-5616.

Huettel S.A., Song A.W., McCarthy G. (2009) Functional magnetic resonance imaging, 2nd Edition. Sunderland, Mass.: Sinauer Associates.

Izhikevich E.M., Edelman G.M. (2008) Large-scale model of mammalian thalamocortical systems. *Proc Natl Acad Sci U S A* 105:3593-3598.

Jay W.I., Wijesinghe R.S., Dolasinski B.D., Roth B.J. (2012) Is it possible to detect dendrite currents using presently available magnetic resonance imaging techniques? *Med Biol Eng Comput* 50:651-657.

Jin X., Huguenard J.R., Prince D.A. (2011) Reorganization of inhibitory synaptic circuits in rodent chronically injured epileptogenic neocortex. *Cereb Cortex* 21:1094-1104.

Johnston D., Wu S.M.-s. (1995) Foundations of cellular neurophysiology. Cambridge, Mass.: MIT Press.

Joy M., Scott G., Henkelman M. (1989) In vivo detection of applied electric currents by magnetic resonance imaging. *Magn Reson Imaging* 7:89-94.

Kajikawa Y., Schroeder C.E. (2011) How local is the local field potential? *Neuron* 72:847-858.

Kamei H., Iramina K., Yoshikawa K., Ueno S. (1999) Neuronal current distribution imaging using magnetic resonance. *IEEE Trans Magn* 35:4109-4111.

Kamondi A., Acsady L., Wang X.J., Buzsaki G. (1998) Theta oscillations in somata and dendrites of hippocampal pyramidal cells in vivo: activity-dependent phase-precession of action potentials. *Hippocampus* 8:244-261.

Kandel E.R., Schwartz J.H., Jessell T.M. (2000) Principles of neural science, 4th Edition. New York: McGraw-Hill, Health Professions Division.

Katzner S., Nauhaus I., Benucci A., Bonin V., Ringach D.L., Carandini M. (2009) Local origin of field potentials in visual cortex. *Neuron* 61:35-41.

Kim D.S., Ronen I., Olman C., Kim S.G., Ugurbil K., Toth L.J. (2004) Spatial relationship between neuronal activity and BOLD functional MRI. *NeuroImage* 21:876-885.

Kim Y.J., Grabowecky M., Paller K.A., Muthu K., Suzuki S. (2007) Attention induces synchronization-based response gain in steady-state visual evoked potentials. *Nat Neurosci* 10:117-125.

Kohn A. (2007) Visual adaptation: physiology, mechanisms, and functional benefits. *J Neurophysiol* 97:3155-3164.

Kole M.H., Ilschner S.U., Kampa B.M., Williams S.R., Ruben P.C., Stuart G.J. (2008) Action potential generation requires a high sodium channel density in the axon initial segment. *Nat Neurosci* 11:178-186.

Konn D., Gowland P., Bowtell R. (2003) MRI detection of weak magnetic fields due to an extended current dipole in a conducting sphere: a model for direct detection of neuronal currents in the brain. *Magn Reson Med* 50:40-49.

Konn D., Leach S., Gowland P., Bowtell R. (2004) Initial attempts at directly detecting alpha wave activity in the brain using MRI. *Magn Reson Imaging* 22:1413-1427.

Kraus R.H., Espy M.A., Volegov P.L., Matlachov A.N., Mosher J.C., Urbaitis A.V., Zotev V.S. (2007) Toward SQUID-Based Direct Measurement of Neural Currents by Nuclear Magnetic Resonance. *IEEE Trans Appl Supercond* 17:854-857.

Kraus R.H., Jr., Volegov P., Matlachov A., Espy M. (2008) Toward direct neural current imaging by resonant mechanisms at ultra-low field. *NeuroImage* 39:310-317.

Lai S., Hopkins A.L., Haacke E.M., Li D., Wasserman B.A., Buckley P., Friedman L., Meltzer H., Hedera P., Friedland R. (1993) Identification of vascular structures as a major source of signal contrast in high resolution 2D and 3D functional activation imaging of the motor cortex at 1.5T: preliminary results. *Magn Reson Med* 30:387-392.

Le Bihan D., Urayama S., Aso T., Hanakawa T., Fukuyama H. (2006) Direct and fast detection of neuronal activation in the human brain with diffusion MRI. *Proc Natl Acad Sci U S A* 103:8263-8268.

Lee A.T., Glover G.H., Meyer C.H. (1995) Discrimination of large venous vessels in time-course spiral blood-oxygen-level-dependent magnetic-resonance functional neuroimaging. *Magn Reson Med* 33:745-754.

Leemis L.M., Park S.K. (2006) Discrete-event simulation: a first course. Williamsburg, VA: Pearson Prentice Hall.

Liang Z.P., Lauterbur P.C. (2000) Principles of magnetic resonance imaging: a signal processing perspective. Piscataway, NJ: SPIE Optical Engineering Press.

Linden H., Pettersen K.H., Einevoll G.T. (2010) Intrinsic dendritic filtering gives low-pass power spectra of local field potentials. *J Comput Neurosci* 29:423-444.

Linden H., Tetzlaff T., Potjans T.C., Pettersen K.H., Grun S., Diesmann M., Einevoll G.T. (2011) Modeling the spatial reach of the LFP. *Neuron* 72:859-872.

Liston A.D., Salek-Haddadi A., Kiebel S.J., Hamandi K., Turner R., Lemieux L. (2004) The MR detection of neuronal depolarization during 3-Hz spike-and-wave complexes in generalized epilepsy. *Magn Reson Imaging* 22:1441-1444.

Logothetis N.K. (2002) The neural basis of the blood-oxygen-level-dependent functional magnetic resonance imaging signal. *Philos Trans R Soc Lond B Biol Sci* 357:1003-1037.

Logothetis N.K. (2003) The underpinnings of the BOLD functional magnetic resonance imaging signal. *J Neurosci* 23:3963-3971.

Logothetis N.K. (2008) What we can do and what we cannot do with fMRI. *Nature* 453:869-878.

Logothetis N.K., Pauls J., Augath M., Trinath T., Oeltermann A. (2001) Neurophysiological investigation of the basis of the fMRI signal. *Nature* 412:150-157.

Lother S., Hoelscher U., Kampf T., Jakob P., Fidler F. (2013) 3D gradient system for two B0 field directions in earth's field MRI. *MAGMA* 26:565-573.

Luo Q., Jiang X., Gao J.H. (2011a) Detection of neuronal current MRI in human without BOLD contamination. *Magn Reson Med* 66:492-497.

Luo Q., Jiang X., Chen B., Zhu Y., Gao J.H. (2011b) Modeling neuronal current MRI signal with human neuron. *Magn Reson Med* 65:1680-1689.

Luo Q., Lu H., Lu H., Senseman D., Worsley K., Yang Y., Gao J.H. (2009) Physiologically evoked neuronal current MRI in a bloodless turtle brain: detectable or not? *NeuroImage* 47:1268-1276.

Maclaren J., Herbst M., Speck O., Zaitsev M. (2013) Prospective motion correction in brain imaging: a review. *Magn Reson Med* 69:621-636.

Maier A., Adams G.K., Aura C., Leopold D.A. (2010) Distinct superficial and deep laminar domains of activity in the visual cortex during rest and stimulation. *Front Syst Neurosci* 4:31.

Martinez D., Montejo N. (2008) A model of stimulus-specific neural assemblies in the insect antennal lobe. *PLoS Comput Biol* 4:e1000139-e1000139.

Menon R.S. (2002) Postacquisition suppression of large-vessel BOLD signals in high-resolution fMRI. *Magn Reson Med* 47:1-9.

Menon R.S., Kim S.G. (1999) Spatial and temporal limits in cognitive neuroimaging with fMRI. *Trends Cogn Sci* 3:207-216.

Menon R.S., Ogawa S., Tank D.W., Ugurbil K. (1993) Tesla gradient recalled echo characteristics of photic stimulation-induced signal changes in the human primary visual cortex. *Magn Reson Med* 30:380-386.

Menon R.S., Ogawa S., Hu X.P., Strupp J.P., Anderson P., Ugurbil K. (1995) Bold Based Functional Mri at 4-Tesla Includes a Capillary Bed Contribution - Echo-Planar Imaging Correlates with Previous Optical Imaging Using Intrinsic Signals. *Magn Reson Med* 33:453-459.

Meyer H.S., Wimmer V.C., Oberlaender M., de Kock C.P., Sakmann B., Helmstaedter M. (2010) Number and laminar distribution of neurons in a thalamocortical projection column of rat vibrissal cortex. *Cereb Cortex* 20:2277-2286.

Mitzdorf U. (1985a) Evoked-Potentials and Current Source Densities in the Cat Visual-Cortex. *Electroencephalogr Clin Neurophysiol* 61:S179-S179.

Mitzdorf U. (1985b) Current source-density method and application in cat cerebral cortex: investigation of evoked potentials and EEG phenomena. *Physiol Rev* 65:37-100.

Mitzdorf U. (1987) Properties of the evoked potential generators: current source-density analysis of visually evoked potentials in the cat cortex. *Int J Neurosci* 33:33-59.

Mountcastle V.B. (1997) The columnar organization of the neocortex. *Brain* 120 (Pt 4):701-722.

Nakamura A., Kakigi R., Hoshiyama M., Koyama S., Kitamura Y., Shimojo M. (1997) Visual evoked cortical magnetic fields to pattern reversal stimulation. *Brain Res Cogn Brain Res* 6:9-22.

Nauhaus I., Busse L., Carandini M., Ringach D.L. (2009) Stimulus contrast modulates functional connectivity in visual cortex. *Nat Neurosci* 12:70-76.

Nicholson C., Freeman J.A. (1975) Theory of current source-density analysis and determination of conductivity tensor for anuran cerebellum. *J Neurophysiol* 38:356-368.

Niedermeyer E., Lopes da Silva F.H. (2005) Electroencephalography : basic principles, clinical applications, and related fields, 5th Edition. Philadelphia: Lippincott Williams & Wilkins.

Noguchi Y., Inui K., Kakigi R. (2004) Temporal dynamics of neural adaptation effect in the human visual ventral stream. *J Neurosci* 24:6283-6290.

Noll D.C., Nishimura D.G., Macovski A. (1991) Homodyne detection in magnetic resonance imaging. *IEEE Trans Med Imaging* 10:154-163.

Nunez P.L., Srinivasan R. (2006) Electric fields of the brain : the neurophysics of EEG, 2nd Edition. Oxford ; New York: Oxford University Press.

Ogawa S., Lee T.M., Nayak A.S., Glynn P. (1990a) Oxygenation-Sensitive Contrast in Magnetic-Resonance Image of Rodent Brain at High Magnetic-Fields. *Magn Reson Med* 14:68-78.

Ogawa S., Lee T.M., Kay A.R., Tank D.W. (1990b) Brain magnetic resonance imaging with contrast dependent on blood oxygenation. *Proc Natl Acad Sci U S A* 87:9868-9872.

Okusky J., Colonnier M. (1982) A Laminar Analysis of the Number of Neurons, Glia, and Synapses in the Visual-Cortex (Area-17) of Adult Macaque Monkeys. *J Comp Neurol* 210:278-290.

Park T.S., Lee S.Y. (2007) Effects of neuronal magnetic fields on MRI: numerical analysis with axon and dendrite models. *NeuroImage* 35:531-538.

Park T.S., Lee S.Y., Park J.H., Lee S.Y. (2004) Effect of nerve cell currents on MRI images in snail ganglia. *Neuroreport* 15:2783-2786.

Parkes L.M., de Lange F.P., Fries P., Toni I., Norris D.G. (2007) Inability to directly detect magnetic field changes associated with neuronal activity. *Magn Reson Med* 57:411-416.

Peters A., Yilmaz E. (1993) Neuronal organization in area 17 of cat visual cortex. *Cereb Cortex* 3:49-68.

Petridou N., Schafer A., Gowland P., Bowtell R. (2009) Phase vs. magnitude information in functional magnetic resonance imaging time series: toward understanding the noise. *Magn Reson Imaging* 27:1046-1057.

Petridou N., Plenz D., Silva A.C., Loew M., Bodurka J., Bandettini P.A. (2006) Direct magnetic resonance detection of neuronal electrical activity. *Proc Natl Acad Sci U S A* 103:16015-16020.

Pettersen K.H., Einevoll G.T. (2008) Amplitude variability and extracellular low-pass filtering of neuronal spikes. *Biophys J* 94:784-802.

Pettersen K.H., Lindén H., Dale A.M., Einevoll G.T. (2010) Extracellular spikes and current-source density. In. Cambridge, UK: Cambridge University Press.

Purves D. (2004) Neuroscience, 3rd Edition. Sunderland, Mass.: Sinauer Associates, Publishers.

Rager G., Singer W. (1998) The response of cat visual cortex to flicker stimuli of variable frequency. *Eur J Neurosci* 10:1856-1877.

Raj D., Paley D.P., Anderson A.W., Kennan R.P., Gore J.C. (2000) A model for susceptibility artefacts from respiration in functional echo-planar magnetic resonance imaging. *Phys Med Biol* 45:3809-3820.

Rappelsberger P., Pockberger H., Petsche H. (1981) Current Source Density Analysis - Methods and Application to Simultaneously Recorded Field Potentials of the Rabbit Visual-Cortex. *Pflugers Archiv-European Journal of Physiology* 389:159-170.

Regan D. (1989) Human Brain Electrophysiology: Evoked Potentials and Evoked Magnetic Fields in Science and Medicine. New York: Elsevier Science.

Rennie C.J., Wright J.J., Robinson P.A. (2000) Mechanisms of cortical electrical activity and emergence of gamma rhythm. *J Theor Biol* 205:17-35.

Robinson P.A., Rennie C.J., Wright J.J. (1997) Propagation and stability of waves of electrical activity in the cerebral cortex. *Phys Rev E Stat Nonlin Soft Matter Phys* 56:826-840.

Saul A.B., Cynader M.S. (1989) Adaptation in single units in visual cortex: the tuning of aftereffects in the temporal domain. *Vis Neurosci* 2:609-620.

Schroeder C.E., Mehta A.D., Givre S.J. (1998) A spatiotemporal profile of visual system activation revealed by current source density analysis in the awake macaque. *Cereb Cortex* 8:575-592.

Scott G.C., Joy M.G., Armstrong R.L., Henkelman R.M. (1991) Measurement of nonuniform current density by magnetic resonance. *IEEE Trans Med Imaging* 10:362-374.

Scott G.C., Joy M.L.G., Armstrong R.L., Henkelman R.M. (1992) Sensitivity of Magnetic-Resonance Current-Density Imaging. *J Magn Reson* 97:235-254.

Sengpiel F., Sen A., Blakemore C. (1997) Characteristics of surround inhibition in cat area 17. *Exp Brain Res* 116:216-228.

Singh M. (1994) Sensitivity of Mr Phase-Shift to Detect Evoked Neuromagnetic Fields inside the Head. *IEEE Trans Nucl Sci* 41:349-351.

Srinivasan R., Russell D.P., Edelman G.M., Tononi G. (1999) Increased synchronization of neuromagnetic responses during conscious perception. *J Neurosci* 19:5435-5448.

Steriade M. (2006) Grouping of brain rhythms in corticothalamic systems. *Neuroscience* 137:1087-1106.

Thomson A.M. (1997) Activity-dependent properties of synaptic transmission at two classes of connections made by rat neocortical pyramidal axons in vitro. *J Physiol-London* 502:131-147.

Thomson A.M., West D.C., Hahn J., Deuchars J. (1996) Single axon IPSPs elicited in pyramidal cells by three classes of interneurones in slices of rat neocortex. *J Physiol* 496 (Pt 1):81-102.

Tononi G., Srinivasan R., Russell D.P., Edelman G.M. (1998) Investigating neural correlates of conscious perception by frequency-tagged neuromagnetic responses. *Proc Natl Acad Sci U S A* 95:3198-3203.

Ulbert I., Karmos G., Heit G., Halgren E. (2001) Early discrimination of coherent versus incoherent motion by multiunit and synaptic activity in human putative MT+. *Hum Brain Mapp* 13:226-238.

Van de Moortele P.F., Pfeuffer J., Glover G.H., Ugurbil K., Hu X.P. (2002) Respiration-induced B-0 fluctuations and their spatial distribution in the human brain at 7 tesla. *Magn Reson Med* 47:888-895.

Wang H., Wang B., Normoyle K.P., Jackson K., Spitler K., Sharrock M.F., Miller C.M., Best C., Llano D., Du R. (2014) Brain temperature and its fundamental properties: a review for clinical neuroscientists. *Front Neurosci* 8:307.

Waxman S.G., Kocsis J.D., Stys P.K. (1995) The axon : structure, function, and pathophysiology. New York: Oxford University Press.

Witzel T., Lin F.H., Rosen B.R., Wald L.L. (2008) Stimulus-induced Rotary Saturation (SIRS): a potential method for the detection of neuronal currents with MRI. *NeuroImage* 42:1357-1365.

Woosley J.K., Roth B.J., Wikswo J.P. (1985) The Magnetic-Field of a Single Axon - a Volume Conductor Model. *Math Biosci* 76:1-36.

Wowk B., McIntyre M.C., Saunders J.K. (1997) k-space detection and correction of physiological artifacts in fMRI. *Magn Reson Med* 38:1029-1034.

Wright J.J. (2009) Generation and control of cortical gamma: findings from simulation at two scales. *Neural Netw* 22:373-384.

Wright J.J., Rennie C.J., Lees G.J., Robinson P.A., Bourke P.D., Chapman C.L., Gordon E., Rowe D.L. (2003) Simulated electrocortical activity at microscopic, mesoscopic, and global scales. *Neuropsychopharmacology* 28 Suppl 1:S80-93.

Wu Z.H. (2009) The Difference of SSVEP Resulted by Different Pulse Duty-cycle. In: *2009 International Conference on Communications, Circuits and Systems Proceedings*, pp 605-607.

Xiong J., Fox P.T., Gao J.H. (2003) Directly mapping magnetic field effects of neuronal activity by magnetic resonance imaging. *Hum Brain Mapp* 20:41-49.

Xue Y., Gao J.H., Xiong J. (2006) Direct MRI detection of neuronal magnetic fields in the brain: theoretical modeling. *NeuroImage* 31:550-559.

Yesilyurt B., Ugurbil K., Uludag K. (2008) Dynamics and nonlinearities of the BOLD response at very short stimulus durations. *Magn Reson Imaging* 26:853-862.

Appendices

A The state equations of the LCM

The LCM uses a simplified version of the continuum cortex model to simulate neuronal processes (Robinson et al., 1997; Rennie et al., 2000; Wright et al., 2003; Wright, 2009). The equations used in the LCM, as listed here, are variations of the equations used in the continuum cortex model (CCM) (Wright, 2009).

A.1 Spike propagation

Neuron generates spikes in the soma and delivers them through the axon tree to the target neurons (Kandel et al., 2000). Using the mean field approximation, I assumed that spike propagation is isotropic, and synapses are distributed evenly in cortex. Then spike a synapse received in a unit time is

$$\phi_{\mathrm{ic}}\left(\mathbf{r},\ \mathbf{r}'\right)=\int f\left(\mathbf{r},\ \mathbf{r}'\right)Q_p\left(\mathbf{r}',\ t-\frac{\left|\mathbf{r}-\mathbf{r}'\right|}{v_p}\right)\mathrm{d}^2\mathbf{r}' \tag{S1.1}$$

The integral is taken over the cortical layer; $Q_p(\mathbf{r}',t)$ is the average spike rate generated at $\mathbf{r}'$; subscript p indicates the type of spikes; v_p is the spike propagation speed; $f(\mathbf{r},\mathbf{r}')$ is the *spike propagator*, which is the possibility for a spike generated at $\mathbf{r}'$ to reach synapses at $\mathbf{r}$. The propagators of single neurons vary, depending on neurons' morphology and physiology. However, using mean field approximation the propagator can be simplified as only a function of distance $\left|\mathbf{r}-\mathbf{r}'\right|$. I use the following propagator in LCM

$$f(r,r')=\exp\left(\frac{-\left|\mathbf{r}-\mathbf{r}'\right|^2}{2\gamma_p^2}\right) \tag{S1.2}$$

where γ_p is the spike propagation range parameter. Unlike in CCM, Eqn. (S1.2) is not normalized. The reason is that the conservation of spikes does not hold in the brain, because the spikes can be vanished or enhanced during their propagation in axons (Waxman et al., 1995).

A.2 Postsynaptic potential

The afferent spikes change the membrane potential of the target neuron. The amplitude of the membrane potential change depends on the afferent spike rate and its membrane potential. LCM uses the same formulation for the membrane potential change as CCM (Wright, 2009)

$$M_{qp}^{[\mathrm{rcpt}]}\left(V_q,\phi_p\right)=g_p\left(\frac{V_p^{\mathrm{rev}}-V_q}{V_p^{\mathrm{rev}}-V_q^{[0]}}\right)\phi_p\exp(-\lambda^{[\mathrm{rcpt}]}\phi_p) \tag{S1.3}$$

where g_p is the synaptic gain at the resting membrane potential; V_p^{rev} is the reversal membrane potential; p indicates the type of afferent spike, and q indicates the type of target neuron. $\lambda^{[\mathrm{rcpt}]}$ is spike adaptation parameter. Three kinds of neurotransmitter receptors are considered in the LCM: *AMPA* receptor, *NMDA* receptor, and *GABA* receptor.

In the LCM, each synapse receives spikes from four sources: LGN (ϕ_{th}), current cortical layer (ϕ_{ic}), other cortical layers (ϕ_{ly}) and other cortical areas (ϕ_{cc}). Spike rate from other cortical area (ϕ_{cc}) is assumed to be the background noise. It is small white noise in the simulation. Spikes from LGN (ϕ_{th}) are the simulation input, which depends on the stimulations. Spike rates from other cortical layers (ϕ_{ly}) is

$$\phi_{\mathrm{ly}_i}(\mathbf{r})=\sum_{\text{other ly}}Q_{\mathrm{ly}_j}(\mathbf{r},t-\delta t)f(\delta r) \tag{S1.4}$$

where the summation is taken over all layers except layer $\mathrm{ly_i}$; $Q_{\mathrm{ly}_j}(\mathbf{r},t-\delta t)$ is the spike rate in cortical layer $\mathrm{ly_j}$; δr is the vertical distance between layer $\mathrm{ly_i}$ and $\mathrm{ly_j}$; $\delta t=\delta r\,/\,v_{\mathrm{v}}$ is the time delay of spikes from layer $\mathrm{ly_j}$ to layer $\mathrm{ly_i}$.

The total membrane potential change is the summation of the membrane potential changes caused by all afferent spikes

$$M_{qp}^{\ [\mathrm{rcpt}]}=N_{\mathrm{ic,\,qp}}M_{\mathrm{ic,\,p}}+N_{\mathrm{cc,\,qp}}M_{\mathrm{cc,\,p}}+N_{\mathrm{th,\,qp}}M_{\mathrm{th,\,p}}+\sum_{\text{other ly}}N_{\mathrm{ly,\,qp}}M_{\mathrm{ly,\,p}} \tag{S1.5}$$

where N_{qp} is the average number of neuron synapses between the two neuron groups.

In CCM, the time course of PSP consists of the convolution of three different functions. However, in LCM it is simplified to a gamma function

$$R^{[\mathrm{rcpt}]}(V_{\mathrm{q}},t)=\begin{cases}0 & t\le\tau^{[\mathrm{rcpt}]}\\ \dfrac{\alpha^{n}}{\Gamma(n)}(t-\tau)^{n-1}\exp\left[-\alpha(t-\tau)\right] & t>\tau^{[\mathrm{rcpt}]}\end{cases} \tag{S1.6}$$

where α and n are parameters; $\tau^{[\mathrm{rcpt}]}$ is the synaptic delay. The values of α and n should depend on the soma membrane potential V_q, since the shape of the PSP time course depends on the target neuron's soma membrane potential (Thomson et al., 1996; Thomson, 1997). LCM uses the following linear approximation

$$\alpha(V_{\mathrm{q}})=\alpha_0+k(V_{\mathrm{q}}-V_{\mathrm{q}}^{[0]}), \tag{S1.7}$$

$$n(V_{\mathrm{q}})=\frac{\alpha}{\alpha_0}(n_0-1)+1 \tag{S1.8}$$

.

Eqn. (S1.7) and (S1.8) ensure that the peaks of the time courses do not change, while their standard deviations depend on membrane potential V_q linearly. To improve the efficiency of the program, LCM only uses simplified step values of α and n for different membrane potential ranges (see Appendix 2 for details).

A.3 Soma membrane potential aggregation

The population average of neuron soma membrane potential change is(Wright, 2009)

$$V_q(\mathbf{r})=V_q^{[0]}+\delta V(\mathbf{r})=V_q^{[0]}+\sum_p\sum_{[\mathrm{rcpt}]}M_{qp}^{[\mathrm{rcpt}]}(V_q,\phi_p)\otimes R^{[\mathrm{rcpt}]}(V_q,t) \tag{S1.9}$$

where $\otimes$ denotes convolution in time.

A.4 Spike generation

Spike generation function of individual neurons is a step function. Their activation thresholds varies. If I assume the thresholds are distributed normally, then the mean firing rate of a neuron population is (Wright, 2009)

$$Q_q(t)=\frac{Q_q^{\max}}{1+\exp\left[-\pi(V_q-\theta_q)\,/\,(\sqrt{3}\sigma_q)\right]} \tag{S1.10}$$

where θ_q and σ_q are the mean and standard deviation of the thresholds.

B The parameters of the LCM

In the LCM, there are approximately 150 parameters, most of which have been determined from experimental data.

B.1 Laminar synapse numbers

The LCM uses a quantitative connection map to define the synaptic connection between cortical layers. The connection map is derived from (Binzegger et al., 2004), in which the authors counted the synapses formed on each neuron type at each cortical layer (see Figure 7 and 8 in Ref. Binzegger et al., 2004) by reconstructing 39 single neurons and thalamic afferents in the cat primary visual cortex. Using the data, I calculated the average synapse numbers formed by excitatory and inhibitory neurons in each cortical layer, and the results are provided in Table S1(Data acquired from Ref. Izhikevich and Edelman, 2008).

		Presynaptic neuron											
		e1	i1	e2/3	i2/3	e4	i4	e5	i5	e6	i6	cc	X/Y
Postsynaptic neuron	e1	907	1600	907	160							7752	408
	i1	73	898	560	151	9		9				7191	
	e2/3		133	3557	799	883	46	431		133	46	1019	54
	i2/3		54	1769	509	443	28	215		69	23	429.2	
	e4		27	416	79	1073	488	82		1684	305	1507	169
	i4			168	39	635	357	35		1024	182	829	54
	e5		138	2526	168	756	71	620	85	360	547	1510	1692
	i5			1356	75	382	33	376	66	128	340	227	3
	e6		2	646	44	554	111	330	24	1100	784	2602	188
	i6			81	6	93	3	161	13	464	496	1887	19

Table S1 Synapse numbers formed between neurons of different types.

Each row represents a postsynaptic neuron type, where e1 (i1) indicates excitatory (inhibitory) neuron in layer 1, and so on. Each column represents a presynaptic neuron type, where CC indicates the presynaptic neuron is outside the primary visual cortex, and X/Y when they are in LGN.

There are a large number of unassigned symmetric and asymmetric synapses in the data of (Binzegger et al., 2004), because some neuron types, such as the spiny neuron in layer 1 and smooth neuron in all layers, are not included in their estimations. Following the suggestion of the authors (Binzegger et al., 2004), I assumed that: 1) The unsigned symmetric synapses are from the smooth neurons of the layer where the synapses are formed (Binzegger et al., 2004); 2) 5% of unsigned asymmetric synapses come from the unspecific nuclei of thalamus (Izhikevich and Edelman, 2008); 3) 95% of unsigned

asymmetric synapses come from other cortical area (Izhikevich and Edelman, 2008). Since no information about excitatory neuron of layer 1 is provided, I further assume that: 4) 10% of unsigned asymmetric synapses on excitatory neurons of layer 1 are from excitatory neurons of the same layer. 5) 0.03% of unsigned asymmetric synapses on inhibitory neurons of layer 1 are from excitatory neurons of the same layer. Modification has been made to data in Table S1.

Table S2 lists the values of cortical depth, ratios of the number of neurons used in LCM. They are estimated from physiological experiment data (Okusky and Colonnier, 1982; Binzegger et al., 2004).

Cortical layer	Cortical depth (mm)	Percentage of neurons in the cortex (%)	Percentage of excitatory neurons in the layer (%)
L1	0.123	1.6	3
L23	0.526	33.8	78
L4	1.133	34.9	80
L5	1.568	7.6	82
L6	1.816	22.1	83

Table S2 Neuron numbers in cortical layers.

B.2 Neuronal physiology parameters

LCM uses the same neuronal physiology parameters as CCM (Wright, 2009), given in Table S3.

Parameter	Meaning	Value
$Q_p^{\max}$	Maximum firing rate of neuron	$Q_e^{\max} = 100$ spikes/sec $Q_i^{\max} = 200$ spikes/sec
V_p^{rev}	Neuron reversal potential	$V_i^{\text{rev}} = -70\ \text{mV}$ $V_e^{\text{rev}} = 0\ \text{mV}$
$V_p^{[0]}$	Neuron resting membrane potential	-64 mV
θ_q	Mean membrane potential when half of neurons are full firing	-35 mV
σ_q	Standard deviation of neuron firing probability	Excitatory: 14.5 mV Inhibitory: 12 mV

Table S3 Neuron electrophysiological property parameters.

B.3 Postsynaptic time course parameters

The postsynaptic potential time course parameters were estimated from (Thomson et al., 1996; Thomson, 1997), and shown in Table S4. Since the reported values of PSP time cover a large range, I chose the middle parameter value if a value range was provided or the average when multiple values had been reported.

Parameter	Meaning	Value
$a^{[\mathrm{rcpt}]}$	PSP change onset time constant	$[\mathrm{AMPA}] = 138.8$ $[\mathrm{NMDA}] = 42.6$ $[\mathrm{GABA}] = 68.5$
$n^{[\mathrm{rcpt}]}$	PSP change onset time constant	$[\mathrm{AMPA}] = 1.70$ $[\mathrm{NMDA}] = 2.1$ $[\mathrm{GABA}] = 1.55$
$\tau^{[\mathrm{rcpt}]}$	Synaptic delay	$[\mathrm{AMPA}] = 0.38\ \mathrm{msec}$ $[\mathrm{NMDA}] = 0.38\ \mathrm{msec}$ $[\mathrm{GABA}] = 0.9\ \mathrm{msec}$
$k^{[\mathrm{rcpt}]}$	Parameter of PSP time course dependence on soma membrane potential	$[\mathrm{AMPA}] = -0.3\ \mathrm{mV}^{-1}$ $[\mathrm{NMDA}] = -0.2\ \mathrm{mV}^{-1}$ $[\mathrm{GABA}] = 0.5\ \mathrm{mV}^{-1}$
$\lambda^{[\mathrm{rcpt}]}$	Receptor spike adaption parameters	$[\mathrm{AMPA}] = 12\ \mathrm{msec}$ $[\mathrm{NMDA}] = 37\ \mathrm{msec}$ $[\mathrm{GABA}] = 50\ \mathrm{msec}$

Table S4 Synaptic transmission parameters.

C Supplementary Tables and Figures

C.1 Supplementary tables

presynaptic neuron	postsynaptic neuron	synapse location	synapse number
P2/3	P5	layer I	85
		layer II/III	388
		layer IV	12
		layer V	2040
P5	P2/3	layer I	1
		layer II/III	429

Table S5 The synaptic connections between P2/3 and P5.

Refer to Figure 9 in (Izhikevich and Edelman, 2008) for a complete cortical connection map.

C.2 Supplementary Figures

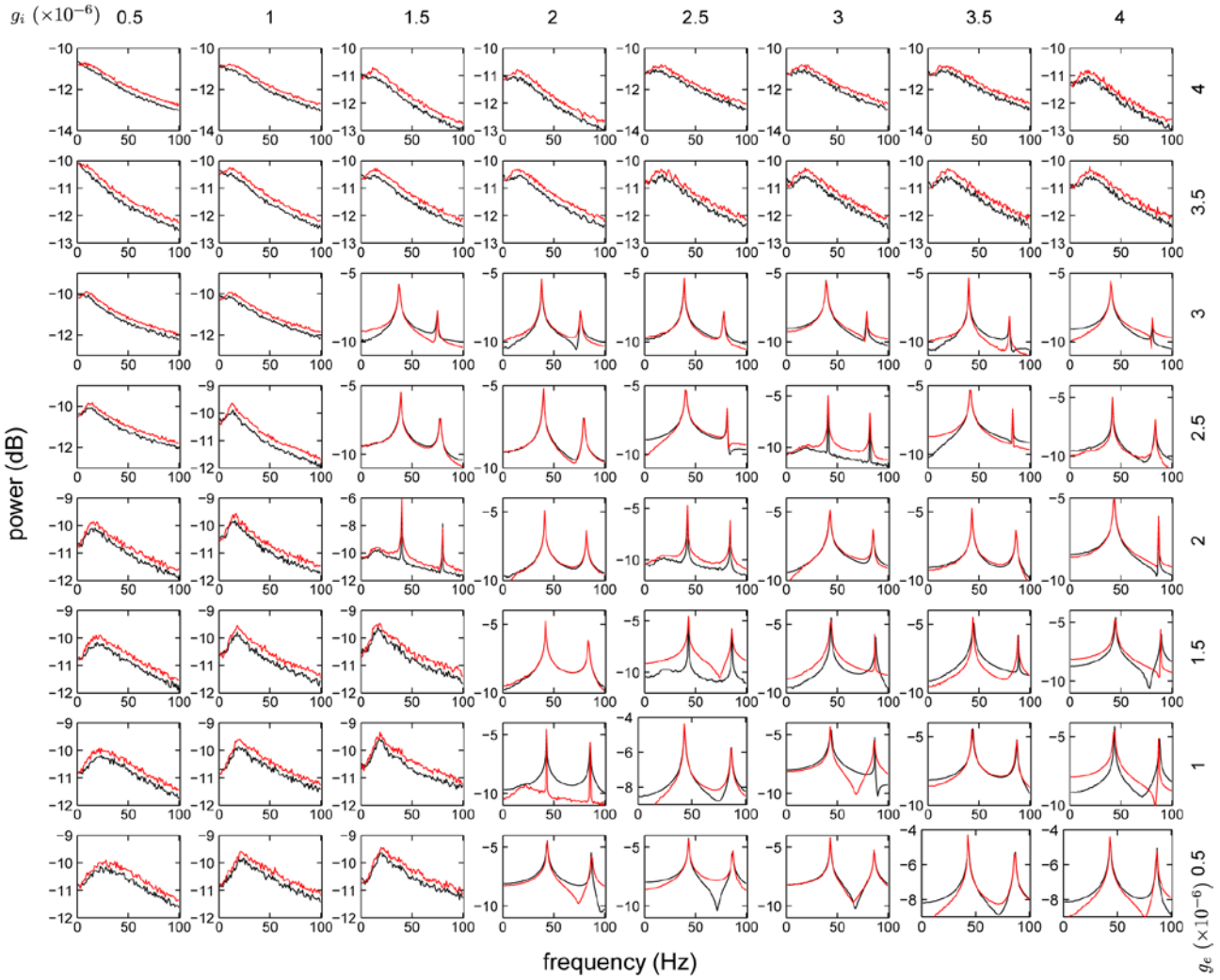

Figure S1. The effects of synaptic gains on LFP frequency.

Provided is the detailed map of frequency spectra of LFPs produced by LCM using different excitatory and inhibitory gains. The red lines show the frequency spectra of stimulated LFPs, while the black lines show that of spontaneous LFPs.

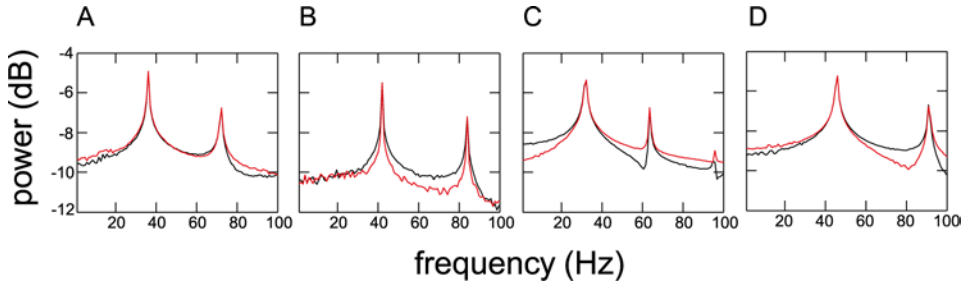

Figure S2. The shift of frequency peaks with different PSP time courses.

Provided are LCM produced LFP frequency spectra while the peak of IPSP time course is shifted (A) from 8 msec to 16 msec and (B) 4 msec, and the peak of AMPA EPSP time course is shifted (C) from 5 msec to 16 msec and (D) 2.5 msec.

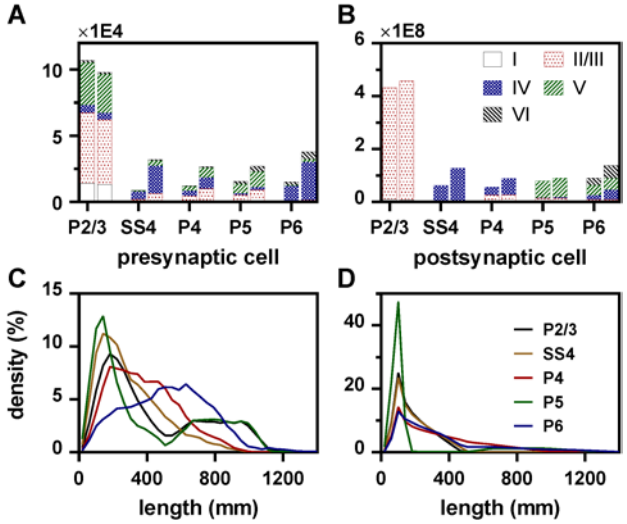

Figure S3 Statistics of the model.

Shown are the numbers of (A) APs and (B) PSPs produced within 100 msec by spontaneous and stimulated activity, and the densities of (C) axon and (D) dendrite lengths. In (A-B), the left and right bars of each group show the results of the spontaneous and stimulated activity, respectively, and the bar patterns denote the target layers of APs in (A) and the location of PSP afferent synapses in (B).

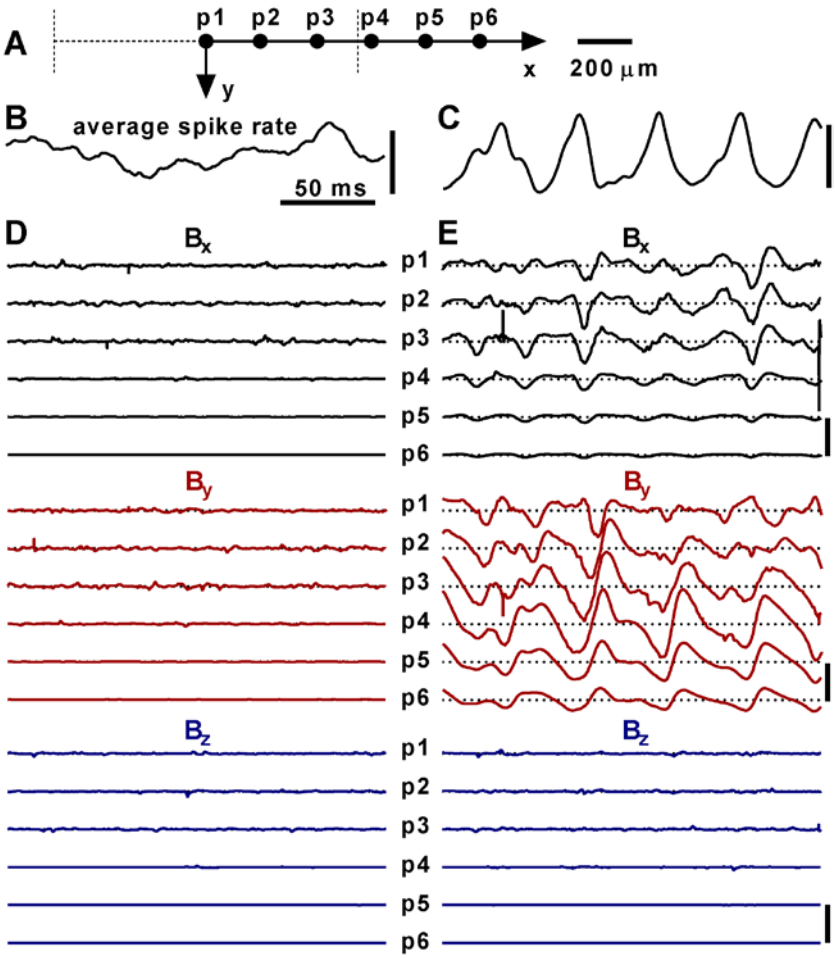

Figure S4 NMFs spatial variations.

Illustrated are (A) the locations of six field points in the middle layer of the cortex for which NMFs are computed (the dashed lines denote the boundaries of the active region), (B) the average neuronal firing rates of the spontaneous activity (scale bar: 0.001 spike/sec) (C) and stimulated activity (scale bars: 20 spike/sec), and the NMFs during (D) spontaneous activity and (E) stimulated activity (scale bar: 500 pT). Some of these results are also shown in Figure 2.

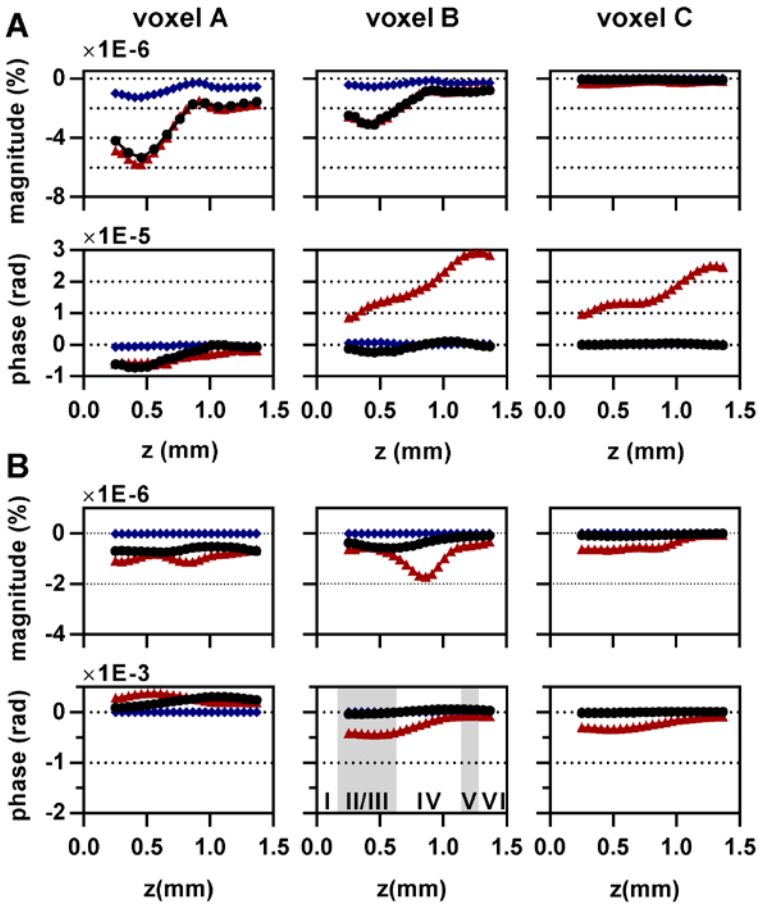

Figure S5 The nc-MRI signal magnitude and phase in different cortical depths.

Shown are the nc-MRI signals in different cortical depths for (A) spontaneous activity and (B) stimulated activity (PAT=200msec). Each point represents a 1.12×1.12×0.5 mm voxel, and the z axis is located at voxel centre. Results were calculated from the same dataset as Figure 5-7. It should be pointed out that results shown here also vary with PAT window size and position.

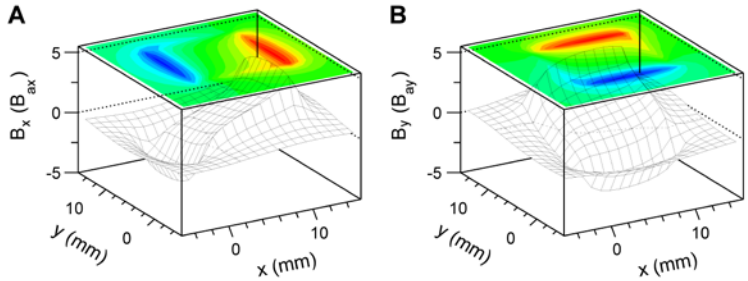

Figure S6 Spatial NMFs of an extended cortical region.

The NMFs were calculated using the method shown in Figure 5-9. In the calculation, the following relationships were adopted, $B_{\mathrm{A}x} = B_{\mathrm{A}y} = B_{\mathrm{B}y}$ and $B_{\mathrm{B}x} = 4B_{\mathrm{B}y}$.

D A MRI compatible strobe light system

A MRI-compatible strobe light system was developed in this project. The strobe light system comprised two components: an electronic control system and optical fibres. The electronic control system employed a crystal oscillator (EPSON SG-8002DC with frequency stability of 50 ppm) to generate a 4 MHz oscillatory signal, which was then divided into desirable frequencies using a dedicated digital circuit. The signal was then used to turn on or off a light-emitting diode (LED) via a solid state relay (Crydom CN048D05 with turning on/off delay of less than 1 msec). The light from the LED was delivered to a mirror in the front of the subject's eyes inside the scanner through a set of 20 coated optical fibres (diameter of the fibres is 1 mm) (see Figure 6-14). The strobe light system was tested separately on each subject with EEG recording before connecting to the MRI system.